Processing of Fluoro Alumino-Silicate Glass-Ceramics by Field Assisted Sintering Technology and Honeycomb Extrusion Technique

By

Praveen Ramakrishnan

A thesis submitted to the University of Birmingham for the degree of

DOCTOR OF PHILOSOPHY

School of Metallurgy and Materials
University of Birmingham
May 2014

தந்தை மகற்காற்றும் நன்றி அவையத்து
முந்தி இருப்பச் செயல்

Sire greatest boon on son confers, who makes him meet,
In councils of the wise to fill the highest seat

Explanation

The benefit which a father should confer on his son is to give him precedence in the assembly of the learned

ஈன்ற பொழுதின் பெரிதுவக்கும் தன்மகனைச்
சான்றோன் எனக்கேட்ட தாய்

When mother hears him named 'fulfill'd of wisdom's lore,'
Far greater joy she feels, than when her son she bore

Explanation

The mother who hears her son called "a wise man" will rejoice more than she did at his birth

மகன் தந்தைக் காற்றும் உதவி இவன்தந்தை
என்நோற்றான் கொல்லெனும் சொல்

To sire, what best requital can by grateful child be done?
To make men say, 'What merit gained the father such a son?'

Explanation

(So to act) that it may be said "by what great penance did his father beget him," is the benefit which a son should render to his father

Tirukkural Poet on the wealth of children (மக்கட்பேறு)

By Tiruvalluvar

Abstract

Field Assisted Sintering Technique (FAST) and extrusion technique was used on fluoro alumino-silicate glasses for crystallisation of relevant glass ceramics. Apatite-mullite glass ceramics derived from the general glass composition of $4.5SiO_2$-$3Al_2O_3$-$1.5P_2O_5$-(5-x)CaO-$xCaF_2$ can be produced by lost wax method. However, Field Assisted Sintering Technique (FAST) and Honeycomb Extrusion Technique (HET) were never used before and this work presents the first data on optimisation of the use of both the above mentioned techniques. Calcium, Strontium and Magnesium containing glass powder compositions were produced and processed by FAST and HET. X-ray diffraction study was carried out on the sample produced using FAST and HET. The Ca substituted glass ceramic samples showed the formation of fluorapatite ($Ca_5(PO_4)_3F$), mullite ($Al_6Si_2O_{13}$) and a minor $AlPO_4$ phase. The Sr substituted glasses crystallised to Sr-fluorapatite ($Sr_5(PO_4)_3F$) and Sr-aluminium silicate ($SrAl_2Si_2O_8$) phases whereas the Mg substituted glass crystallised to mullite ($Al_6Si_2O_{13}$) and wagnerite (Mg_2PO_4F) crystal phases. All the crystal phases formed were in good agreement with previous crystallisation studies of the same glass compositions. The FAST sintered glass ceramic exhibited improved mechanical properties compared to conventional sintering. For the extrusion technique, the rheological properties were studied using the Benbow/Bridgwater model for paste parameters. The honeycomb extrusion pressure drop was also studied using a model developed by Blackburn and Bohm. In this study, waste glass was used to model the glass paste (glass and binder) rheology that was further applied when Ca and Mg-containing glass powders were used. The measured six paste parameters were in good agreement when compared with the experimental results. The produced honeycomb structure was sintered conventionally using a furnace. Microstructural studies and X-ray diffraction were carried out. A well-defined porous structure and formation of crystal phases similar to the phases observed during conventional sintering were observed.

Acknowledgments

First I would like to thank Dr Artemis Stamboulis and Prof. Stuart Blackburn for their time, support, motivation and discussions during my PhD.

I am thankful for UKIERI for providing funding to conduct part of my work in IIT Kanpur, India.

I owe appreciation to Prof. Mike Reece and Dr. Andy Bushby at Queen Mary University of London and his staff and students for using the Field Assisted Sintering facility and Nanoindentation.

Special thanks to Dr. Ben Milsom for his support and assistance in using the Field Assisted Sintering Technique at Queen Mary University of London.

Most of all I would like to thank my parents and my brother for all their support throughout the PhD.

I am thankful to Dr T.M. Sridhar and Dr. Balu Ranganathan for their moral support during my PhD.

Also, thanks to John Wedderburn, Stephen Baker, Frank Briddlestone and James Bowen for their technical and scientific support.

Last but not least, I am thankful to all my friends who supported me all of this period during my PhD.

Table of Contents

LIST OF FIGURES VIII

LIST OF TABLES X

LIST OF ABBREVIATIONS XI

CHAPTER I 1

1.1 Introduction 1

1.1.1 Bioactive ceramics 2

1.1.2 Bioresorbable Ceramics 2

1.1.3 Bio-inert ceramics 3

1.2 Outline of the thesis 3

1.3 Alumino-silicate glass and glass ceramics 4

1.3.1 Calcium containing alumino-silicate glass ceramics 6

1.3.2 Strontium containing alumino-silicate glass ceramics 11

1.3.3 Magnesium containing alumino-silicate glass ceramics 13

1.4 Sintering 14

1.4.1 Crystallisation of glasses by heat treatment 15

1.5 Field Assisted Sintering Technique (FAST) 18

1.5.1 The effect of high-heating rate 18

1.5.2 The effect of applied pressure during sintering 19

1.5.3 Effect of electric current on the FAST process 21

1.5.4 Temperature distribution in SPS 23

1.1.5 Densification mechanism 25

1.5.6 Application of FAST in Biomaterials 25

1.5.7 Application of FAST in Glass-Ceramics 28

1.6 Extrusion of Alumino- silicate glass for tissue engineering scaffold application 29

1.6.1 Natural polymer and synthetic polymers for scaffolds 30

1.6.2 Bioceramics for scaffolds 31

1.6.3 Methods of scaffold fabrication 31

1.7 Honeycomb extrusion process 32

1.7.1 Honeycomb geometry 33

1.7.2 Honeycomb die design 34

1.7.3 Types of Extruder 35

1.8 Paste formulation 36

1.8.1 Rheology of paste flow 36

1.8.2 Analysis of paste flow by Benbow/Bridgwater and co-workers using ram extruder 37

1.8.3 Calculation of Pressure drop in honeycomb die 41

1.9 Aims and objectives 44

1.9.1 FAST sintering process 44

1.9.2 Honeycomb extrusion process 44

CHAPTER II-MATERIALS AND METHODS 45

2.1 Materials 45

2.1.1 Ca containing Alumino Silicate Glass 45

2.1.2 Sr-containing alumino-silicate glasses 45

2.1.3 Mg-containing Alumino-Silicate Glasses 46

2.1.4 Waste Glass 46

2.2 Methods 48

2.2.1 Processing of Materials Using FAST and Honeycombe Extrusion 48

2.2.1.1 FAST Sintering using FCT system 48

2.2.1.2 FAST Sintering using Dr Sinter 49

2.2.1.3 Paste formulation 50

2.2.1.4 Paste characterisation 51

2.2.1.5 Honeycomb Extrusion 52

2.2.2 Characterization techniques 53

2.2.2.1 Density Measurements 53

2.2.2.2 X-ray Powder Diffraction 53

2.2.2.3 Vickers Hardness experiments 53

2.2.2.4 Fracture toughness 54

2.2.2.5 Nano indentation 54

2.2.2.6 Scanning Electron Microscopy 55

CHAPTER III: RESULTS AND DISCUSSION 56

3.1 FAST Sintering of Glass using FCT-System 56

3.1.1 Temperature profile and relative shrinkage on crystallisation of glasses 56

3.1.2 Density 76

3.1.3 X-ray Diffraction 81

3.1.4 Surface Mechanical Properties 94

3.1.5 Microstructure of LG26 glass ceramic 102

3.1.6 Summery 104

3.1.6.1 Glass crystallised at different sintering temperature with 1 min sintering time 104

3.1.6.2 Glass crystallised with sintering time of 5 min at final sintering temperature.. 105

3.1.6.3 Glass crystallised with change in heating rate 105

3.2 Results & Discussion-FAST Sintering of Glass using Dr.Sinter 107

3.2.1 Density measurements 107

3.2.2 XRD analysis 110

3.2.3 Surface Mechanical Properties 113

3.2.4 Microstructural Studies 120

3.2.5 Summery 123

3.3 Results and discussion of honeycomb extrusion process 125

3.3.1 Benbow/Bridgwater model fit in waste glass paste 125

3.3.2 Benbow/Bridgwater Model Fit in LG26 and LG26Mg 131

3.3.3 Honeycomb pressure drop Model Fit 135

3.3.4 X-Ray Diffraction of Honeycomb extrudate of LG26 and LG26Mg 137

3.3.5 Microstructure 138

3.3.6 Summery 141

CHAPTER IV: CONCLUSIONS AND FUTURE WORK 142

4.1 Conclusions 142

4.2 Future work 143

REFERENCE 144

List of Figures

***Figure 1**: Illustration of bioactive behaviour of bioceramics [5, 6] 2*
***Figure 2:** Crystallization of apatite-mullite glass ceramics at different temperatures [55] 9*
***Figure 3:** In vivo testing of apatite-mullite glass ceramics [58]. 10*
***Figure 4**: Basic representation of FAST **[98]**. 20*
***Figure 5:** Types of the electric current applied in resistance sintering [98]. 22*
***Figure 6:** ABAQUS FEM simulations visualizing the temperature distribution on the die and punch surface after 450s operation of spark plasma sintering at a constant Joule heat density of $1.25x10^7$ W/m^3: (a) overall view of the entire system of graphite plate/punch/die system and (b) closer view of the region of top punch and graphite punch/graphite plate interface [108] 24*
***Figure 7**: Morphologies of various HA-based SPS compacts: (a) ceramic HA; (b) ceramic 1 wt % Si-HA; (c) ceramic 3 wt% Si-HA and (d) ceramic 5 wt % Si-HA [98] 27*
***Figure 8:** Er-doped LAS glass ceramic prepared by FAST showing residual porosity [118]. 28*
***Figure 9**: Honeycomb die design [136] 34*
***Figure 10**: Honeycomb die structure design [140] 35*
***Figure 11**: Illustration of ram extrusion analysis of flow[142] 39*
***Figure 12**: Area used in the calculation of holes to slot transition in the equation 17 and equation 18. ..... 41*
***Figure 13**: Honeycomb die design 43*
***Figure 14:** LG26 glass sintering profile in relation with time, temperature and heating rate. 56*
***Figure 15:** Relative punch movement during the heat treatment of LG26. ..... 57*
***Figure 16:** LG26 glass shrinkage in relation to applied force and temperature. 58*
***Figure 17:** LG26Sr glass shrinkage in relation to applied force and temperature. 59*
***Figure 18:** Shrinkage of LG26Mg during the FAST sintering process. 62*
***Figure 19:** LG26 shrinkage and compaction rate of (a) LG26-700-100-1, (b) LG26-800-100-1, (c) LG26-900-100-1 and (d) Lg26-1000-100-1 ..... 63*
***Figure 20**: The rate of shrinkage and the compaction of LG26 glass based on the piston movement (a) LG26-800-100-5 and (b) LG-900-100-5 ..... 65*
***Figure 21:** The shrinkage and compaction of LG26 at the heating rate of 300°C and 500°C/min (a) LG26-800-300-5 and (b) LG26-800-500-5. ..... 67*
***Figure 22:**LG26Sr shrinkage and compaction rate of (a) LG26Sr-700-100-1, (b) LG26Sr-800-100-1, (c) LG26Sr-900-100-1 and (d) LG26Sr-1000-100-1 ..... 68*
***Figure 23:** The shrinkage and compaction of LG26Sr at the heating rate of 300°C and 500°C/min (a) LG26Sr-800-100-5 and (b) LG26Sr-800-100-5 ..... 69*
***Figure 24**: The shrinkage and compaction of LG26Sr at the heating rate of 300°C and 500°C/min (a) LG26Sr-800-300-5 and (b) LG26Sr-800-500-5 ..... 70*
***Figure 25:** LG26Mg shrinkage and compaction rate of (a) LG26Mg-700-100-1, (b) LG26Mg-800-100-1, (c) LG26Mg-900-100-1 and (d) LG26Mg-1000-100-1 ..... 72*
***Figure 26:** Shrinkage rate and piston position of LG26Mg (a) LG26Mg-800-100-5 and (b) LG26Mg-900-100-5 ..... 73*
***Figure 27**: The shrinkage and compaction of LG26Mg at the heating rate of 300°C and 500°C/min (a) LG26Mg-800-300-5 and (b) LG26Mg-800-500-5 ..... 75*
***Figure 28:** (a) Density of FAST sintered LG26, LG26Sr and LG26Mg sintered at different temperature, (b) Density of FAST sintering at different temperature with holding time of 5 min, (c)Density of LG26,LG26Sr and LG26Mg sintered at 800°C using different heating rate temperature 78*
***Figure 29**: XRD patterns of LG26, LG26Sr and LG26Mg glass powder and glass ceramics 83*
***Figure 30:** XRD patterns of LG26, LG26Sr and LG26Mg glass ceramics after FAST sintering at 800°C for 1 min 85*
***Figure 31**: XRD patterns of LG26, LG26Sr and LG26Mg glass ceramics after FAST sintering at 900°C for 1 min 87*
***Figure 32:** XRD diffractogramms of LG26, LG26Sr and LG26Mg glasses and glass ceramics: respectively after FAST sintering at 1000°C for 1 min 88*

Figure 33: *XRD diffractogrammes of LG26, LG26Sr and LG26Mg glasses and glass ceramics: respectively after FAST sintering at 800°C for 5 min* *90*
Figure 34: *XRD diffractogrammes of LG26, LG26Sr and LG26Mg glasses and glass ceramics: respectively after FAST sintering at 900°C for 5 min* *91*
Figure 35: *XRD diffractogrammes of LG26, LG26Sr and LG26Mg glass ceramics after FAST sintering at 800°C for 5 min with 300°C/min as heating rate* *92*
Figure 36: *XRD diffractogrammes of LG26, LG26Sr and LG26Mg glass ceramics after FAST sintering at 800°C for 5 min with 500°C/min as heating rate* *93*
Figure 37: *a) Vickers Hardness of the glass ceramics sintered at different temperature, b) Vickers hardness of the Glass sintered with 5 min holding time at two different temperature,c) Vickers hardness of the glass sintered at different heating rate* *95*
Figure 38*: a) E-modulus of glass sintered at different temperature, b) E-modulus of glass sintered with 5 min holding time,c) E-modulus of the glass sintered at 800°C with different heating rate* *97*
Figure 39*: a)Nanoindentation hardness of the glass ceramics sintered at different temperature, b) Nanoindentation hardness of the glass ceramics sintered 5 min holding time, c) Nanoindentation hardness of the glass sintered at 800°C with different heating rate* *99*
Figure 40*: SEM of Vickers indent on LG26* *102*
Figure 41*: SEM of LG26 glass ceramic sintered at 1000°C* *103*
Figure 42*:a) LG26 Glass ceramics sintered at different processing condition b) Density of LG26Sr substituted Glass-ceramics sintered at different temperature* *108*
Figure 43: *a) X-Ray Diffraction of LG26 Crystallized at Different Temperature, b) X-Ray Diffraction of LG26 and Sr Substitution Glass-Ceramics Crystallized at 700/750 with 5 min Holding, c) X-Ray Diffraction of LG26 and Sr Substitution Glass-Ceramics Crystallized at 700/800 with 5 min Holding* *112*
Figure 44*: a) Hardness of LG26 glass ceramics crystallised at different temperature, b) Hardness of LG26 and Sr substituted glass ceramics* *115*
Figure 45*:SEM of Vickers indent on LG26 glass ceramics* *118*
Figure 46*: E-modulus of LG26 and Sr substituted glass ceramics* *118*
Figure 47*: Fracture toughness of LG26 and Sr substituted glass ceramics* *119*
Figure 48*: SEM of Vickers indentation of 2Kg of applied load of fracture toughness testing by Anstis method* *119*
Figure 49*:a) Fractured surface of LG26, b) Chemical Etching of LG26Sr2, c) Chemical etching of LG26Sr3 d) Chemical etching of LG26Sr100* *122*
Figure 50: *Extrusion load in relation to binder viscosity for Paste 1 with 1 as Compaction, 2 as Transient flow and 3 as steady state of flow.* *126*
Figure 51*: Extrusion load in relation to binder viscosity for Paste 2 with 1 as Compaction, 2 as Transient flow and 3 as steady state of flow.* *127*
Figure 52*: Paste 2 L/D against extrusion Pressure* *128*
Figure 53*: Benbow/Bridgwater model fit with experimental pressure at different velocity of Paste 2* *129*
Figure 54: *Benbow /Bridgwater model fit with experimental pressure at different velocity of Paste 3* *131*
Figure 55: *Benbow /Bridgwater model fit with experimental pressure at different velocity of Paste 4* *132*
Figure 56: *Benbow/Bridgwater model fit with experimental pressure at different velocity of Paste 5* *133*
Figure 57: *Benbow /Bridgwater model fit with experimental pressure at different velocity of Paste 5* *135*
Figure 58: *X-ray diffraction of honeycomb extrudate of LG26 and LG26Mg* *138*
Figure 59: *a) Microstructure of honeycomb cell of LG26Mg sintered, b) Deformation of honeycomb cell in LG26Mg* *138*
Figure 60*: Microstructure of LG26 honeycomb extrudate sintered at 1100°C* *139*

List of Tables

***Table 1**: Various methods of scaffolds fabrication technique [131] 32*
***Table 2:**Molar composition of the base calcium glass**.** 45*
***Table 3:** Molar composition of Sr substituted alumino-silicate glasses.* 46*
***Table 4:** Composition of Mg substituted alumino-silicate glasses* 46*
***Table 5**: Molar composition of Alumino silicate glasses* 47*
***Table 6:** Sintering of calcium base glass using FCT.* 48*
***Table 7:** FAST sintering of LG26.* 49*
***Table 8:** Glass paste formulation* 50*
***Table 9:** Sintering and melting temperature of LG26, Lg26Sr and Lg26Mg* 60*
***Table 10:** FCT Sintering Program of LG26, LG26Sr and LG26Mg.* 61*
***Table 11:** DSC analysis of LG26, LG26Sr and LG26Mg glasses [46].* 61*
***Table 12:** Shrinkage and compaction rate of LG26* 64*
***Table 13:** Shrinkage rate and piston position of LG26 sintering with 5 min holding time* 66*
***Table 14**: The difference in the shrinkage rate and piston position* 66*
***Table 15**: Shrinkage and compaction rate of LG26Sr* 67*
***Table 16:** Difference in the shrinkage rate and piston position during FAST sintering of LG26Sr with 5 mins of holding time and at two different final sintering temperatures* 69*
***Table 17:** Difference in the shrinkage rate and piston position of LG26Sr at different heating rate* 71*
***Table 18**: shrinkage and compaction rate of LG26Mg* 74*
***Table 19:** Difference in the shrinkage rate and piston position of LG26Mg* 74*
***Table 20:** The difference in the shrinkage rate and piston position of LG26Mg* 75*
***Table 21:** Density of LG26,LG26Sr and LG26Mg* 77*
***Table 22:** Density of LG26Mg with 5 min sintering time* 80*
***Table 23:** Density of LG26Mg with different heating rate* 80*
***Table 24**: Crystallographic parameters from XRD database for LG26* 81*
***Table 25**: Crystallographic parameters from XRD database for LG26Sr* 81*
***Table 26**: Crystallographic parameters from XRD database for LG26Mg* 82*
***Table 27**: Mechanical properties of Bioceramics [12]* 101*
***Table 28**: Comparison of mechanical properties between FAST and conventional sintering* 102*
***Table 29**: Density of Lg26 with different sintering Parameters* 109*
***Table 30**: Density of the different molar content of crystallized Sr glass powder* 109*
***Table 31**: Surface Mechanical properties of LG26 and LG26Sr Glass ceramics* 116*
***Table 32**: Vickers Hardness of LG26 glass ceramics* 117*
***Table 33**: Experimental and predicted pressure of Paste 2 at each velocity* 128*
***Table 34**: Benbow/Bridgewater/Bridgewater paste parameters for Paste 2* 128*
***Table 35**: Experimental and predicted pressure of Paste 3 at each velocity* 130*
***Table 36**: Benbow/ Bridgwater paste parameters for Paste 3* 130*
***Table 37:** Benbow/Bridgwater paste parameters for Paste 4* 131*
***Table 38**: Experimental and predicted pressure of Paste 4 at each velocity* 132*
***Table 39:** Benbow/ Bridgwater paste parameters for Paste 5* 133*
***Table 40**: Experimental and predicted pressure of Paste 5 at each velocity* 133*
***Table 41**: Benbow/ Bridgwater paste parameters for Paste 6* 134*
***Table 42:** Experimental and predicted pressure of Paste 6 at each velocity* 134*
***Table 43:** Experimental pressure of honeycomb extrusion* 136*
***Table 44**: Percentage of pressure drop of honeycomb extrusion* 137*

List of Abbreviations

A_h	Open Area of Holes (m^3)
A_s	Open Area of Slots (m^3)
ASTM	American Society for Testing of Materials
A-W	Apatite Wollastonite
D_1	Diameter of the circle touching the outer most hole m
DC	Direct Current
D_O	Diameter of holes (m^3)
EDX	Energy Dispersive X-Ray Analysis
E-Modulus	Elastic Modulus
FAP	Fluorapatite
FAST	Field Assisted Sintering Technique
FT	Fracture Toughness
HA	Hydroxyapatite
H_V	Vicker's Hardness
HET	Honeycomb extrusion technique
L_1	Length of the hole (m)
L_2	Length of the Slot (m)
LAS	Lithium Aluminosilicate
MAS-NMR	Magic Angle Spinning Nuclear Magnetic Resonance
N	Number of the holes (m)
NBO	Non Bridging Oxygen
P	Total Pressure Drop
P_1	Pressure drop for convergent flow in round die entry

P_1	Pressure drop for parallel flow in the round die entry
P_A	Pressure drop into holes
P_B	Pressure drop into holes via intermediate equation
P_C	Pressure drop through holes
P_D	Pressure drop hole-slot transition
PECS	Pulsed Electric Current Sintering
P_F	Pressure drop through slots
Q	Volumetric flow (m/s)
SBF	Simulated Body Fluid
SEM	Scanning Electron Microscopy
SPS	Spark Plasma Sintering
Sr FAP	Sr Fluorapatite
S_W	Slot width (m)
TCP	Tri-Calcium Phosphate
Tg	Glass Transition Temperature
V	Velocity of the extrudate (m^3/s)
V_1	Velocity of paste passing D_1 (m/s)
V_2	Velocity of paste in die holes (m/s)
V_O	Barrel velocity(m/s)
XRD	X-Ray Diffraction
α_1	Velocity factor of bulk paste yield stress (Pa $sm^{-1)}$
β_1	Velocity factor of wall shear stress (Pa $sm^{-1)}$
σ_0	Bulk yield stress
τ_0	Initial wall shear stress

CHAPTER I

1.1 Introduction

Materials that interact with the biological environment for replacement or reconstruction of deceased organs without causing any toxic conditions are called biomaterials. The four major classifications of biomaterials are metals, polymers, composites and ceramics [1, 2]. The history of metallic biomaterials dates back to 18th century where gold, silver, and copper were used exploiting their antimicrobial properties in poor surgical environment [3, 4]. The emerge of modern era metals and metal alloys like 316L stainless steel, Co-Cr alloy and Ti-6Al-4V for orthopaedic applications came later [5, 6].

Compared to metals and metal alloys, polymers are one of the oldest biomaterial used in surgical environment [7]. They have been mainly used as sutures but also as blood vessel prostheses, heart valves, tissue adhesives and lenses [5, 6]. Composites are more recent and advanced materials that are used in medical application [8]. Composites are the result of the mixture of two different materials leading to a material with improved properties [9, 10]. Glass ionomer cements are an example of such a material.

Recently, ceramics play a major role in biomaterials due to their biocompatibility nature based on the composition of materials [11]. These ceramics are also called bioceramics. All biomaterials can be divided into three major groups based on the nature of reactivity with the physiological environment. The three main groups of bioceramics are inert, surface reactive or bioactive, and biodegradable [5, 12]. Inert bioceramics can remain in a physiological environment for longer periods without leaching out any toxic chemicals [13, 14]. Surface reactive ceramics or bioactive ceramics can react with the tissue in a physiological environment forming a chemical bond [5, 13, 14]. Resorbable ceramics degrade along with the restoration of the diseased site without causing any harm to the environment around the tissue [13, 14].

1.1.1 Bioactive ceramics

Hydroxyapatite ($Ca_5(PO_4)_3OH$) is the major mineral content of human bone. Hydroxyapatite ($Ca_5(PO_4)_3OH$) can be synthesised using different processing methods like sol-gel, hyderothermal , biomimetic deposition technique. When hydroxyapatite is implanted in the body a chemical bond is formed between calcium phosphate layer and the protein serum for osteoblast cell attachment. Figure 1 illustrates the complet reaction of this process [15-17].

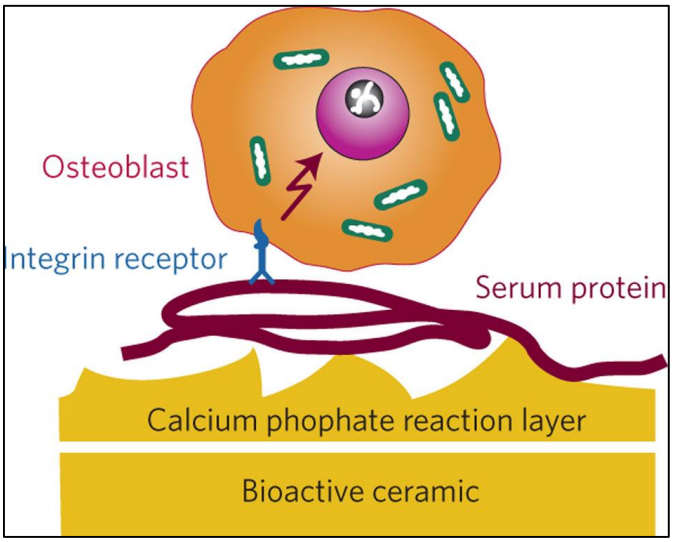

Figure 1: Illustration of bioactive behaviour of bioceramics [5, 6]

Materials like Bioglass®, A-W glass ceramics and calcium phosphates are few examples of developed osteoconductive materials which integrate with bone. Recently researchers showed a vast interest in field of bioceramics for creating new materials with osteoconductive properties for biomedical applications [5, 6]. Bioactive ceramics can be applied as coating materials for implants. This helps towards direct mineralization of bone which creates a strong bonding between bone and implanted materials.

1.1.2 Bioresorbable Ceramics

Bioresorbable ceramics are also known as biodegradable ceramics; the advantages of these ceramics are limitless because they can degrade in the body avoiding the need for a second operation or any passive internal damage occurred during an operation. After implanting

bioresorbable ceramics, they react with the surrounding tissues and help the tissues to grow along as the materials degrade away [5, 16, 18]. This phenomenon is called osteo-induction. These type of ceramics release the chemicals which form the regenerate the tissue at much accelerated level when compared with other bioactive materials, but it is very difficult to achieve due to the rate of resorption along with the stability and strength of the materials [5, 11]. Resorbable ceramics do not produce any toxic substances while degrading; only very few ceramics have been successful as resorbable materials and one of them is tri-calcium phosphate (TCP) that has been in applications for regeneration and restoration of bone defects [5, 19, 20].

1.1.3 Bio-inert ceramics

Bio-inert ceramics do not react with tissues in a biological environment. These types of ceramics stay in the biological environment for longer period. Alumina and zirconia are good examples of inert materials and are used as implants in both dental and orthopaedic applications [20-22]. These inert ceramics have very low surface reactivity and they have superior mechanical properties when compared with other materials. These materials are used as coatings of hip implants due to minimal friction after implantation. If these materials are implanted and undisturbed, the new bone will grow around the implant [23-25].

1.2 Outline of the thesis

This thesis is mainly focuses on the optimisation of the processing conditions for Field Assisted Sintering technique and extrusion technique for the glass composition $4.5SiO_2–3Al_2O_3–1.5P_2O_5–3CaO–2CaF_2$.The field assisted sintering technique is used to understand the changes that has taken place in properties of the glass ceramic and compared with the glass ceramics prepared by the conventional method. The influence of the compositional change, when calcium (Ca) is substituted by strontium (Sr) and magnesium (Mg) is also studied. Strontium substituted samples were sintered at the optimized sintering parameters of the base Ca glass on FAST. The conventional sintering of Ca, Sr, and Mg substituted glasses were carried out by

holding at the nucleation temperature for an hour and then raising to its final crystallisation temperature for another hour. A detailed discussion on the crystallisation behaviour and changes in the properties of the Ca glass-ceramics and the strontium and magnesium substituted glass ceramics is presented here along micro-structural characterisation analysis. The glass used in this technique were melt quenched and grinded glass powder.

The second part of this work mainly deals with extrusion of the glass powder. In the processing technique waste glass was used to optimise the extrusion rheology. Optimised conditions were applied to get initial extrusion parameters for Ca, Sr, and Mg containing alumino-silicate glasses. Furthermore, optimisations were carried out for each glass system to attain the best extrusion rheology of the glass paste. During this optimisation process the rheology model developed by Benbow was followed [26]. After the characterisation of the paste parameters, honeycomb extrusion was carried out to produce a 2D porous scaffold for tissue engineering applications. All the honeycomb extrudates were sintered in a conventional furnace. The sintered samples were characterised using techniques such as X-Ray Diffraction (XRD), Scanning Electron Microscopy (SEM) to understand crystallisation mechanisms and evaluate porosity generated during the crystallisation process.

1.3 Alumino-silicate glass and glass ceramics

Glass is defined as an amorphous solid that has no long-range order of atomic arrangements; the glass is frozen in a structure since it is formed by fast cooling from the melt. There are no changes in specific volume and the glass becomes more rigid with increasing viscosity [25, 27-29]. There are many models to interpret the glass structure. Out of all these models, the most accepted is the Zachariasen's random network theory. Initially, Zachariasen proposed four rules which were then developed for the formation of 3D glass networks [27];

(i) Each oxygen atom is linked to no more than two cations.

(ii) The oxygen coordination number of network cations is small.

(iii) The oxygen polyhedral share only corners with each other and not faces or edges.

(iv) At least 3 corners of oxygen polyhedral should be shared to form a 3D structure.

(v) The percentage of network formers in the glass must be high and surrounded by oxygen tetrahedral.

(vi) Some oxygen should be linked to two network cations and should not form any further bonds with any other cation [27].

The behaviour of glasses can be changed by the introduction of aluminium oxide- an intermediate oxide that can act as both network former and network modifier [30]. Lowenstein suggested that aluminium in four fold coordination can act as an intermediate oxide [26, 29]. This can break the electron balance with a surplus negative charge in the aluminium tetrahedron. These can be compensated by adding positively charged ions like Ca^{2+}, Na^{+}, Mg^{+}, or Al^{3+} (network modifiers). The ratio limit for Al/Si must be smaller or equal to 1 [27, 29]. Above this value, aluminium will not be able to adopt the tetrahedral structure of [SiO_4] units. Lowenstein [31] suggested that, whenever the oxygen bridge is linked by two tetrahedral, the centre of only one can be occupied by aluminium, the other centre must be occupied by a small ion or ion with 4 or more electrovalence [32]. All the oxygens in the glass are bridging oxygens, the non-bridging oxygens can be only formed by the introduction of network modifiers such as CaO or NaO in the glass composition [33]. Similarly, whenever two Al tetrahedral are neighbours, one of the two aluminium ions will take the higher coordination number of 5 or 6 [30, 34].

In the past few decades, there has been a wide interest of research into glass and glass-ceramics due to their properties and potential to be used as biomaterials for biomedical applications [35, 36]. There are three major groups of glasses that have been studied for medical applications; alumino-silicate, alumino-borate and zinc silicate glasses [35, 37, 38]. Although alumino-silicate glasses are known for long time chemical structure are not fully understood. In addition,

alumino-silicate glasses have advantageous properties compared to other glass compositions in terms of chemical durability, tolerance in higher temperature and superior mechanical strength when heat treated to glass ceramics [32, 39]. The composition of glasses plays a major role in determining their properties when crystallised [38]. In order to design new glass-ceramics for medical applications, one should consider the physical, chemical and biological properties required for particular medical applications [37].

The design of glass ceramics for medical application requires the choice of the appropriate amount of raw materials for glass production. The glass composition should be able to crystallise in short time period [40]. The raw materials should highly contain network modifying oxides which cause the formation of non-bridging oxygens in the glass network. Nucleating agents are also useful to enhance crystallization of glasses [41]. Once the desired glass composition is produced, the glass should be characterized by thermal analysis to understand its thermal dynamics such as nucleation and crystallization properties of the glass, which helps in the production of glass ceramics [42].

1.3.1 Calcium containing alumino-silicate glass ceramics

A glass system was developed by Clifford, A. and R. Hill [43] based on the composition of $4.5SiO_2–3Al_2O_3–1.5P_2O_5–3CaO–2CaF_2$. These compositions crystallise to a fluorapatite ($Ca_5(PO_4)_3F$) and mullite ($Al_6Si_2O_{13}$) phase at 1100^{o}C. The apatite phase formed during the crystallisation process is similar to the hydroxyapatite minerals found in human bone [44, 45]. The fluorapatite present in this glass ceramic has better stability, when compared with hydroxyapatite due to fluorine ions being well packed in the apatite crystals in comparison with the hydroxyl ions in the apatite crystal as fluorine ions are smaller [44]. The main advantage of this glass is their ability to cast in any shape using lost wax technique at the temperature of 1400^{o}C this helps to create custom made implants for medical applications. A systematic multinuclear MAS-NMR study was conducted in order to understand the structure of the above

glass compositions [46]. The presence of non-bridging oxygens was reported as well as the presence of a pyrophosphate environment that shifted to an orthophosphate environment in the crystallized glasses with the presence of $AlPO_4$ as a minor phase [47]. On the other hand, fluorine was present as F-Ca(n) and Al-F-Ca(n) species in the glass. In the crystalline glasses, the F-Ca(n) species gave rise to the formation of fluorapatite. Needle-like fluorapatite crystallised first and mechanically interlocked with mullite crystals resulting in a high fracture toughness glass ceramic [43]. The presence of fluorine in this glass system was more essential to form fluorapatite crystal segments. The presence of CaF_2 in this glass system helps with the formation of fluorapatite and the rearrangement of the glass network [48-50]. The fluorine free glass composition crystallised to a β-$Ca_3(PO_4)_2$ (β-calcium phosphate) and $CaAl_2Si_2O_8$ (anorthite) [49, 51]. O'Donnell et al studied the mechanism involved in the crystallisation of the above apatite-mullite glass compositions [52]. It was reported that spinodal decomposition occurred before amorphous phase separation followed by nucleation and crystal growth [52]. During spinodal decomposition calcium, fluorine and phosphorous rich droplets are formed in a silicon and aluminium rich matrix. These two phases have different glass transition temperatures. When the temperature is above the glass transition of the first phase, nanocrystals of fluorapatite are formed. The crystals grow as big as the size of the droplets allows. When the temperature becomes above the glass transition of the second phase, mullite starts to form and the fluorapatite nanocrystals in the droplets grow at the same time to form an interlocking crystallised network of fluorapatite and mullite. At 1200^oC, crystal dissolution was observed followed by recrystallization on cooling [43, 53]. It was reported that the Vickers hardness of the crystallised glasses was in the range of 600 to 800 HV and the fracture toughness ranged from 1.5 to 2.5 MPa√m [48, 54]. The E-modulus of this glass was calculated to be 83 GPa based on an impulse excitation technique as reported by Wang [46].

A recent study on the effect of controlled crystallization of the apatite mullite glass ceramics was carried out by O'Flynn et al [55]. Previous researches showed that the presence of fluorine is significant for the formation of the needle like microstructure of the glass ceramics. It was also shown, that the use of different heating rates had a direct effect on the microstructure with lower heating rate resulting in the formation of finer crystals compared with higher heating rates. In addition, the crystallisation holding time had a direct effect on the formation of fluorapatite crystals with longer holding times resulting in crystal sizes of 10 μm when compared to shorter holding times where the crystal size was measured at 100 nm. Figure 2 shows an SEM study of the crystallisation of apatite-mullite glass ceramics at different temperatures reported by O'Flynn et al [55].

Solid state MAS-NMR studies were performed recently in order to understand the structure of the apatite-mullite glass ceramics. ^{29}Si MAS-NMR spectra of the crystallised glasses suggested the presence of Q^4 (4Al) species associated with the mullite phase.

^{27}Al spectra also confirmed the presence of six fold coordinated aluminium associated from the mullite phase. ^{31}P MAS-NMR indicated that phosphorus was present in the form of orthophosphate (PO_4^3, Q^0) species associated with the formation of a fluorapatite phase. ^{19}F MAS-NMR studies on the other hand, suggested that the presence of F-Ca(n) species were directed involved in the formation of $Ca_5(PO_4)_3F$ (fluorapatite) [56]. The study of crystallisation in these glass ceramics lead to the conclusion that the presence of fluorine and the CaO/P_2O_5 ratio play a major role in the crystallisation of the apatite phase. The presence of fluorine in the above glass system resulted in decreasing the glass transition temperature and crystallization temperature and disturbed the glass network leading to the formation of aluminium in higher coordination states during the crystallization process.

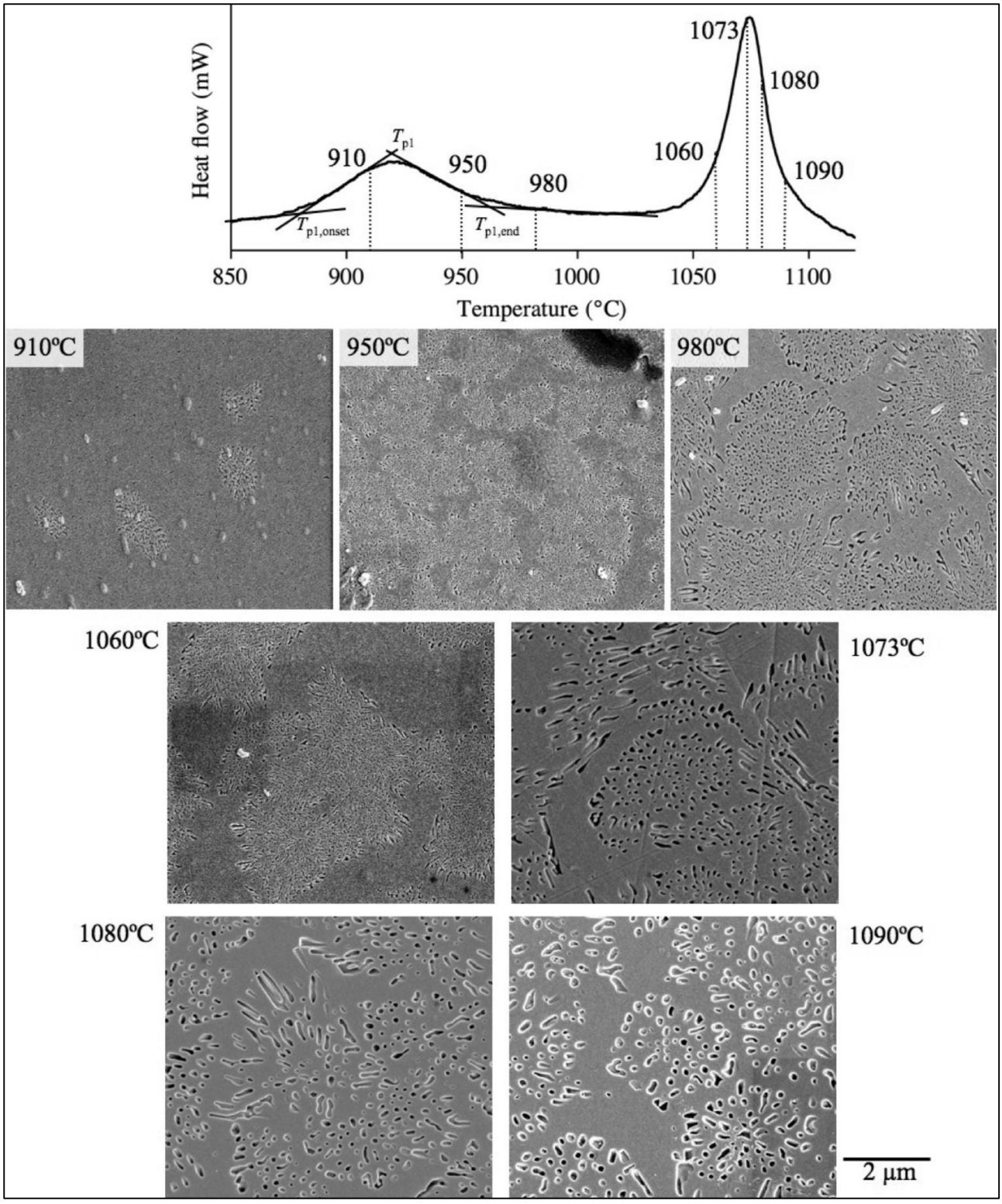

Figure 2: Crystallization of apatite-mullite glass ceramics at different temperatures [55]

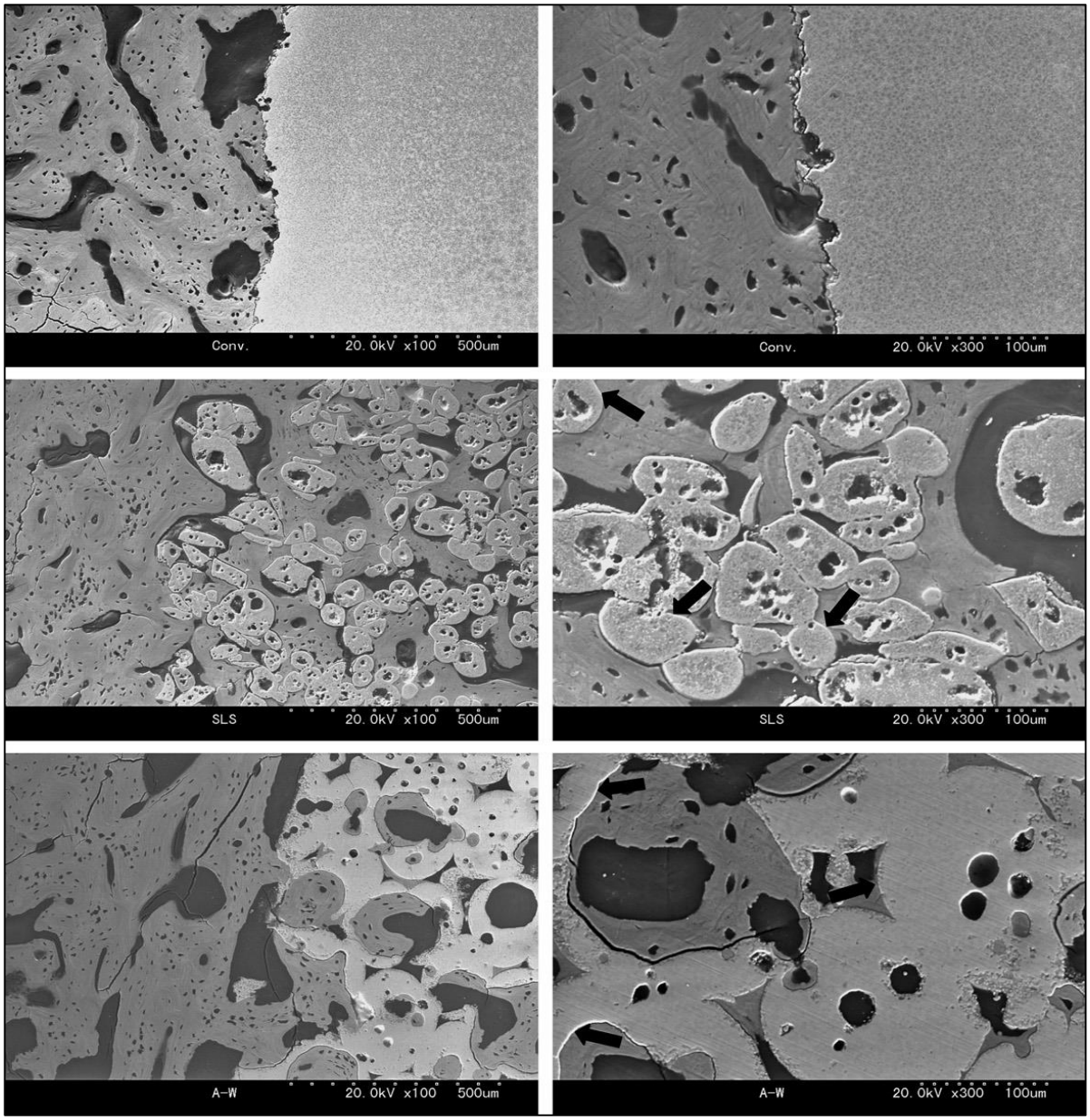

Figure 3: In vivo testing of apatite-mullite glass ceramics [58].

Freeman et al [57] studied the osteo-conductivity of the apatite-mullite glass ceramics using different calcium/phosphate ratio on a rat model. They concluded that the presence of fluorapatite in large proportion favours bone bonding. Recently, Goodridge et al [58] studied the biological properties of these glass ceramics processed using selective laser sintering and compared with cast glass ceramics. Figure 3 shows the SEM of the in vivo testing of apatite-mullite glass ceramics compared with the apatite-wollastonite glass ceramics. Their

cytotoxicity study shows no changes on the material behaviour in both in vitro and in vivo which shows that these materials are biocompatible.

1.3.2 Strontium containing alumino-silicate glass ceramics

In the recent years substituted apatites have become an interesting topic for researchers due to their better properties when compared with natural apatite. Strontium has an atomic radius of 1.16 pm close to calcium atomic radius 0.94 pm, and can substitute calcium in the glass network [59]. The presence of strontium is 3.5% in bone and it is also found in liver, muscles and physiological fluids [60, 61]. Strontium is used in drugs for the treatment of osteoporosis in the forms of strontium ranelate and strontium chloride [61]. The intakes of this drug show a greater deposition of calcium and enhancement of the synthesis of bone collagen. The SrO/CaO substitution has become more interesting for the researchers due to their excellent biocompatibility [62]. The use of substituted Sr bioglass offered a new strategy for bone regeneration. Previous studies on the substitution of strontium for calcium in the apatite lattice to form strontium-calcium hydroxyapatite and pure strontium hydroxyapatite have been reported [63]. Substitution of strontium for calcium results in increased atomic weight and number as well as in increased density of the glass and crystal structure and consequently in increased X-ray radio-opacity [59]. The study conducted by Li et al [64] on the substitution of strontium in the calcium phosphate glass ceramics showed that the strontium containing ceramic dissolved much quicker than Mg or Zn substituted glass ceramics. The glass ceramics were synthesised by a sol-gel method to produce a 3D ceramic scaffold [64]. Fredholm et al studied the effect of substitution of Sr in the structure of bioactive glass [65]. The substitution of Ca for Sr in bioglass resulted in an expansion of the glass network due to strontium being a larger cation. This resulted in a more disrupted glass network with reduced glass transition temperature [65, 66].

The strontium cation can be substituted for calcium in alumino-silicate glasses with composition of $4.5SiO_2–3Al_2O_3–1.5P_2O_5–(3\text{-}x)CaO–(2\text{-}x)CaF_2$. The substitution of strontium for calcium was reported to have a little effect on the glass structure with strontium replacing F–Ca(n) by F–Sr(n) and Al–F–Ca(n) by Al–F–Sr(n) [59]. This substitution had minimal effects on the ^{27}Al, ^{31}P and ^{29}Si MAS-NMR spectra. It has been reported, that strontium substitution for calcium decreased the optimum nucleation temperature of the glasses and had an effect on the crystallization temperature with decreased values observed for mixed Sr and Ca glass ceramics [46]. Strontium substitution promotes surface nucleation of the apatite phase [59]. Low substitution of strontium results in a formation of a calcium fluorapatite phase. Increasing strontium substitution results in a mixed calcium/strontium fluorapatite phase being formed, whereas complete substitution of strontium results in the formation of a pure strontium fluorapatite phase at the first crystallization temperature Tp_1 as well as a monoclinic Sr celcian phase as a second phase at the second crystallisation temperature Tp_2. The FTIR spectra of Sr containing glass ceramics show the P-O asymmetric and symmetric stretching vibration of phosphate group. Increased strontium substitution results in the formation of new phases. This is due to Sr fluorapatite. Hill et al [59] reported that substitution of strontium for calcium hinders the apatite phase formation and inhibits bulk nucleation due to the lower lattice energy of strontium fluorapatite which possibly suppresses the amorphous phase separation, that was known to occur in the strontium free glass (calcium base glass). The E-modulus of the strontium substituted glass was calculated and reported by Wang to be 77 GPa which is lower than the calcium substituted glass, E-modulus of the calcium glass is 83 GPa [46].

The recent research on the biological properties of strontium containing apatite cements (Sr-HA) showed better osteointegration. Sr-HA cements lead to formation of crystalline apatite between bone and the implanted material [67]. The study was conducted on the strontium substituted hydroxyapatite mixed with polyetheretherketone by compression moulding to form

a hybrid composite. It was shown that Sr-HA/polyetheretherketone formed a better and thicker apatite layer when, compared to HA/polyetheretherketone surface when immersed in simulated body fluid (SBF) solution [68]. Only few in vivo studies have been conducted on strontium based apatites. Recently Sabareeswaran et al [69] studied the in vivo properties of strontium containing fluoro-alumino-silicate glass ceramic. The results of their rabbit model study showed osteoconductivity, which was similar to hydroxyapatite based bioglass used as the control material [69].

1.3.3 Magnesium containing alumino-silicate glass ceramics

Magnesium is one of the element which can associated with apatite. Mg substituted hydroxyapatite and polyacerilic acid shows reduction in crystallinity of the apatite lattice with crystal size of 20 to 60 nm, which is close to bone crystals [70]. Magnesium stabilizes β-tricalcium phosphate when produced using the chemical hydrothermal flow synthesis [71]. Magnesium which is involved in various chemical reactions in the human body is found in the kidneys in the form of ($MgHPO_4.3H_2O$) and ($MgNH_4PO_4 \cdot 6H_2O$) salts. This salts shows excellent tissue regeneration and also an alternative for calcium phosphate [72]. The study on the dip-coating of magnesium containing apatite shows that Mg decreases the release of Ca when the material is immersed in simulated body fluid [73]. Recently Hill et al [74] reported the effect of Mg cation substitution in the structure of Bioglass®. It was reported that phosphorous was present in an orthophosphate environment and there was no evidence of Si-O-P bonding in the glass structure. It was also reported, that in the bioactive glass network, MgO played the role of an intermediate oxide. Gu et al [75] reported a study based mixing the Mg and HA powders using ball milling and hot pressed sintering showed higher yield strength with reduced tensile strength.

Magnesium has an atomic weight of 24.3 u and ionic radius of 0.086 pm and has substituted calcium in alumino-silicate glass with the composition $4.5SiO_2–3Al_2O_3–1.5P_2O_5–(3\text{-}x)CaO–$

(2-x)CaF_2 [76]. Magnesium in the above glass behaved like a network modifier in the silicate structure. The previous work on the effect of Mg substitution on the structure of glasses and glass ceramics was reported by Kartellia [76] using various analytical techniques. The results of that study showed that the substitution of magnesium in the alumino silicate glass or calcium resulted in a decrease in the density of the glass due to magnesium being a smaller cation compared to calcium. The density of the magnesium substituted glass ceramics was also decreased. The crystallisation of magnesium substituted glasses resulted in the formation of wagnerite and mullite as the secondary phase. MAS-NMR study in this glass ceramic system was carried out by Wang [46]. The reported results of ^{29}Si NMR spectra showed the formation of Q^4 species of (4Al, 2Al and 3Al) and also ^{27}Al spectra showed the presence of Al(VI) which is associated with the mullite formation. ^{31}P spectra showed the presence of an orthophosphate environment. ^{19}F MAS-NMR of the crystallized glass showed the presence of F-Mg(3) which is associate with the formation of Wagnerite [46]. The reported E-modulus of the glass using IET technique was 90 GPa which was higher compared to other substitution of calcium and strontium glass. This glass did not exhibit an optimum nucleation temperature and phase separation was observed during the crystallization process [76]. However, there are only a few reported studies found on magnesium substituted fluoro alumino-silicate glass ceramics.

1.4 Sintering

Sintering is the oldest and well known methods of consolidating a powder compacts which was originated in the prehistoric era [77]. Currently sintering are used for the fabrication of bulk ceramics and powder metallurgical parts. There are various types of sintering techniques available to improve the density and retain the nanostructure of powder compacts and ceramics. Out of all, this technique recently researchers are more interested in the densification of ceramics by electric current using joule heating with the combination of pressure sintering. This concept of sintering under electric current was developed in 1950s by scientists in

Lockheed missile and Space Company in California [78]. Further developments were made in Japan [79]. There are various types of sintering methods using electric current currently available in the market. Spark plasma sintering (SPS) technique is one such method which combine the principle of pressure assisted sintering by electric current for the densification of materials. This spark plasma sintering is also known as pulse electric current sintering (PECS) or field assisted sintering technique (FAST). In this research work the term FAST will be used instead of SPS this is due to the doubts present on the existence plasma is this process [79]. In the last few years there has been a considerable amount of published research using FAST. This is due to the potential advantages that this technique offers for densification of powder materials.

1.4.1 Crystallisation of glasses by heat treatment

Glass-ceramics are polycrystalline material produced through controlled heat treatment of base glass [80-82]. The properties of glass ceramics are controlled by the mineral phases produced during the process of crystallization [83]. One of the main advantages of glass ceramics is that they can form minerals and crystal structures depending on the initial glass composition [18, 83]. The preparation of glass ceramics involves three major steps:

1. Selection of right amount of raw materials.
2. Melting of the raw materials with rapid cooling.
3. Heat treatment of glass above the glass transition at nucleation temperature and future heat treatment above the crystallization temperature to form a glass ceramic.

When compared to conventional sintered ceramics, glass-ceramics have unique benefits. Complex shapes can be produced by a casting method [38]. The conversion of glass to glass-ceramics usually involves two step thermal treatments of nucleation and crystal growth [84]. The theory of nucleation was first proposed by Gibbs [81, 85, 86]. According to Gibbs, the

formation of new phases requires a small cluster of building units in a volume of super saturated ambient phases [82]. Nuclei were considered as small liquid droplets which are having the same properties as bulk phases with the only exception of being their small linear sizes [38]. The growth of crystals takes place from these small nuclei, when glass is heat treated to higher temperature [85, 87].

To understand the properties of glass crystallization and glass transformation temperature of a glass a thermal characterisation is needed. This thermal analysis can be carried out using differential scanning calorimeter (DSC) or differential thermal analyser. (DTA), which will help to understand the crystallization kinetics and glass transformation temperature [88]. DTA is the older method developed in 1899 whereas DSC is more advanced method developed based on DTA to determine the thermal properties of the materials[88]. Very small amount of sample is more than enough in order to carry out this thermal analysis experiment. Using DSC or DTA with constant heating rate one can find out the changes taken place during the heat treatment. The use of thermal characterisation on glass will also provide a details analysis on the type of crystallisation and activation energy required for the crystallisation of the glass.

Marotta et.al [89] proposed a method to find an nucleation temperature of glass. Which can be applied to any type of glass system that undergoes bulk crystallisation. They suggested that stable nuclei N_n produced in a sample per time element t_n is:

$$N_n = I\ t_n^b \qquad \text{Equation 1}$$

I is the kinetic rate constant of nucleation and b is a parameter related to the nucleation mechanism. If the samples are subjected to lengthening heating in the surrounding area of the assumed nucleation maxima, the exothermal crystallization peak temperatures will reflect variations in nucleation rates. Therefore Marotta showed, that the subsequent equation focused

on shifts in exothermal peak temperatures applies if t_n is the same for each sample at each temperature T_n [90]:

$$\ln I = \frac{E_c}{R}\left[\frac{1}{T_{p'}'} - \frac{1}{T_p}\right] + constant\ t \qquad \text{Equation 2}$$

Where E_c is the activation energy for crystallization, R is the gas constant, T_p' is the crystallization peak temperature occurring after a nucleation hold and T_p is the latter crystallization peak temperature without a nucleation hold. Therefore the whole method works by heating a glass sample to beyond its glass transition temperature and holding the samples at that temperature for one hour, then constantly heating the sample beyond the crystallization peak temperature. The same process is applied to more samples except rising the holding temperature by some increment every time. Finally, a nucleation rate-temperature curve can be obtained by plotting T'_p against T_n. The minimum value of this curve corresponds to the optimum nucleation temperature.

Marotta *et al* [89] also proposed a method to find the activation energies for crystallization which is given in equation 3

$$Ln\,1/r = E_C / RT_P + cons\tan t \qquad \text{Equation 3}$$

According to equation 3 where *r* is the heating rate, E_C is the activation energy of the process, T_P is the temperature corresponding to the maximum of the crystallization peak and R is the universal gas constant. For calculating the activation different heating rates were applied. This methods works by assuming that there is no change in the glass composition during the crystallisation process. However this assumption does not apply to the crystalline phases formed during crystallisation.

1.5 Field Assisted Sintering Technique (FAST)

FAST works under the combined principles of hot press and resistive heating techniques. In the hot press sintering the sample is placed in the cylindrical die and is s surrounded by the cylindrical furnace. In this technique, the pulse electric current is passed through the conductive graphite die which contains the material along with constant application of pressure to consolidate the material [91]. By using resistive heating we can easily attain the minimum heating rate of 100^{o}C/min to maximum heating depends on the configuration of equipment roughly 1000^{o}C/min. During the hot press sintering the heating rate ranges from 1-10^{o}C/min. The advantages of FAST are high heating and cooling rate which helps in lowering the sintering temperature and holding time. Materials prepared by this technique showed greater increase in density when compared with other conventional methods of sintering [91]. Using this method we can control the grain growth and retain with minimum porosity.

1.5.1 The effect of high-heating rate

One of the main advantages of the FAST sintering technique is the heating rate. In the processing of ceramics, the heating rate plays a major role in the densification of materials. The high heating rate helps to improve sintering with minimum grain growth. The main concept of the heating rate in ceramic processing is to avoid surface diffusion, grain coarsening and improve the densification on the lower activation energy materials [92]. In FAST sintering technique electrical current is used that helps to generate a fast heating rate of 100^{o}C-1000^{o}C/min. In order to understand the effect of high-heating rate on the materials processing some researchers have conducted a series of experiments to understand the need of high heating rate on few materials even though some of their results are contradicting Zhou et al [93] conducted the experiment on alumina powder using different particle sizes in FAST method. Fast heating rate resulted always in smaller grain size. On the other hand, the density of the samples changed which is related to the final temperature of the sintered alumina. Kim et al

[94] used the FAST technique to obtain transparency of the alumina material using heating rates ranging from 2^{o}C/min to 100^{o}C/min. It was reported, that using the low heating rate with the final temperature of 1150^{o}C with 20 min sintering time alumina with fine grain size, low porosity and high transparency was produced. The grain size of 0.29µm was observed with 0.0025 nm of porosity. Stanciu et al [92] studied the effect of heating rate on the densification process using conductive and non-conductive powder. They used α-Al_2O_3 as non-conductive and $MoSi_2$ as conductive powder. Their results showed that there is no change in the final density of the sintered samples at the same holding time of both materials. The grain size in the case of alumina was smaller when compared to $MoSi_2$. On the other hand Shen et al [95] showed that the higher heating rate had little effect on the alumina which showed the negative effect on the final density but the grain size was showing the dependence which was also reported by Stanciu et al [92].

When comparing the results of previous works most of results are concluding that higher or faster heating rates can help to control the grain growth with even distribution of grain boundaries resulting in improved density with minimal porosity.

1.5.2 The effect of applied pressure during sintering

FAST technique works under the similar principle like hot press sintering where the application of mechanical pressure is necessary during the densification process of ceramics. The compressive pressure of 150MPa and higher can be applied which depends on the strength of the graphite die [96].

The application of mechanical pressure plays a vital role on particle re-arrangements and the breaking down of agglomerates. The pressure in FAST technique helps in decreasing the sintering temperature by deformation and diffusion of the particles at the sintering temperature. Anselmi-Tamburini et al [97] carried out the sintering of 8 mol of yttria stabilized zirconia in

FAST method. They concluded that the applied pressure had a significant effect on the final density but had no effect on the crystal size.

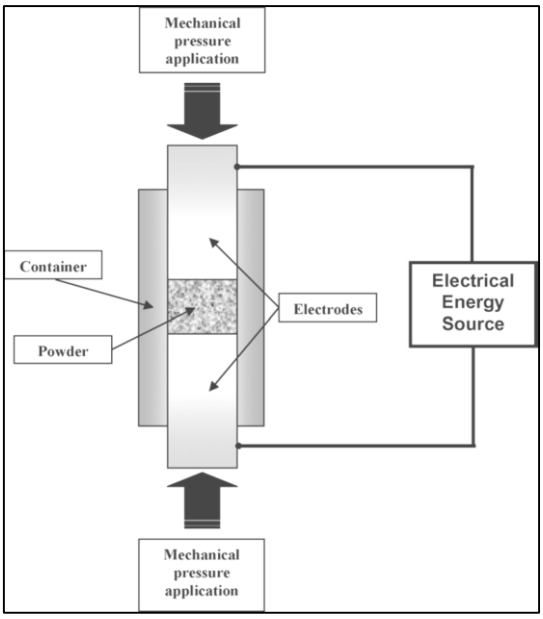

Figure 4: Basic representation of FAST **[98]**.

Their results are based on theoretical and experimental considerations of the role of applied pressure on the material. Quach et al [99] also studied the yttria stabilized zirconia using FAST with various sintering temperatures. Their results on that application of high pressure helped in producing dense samples with a grain size of 15 nm. They concluded that densification is due to the intrinsic effect of pressure and distraction of agglomerates but the pressure had little effect when samples sintered at a higher temperature.

Choi et al [100] studied the consolidation behaviour of nano sized powder of CeO_2 ceramics. In their work the application of high pressure helps in reduction of final sintering temperature and hold time with relative density of above 97%. They also concluded that the control on the microstructure and desired grain size can be possible with appropriate parameters on FAST. Guo et al [101] studied the effect of changing the pressure during FAST method using ZrB_2-SiC-Yb_2O_3. The application of high pressure at the final sintering temperature removed the

volatile species by evaporation which was helpful for avoiding the micro cracks and the formation of SiO_2 in this system.

Comparing previous experiments on the understanding of the application of pressure in FAST leads to the following three major points:

1. Applying mechanical pressure helps in improving the density and reducing the final sintering temperature.
2. Applications of mechanical pressure helps the particles to bond. It also helps to remove the volatile substances formed during sintering and avoid maximum porosity.
3. When nanopowders are used, the application of pressure helps to avoid the formation of nanoparticles agglomerates.

1.5.3 Effect of electric current on the FAST process

The application of electric current for the sintering of powder materials is not a new topic. It was patented in the USA in 1922 [98]. The patent states that production of dense materials can be achieved by applying electric current through the samples which helps to reach the appropriate sintering temperature [98]. FAST works under the principle of resistance sintering method. In this technique, the electric current and mechanical pressure is applied to consolidate the powder. Conductive and non-conductive powders can be sintered by using electric current [102]. In the case of conductive powders, pulsed DC current will pass through the materials and create joule heating effect for densification but non-conductive powders need to be packed with the use of a conductive die which helps the densification of the powder material [103]. Typical conductive dies are made of graphite, copper and stainless steel. For the FAST processing of the glasses in this project, a graphite die was used.

Resistance sintering has been around for more than 50 years with different names. Currently few companies have commercialized resistance sintering equipment [98]. This resistance

sintering equipment is commonly known as spark plasma sintering even though the existence of plasma is questionable.

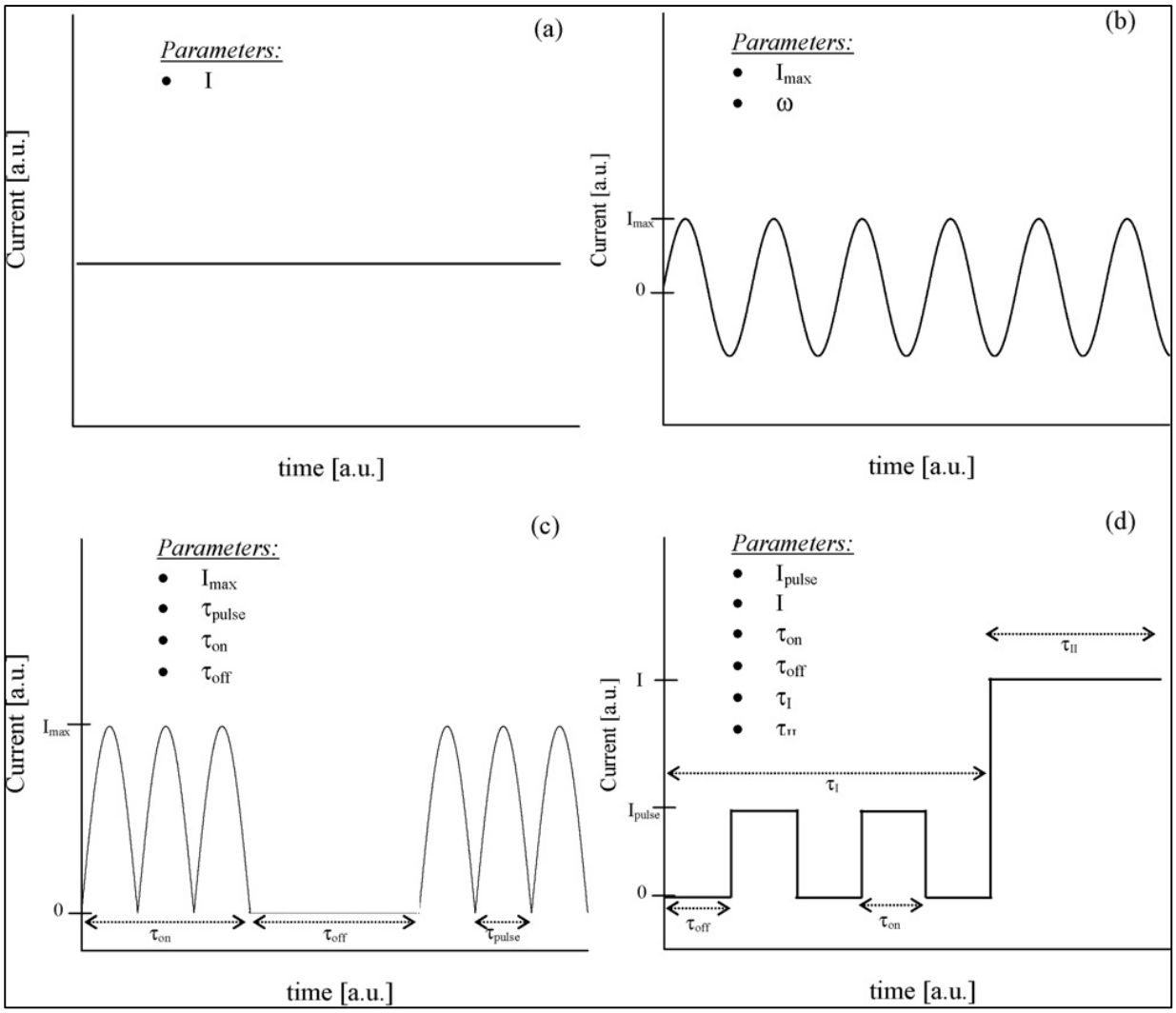

Figure 5: Types of the electric current applied in resistance sintering [98].

Resistance sintering can be divided into four types based on the current. Figure 5a shows the first type constant DC current [98]. In Figure 5b AC current is applied. Figure 5c shows the pulsed DC current and Figure 5d is a two stage current applied; at the first stage pulsed DC was applied and later constant DC current is applied [98].

1.5.4 Temperature distribution in SPS

Few research groups investigated the temperature distribution during SPS Process. Wang et al [104] investigated the temperature difference inside the die by 2D modelling. They concluded that:

1. Higher thermal conductivity decreased the temperature difference.
2. Temperature difference was directly related to the heating rate.

Zavaliangos et al [105] proposed a detailed finite element analysis study to understand the temperature evolution during the sintering process in SPS. They analysed the temperature distribution in the radial and axial direction. They tried to decrease the finite element calculation from the objective of Joule's heating generation inside and outside of the die setup of SPS process. Their observations showed that there is a co-relation between the surface and the sample temperature.

A more similar study was conducted by Vanmeensel et al [106, 107]. They designed the experiment in order to validate the finite element model. They carried the experiment using titanium nitride as an electrical conducting and zirconia as insulating material. According to their setup, using titanium nitride a conductive material the applied current should passes through the material and using zircona a nonconductive material the current should pass through the graphite die. The results of their experiment concludes that there is large inhomogeneous distribution of temperature during the sintering of the samples, mainly due to the nature of materials. Because of such temperature distribution, a close guideline was proposed to capture a temperature profile. It was suggested, that the pyrometer was placed at the bottom of the bore hole inside the upper punch of above 5 mm away from the sample centre. This can ensure better control over the distribution of temperature. Tiwari et al [108] studied the same effect with different thermal conducting type of powder. For the simulation study MATLAB and ABAQUS were used and the following points were made:

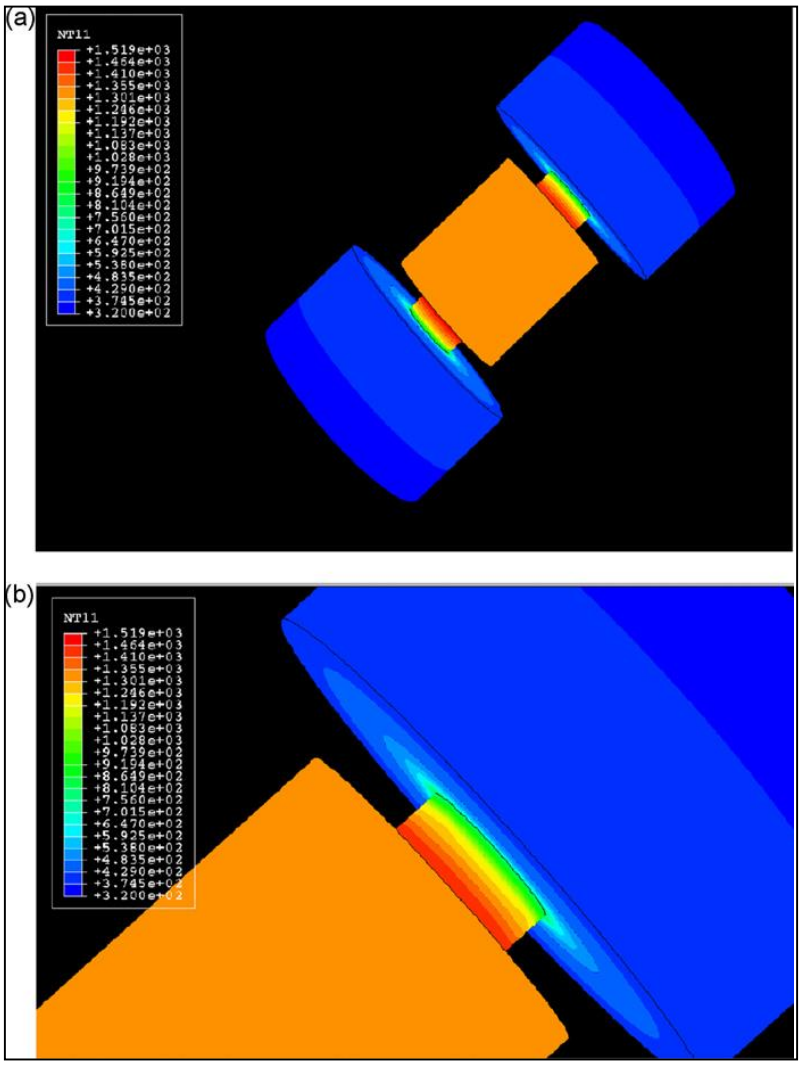

Figure 6: ABAQUS FEM simulations visualizing the temperature distribution on the die and punch surface after 450s operation of spark plasma sintering at a constant Joule heat density of $1.25x10^7$ W/m^3: (a) overall view of the entire system of graphite plate/punch/die system and (b) closer view of the region of top punch and graphite punch/graphite plate interface [108].

1. The difference in the temperature at the centre of samples is related to different input of power supply.
2. Their simulation study showed that max temperature is attained at the punch region and the graphite plate remains at the room temperature at the steady state.
3. In the transient condition, the die surface remains much lower than the temperature at the punch region.

4. The maximum level of current density is attained at the central part of the graphite die and the punch where the sample is placed during the steady state condition.
5. The simulation results suggest that uniform distribution of temperature at die and punch assembly during steady state of current flow

1.1.5 Densification mechanism

The densification process in FAST was to be believed that at initial stage the pulsed DC current generates the spark discharge between the powder particles. The plasma was generated by ionizing the gases present in the sample [109]. The generation of both spark and plasma eliminate the gases and oxide layer formed on the surface of the powder particles. In that way, the surface of the particles are cleaned and activated, this provides a diffusion bonding of the boundary particles. This will activate the densification of the compact [110]. Because of the existence of spark discharge and the plasma between the powder regions this process is called the Spark Plasma Sintering, even though the lacking of the evidence of plasma and spark discharge in addition to that there is no evidence on the effects of pulsed direct current on the densification of the conducting powders has explored well.

1.5.6 Application of FAST in Biomaterials

Recently, there has been a wide interest in applying FAST in order to prepare bioceramics for medical applications. FAST was used to fabricate hydroxyapatite (HA) and related products. Gu et al [111] reported that HA prepared by this technique showed densification of 99.6% at a sintering temperature of 950^{o}C with a holding time of 5 min. HA fabricated by FAST showed no phase change at 950^{o}C but it started to decompose when the temperature was increased to 1000^{o}C. The mechanical properties like micro hardness and Young's modulus showed increased value when compared with conventional sintering. Yu et al [112] used FAST to study the effect of post heat treatment of HA coating on Ti rods after plasma spray to understand the effect on the in vitro properties of the HA coating. They heat treated the coated

HA at various temperatures and one sample with prolonged hold time with 100°C/min as a heating rate. They concluded that FAST should be the reason for accelerated growth of apatite layer on HA coating over Ti substrate. Some researchers used FAST to produce transparent apatite based materials for biomedical applications [113]. Kawagoe et al showed that transparent beta tri-calcium phosphate ceramics can be prepared using FAST with average reduced sintering temperature by 200°C for shorter holding time when compared with conventional method of 1000°C. They also reported grain size of 1.5μm for the β- tri-calcium phosphate sintered at 1000°C with almost no pore. FAST was used for alloying by Zou et al [114] in order to fabricate nano-/ultrafine grained Ti–35Nb–7Zr–5Ta alloys. Their results showed higher value of mechanical properties when compared with conventional methods and also the near full density was achieved at 1373K which is 600K lower than the conventional methods. HA composites of Ti_3SiC_2/HA was prepared using FAST at the temperature of 1200°C with a heating rate of 200°C/min under the pressure of 60 MPa for 5min holding at the final temperature. The density of fabricated samples was higher than 96% of the theoretical density. The XRD of the samples showed no interaction between Ti_3SiC_2 and HA. The mechanical testing of these composites showed a decreased Vickers hardness and increased elastic modulus when the composition of Ti_3SiC_2 was increased. Moreover the bending strength and fracture toughness were also improved with increasing the amount of Ti_3SiC_2 [115]. SiO_2 doped HA was fabricated using the FAST method. Amorphous Si-HA was prepared by an aqueous precipitation route by adding 1, 3, and 5 wt% of SiO_2 to pure HA. The above mixture was used in FAST heating at 1000°C with 3 min holding time at the heating rate of 100°C/min. The XRD of the pure HA showed no phase change with near theoretical densification of 97%. The XRD of Si-HA on the other hand, showed the formation of β-TCP with increasing intensity in XRD when the weight percentage of SiO_2 was increased. The densification of the doped samples decreased at 94% with the formation of intergranular

porosity. The Young's modulus of the Si doped HA was increased compared to pure HA. The increase in Young's modulus can be attributed to the suppression of grain coarsening during the FAST process. A decrease in the hardness value was also observed. Their doped HA samples showed also a better cell proliferation ability to compare with pure HA [98].

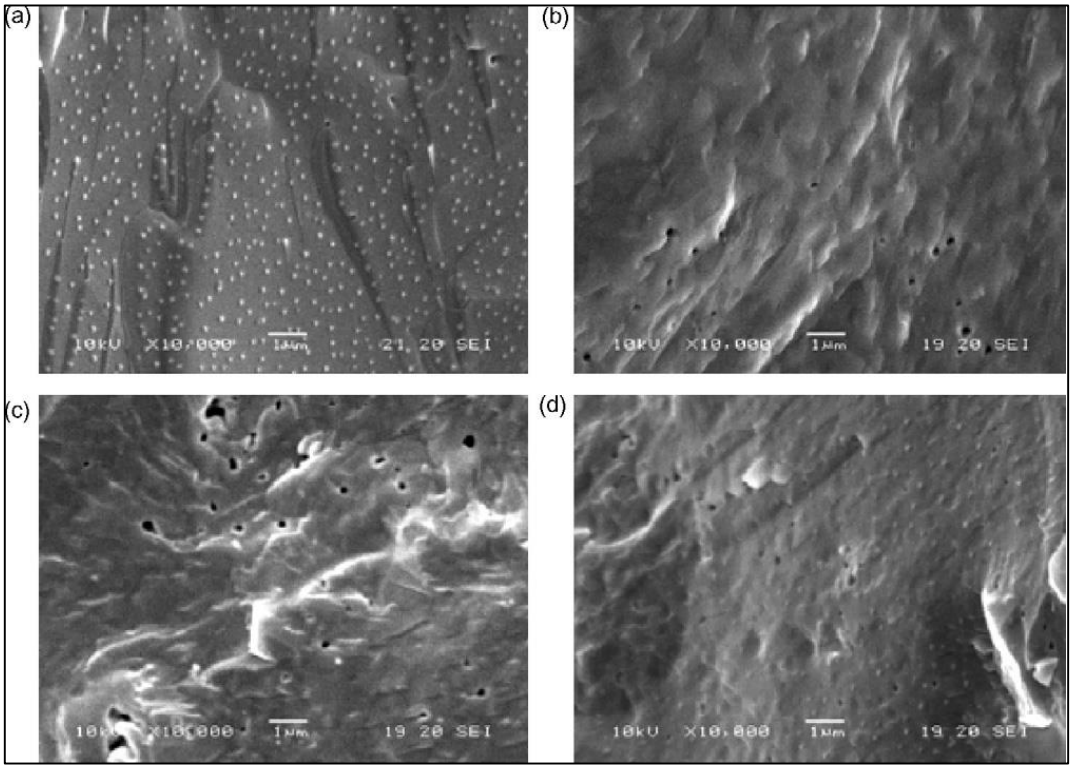

Figure 7: Morphologies of various HA-based SPS compacts: (a) ceramic HA; (b) ceramic 1 wt % Si-HA; (c) ceramic 3 wt% Si-HA and (d) ceramic 5 wt % Si-HA [98]

Recently, silver substituted HA received much attention due to its anti-microbial properties. HA with 5 weight percentage of silver was consolidated through FAST with the parameters of 1000^{o}C for 2 min at 40 MPa pressure. The XRD of these sample showed the presence of HA and β-TCP. The starting materials prepared by Ag ball milled HA, Ag-coated HA and pure HA. The relative density of FAST sample was 96% and 99%. The grain size of 400-800nm were formed on pure HA. In the case of AgHA ball milled samples showed the grain size of 1-2 micro meter but coated samples showed 100-200nm with even distribution of Ag in HA compacts [116]. All previous research shows the ability of FAST as one of processing

techniques for biomaterials preparation with improved properties when compared with other conventional methods for materials preparation.

1.5.7 Application of FAST in Glass-Ceramics

The chalcogenide glass with the composition weight percentage of $62.5GeS_2–12.5Sb_2S_3–25CsCl$ was prepared by a melt quench method. The obtained powder was milled in an agate motor and pestle. These powders were used in FAST using the parameter of 290^oC as sintering temperature with 100 MPa as holding pressure at the heating rate of 100^oC/ min. The mechanical properties of these glass ceramics were improved significantly. For example, Vickers hardness was increased to 141 HV. FAST processed samples showed good optical properties with shorter time of sintering when compared with conventional thermal treatments [117]. Erbium doped lithium aluminosilicate glass was prepared using FAST technique (Figure 8). The parameters used for FAST processing are 800 to 900^oC as densification temperature with pressure of 35 and 53 MPa and heating rate of 200^oC/min. The obtained samples were 2 to 3 mm in thickness. The lithium aluminosilicate (LAS) glass ceramic powders were prepared by sol-gel method. The optical characterization of theses glass ceramics showed a decrease in IR emission which is due to residual porosity. The density of the samples reached near theoretical density of 96% [118].

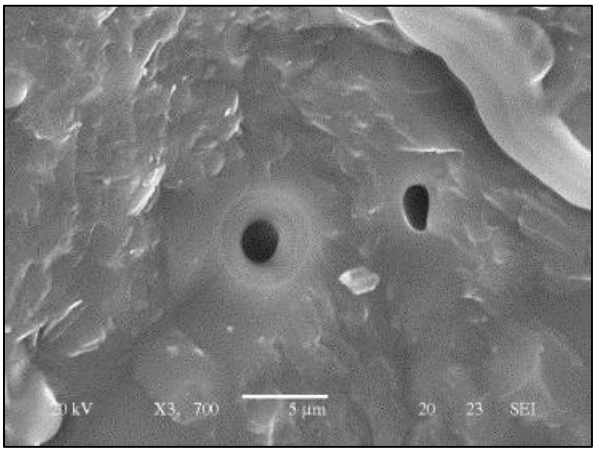

Figure 8: Er-doped LAS glass ceramic prepared by FAST showing residual porosity [118].

Transparent glass-ceramics containing $LiTaO_3$ nano crystals in an aluminosilicate glass system were prepared using FAST. The XRD diffractogram and the FTIR spectrum of these samples showed the presence of $LiTaO_3$ nanocrystals. The crystal size of $LiTaO_3$ was calculated using XRD. The crystal size ranged from 14 to 36 nm. The dielectric constant of this glass ceramic was also increased when compared with the glass matrix. The absorption of NIR fluorescence spectra showed the presence of Nd^{3+}:$LiTaO_3$ nanocrystals [119]. Most of previous research using FAST technique in glass ceramics is towards the optical applications only but this investigation shows that an alumino-silicate glass system can be used in FAST for the production of glass ceramics. In this research the alumino-silicate glass system with the composition of $4.5SiO_2$-$3Al_2O_3$-$1.5P_2O_5$-$3(X)O$-$2(X)F_2$ was studied. Previous research was concentrated only to FAST sinter HA and doped HA. There has been very little amount of research published using FAST technique for producing glass ceramics. All previous research was focused on the optical application of the materials. Therefore this research work is a first attempt for using FAST in the production of glass ceramics for biomedical applications.

1.6 Extrusion of Alumino- silicate glass for tissue engineering scaffold application

In tissue engineering the scaffold plays a critical role for the growth of cells either by seeding with in or from the surrounding tissues through migration [120]. The scaffold geometry helps in loading or packing the cells and delivering them to the specific area [121]. In order to perform these functions the scaffold substrate should provide suitable environment for cell growth, attachment, proliferation, and migration [121]. The properties required in order to develop a biomaterials scaffold are:

1. To support and deliver cells
2. To stimulate cellular response
3. To provide a wound-healing barrier
4. To be biocompatible and biodegradable

5. Easy process ability and malleability into desired shapes
6. High porosity with large surface/volume ratio
7. To possess mechanical strength and dimensional stability
8. sterilisability,

Generally, three-dimensional porous scaffolds can be fabricated from natural and synthetic polymers, ceramics, metals, and composite biomaterials [121].

1.6.1 Natural polymer and synthetic polymers for scaffolds

There are vast numbers of natural polymers which can be used as tissue engineering scaffolds for biomaterial applications. The best example for natural polymers are, collagens, elastin, and fibrinogen make up much of the body's native extracellular matrix (ECM). This ECM provides structure and mechanical integrity to tissues that controls the cell function [122]. The few examples that can be used as scaffolds are collagens (gelatine), cellulose, chitosan (chitin), pectinic acid, and starch.[123, 124]. The use of natural polymers has a few advantages over biocompatibility, process ability, and availability. Even though it has these advantages there are a few disadvantages which are a tendency to be expensive, suffer variation from batch to batch and cross contamination. Synthetic polymers has more advantage when compared with natural polymers. This synthetic polymers can also be used as biomaterials [125, 126]. Synthetic polymers can be processed easily using various techniques. These polymers can be divided in to biodegradable and non-degradable polymers[125, 127]. Their physical and mechanical properties can be adjusted according to need. Some of the non-degradable polymers that can be used as scaffold for tissue engineering applications are: polyvinyl alcohol (PVA), polyhydroxyethymethacrylate (PHEMA), and poly (N-isopropyl acrylamide) (PNIPAAm) are few examples. Degradable polymers includes poly(α-hydroxyl esters) such as polyglycolide (PGA), polylactide (PLA) and its copolymer poly(lactide-*co*-glycolide) (PLGA), polydioxanone (PDO), and biodegradeable polyurethanes[122, 123]. Out of these two types,

biodegradable polymers are mostly preferred for tissue engineering applications because they minimise the chronic foreign body reaction and lead to the healing of deceased tissue and serve as a temporary scaffold for both mechanical and biochemical support in the human body.

1.6.2 Bioceramics for scaffolds

Bioceramics are a one of the part of biomaterials which are prepared by melting or sintering, of inorganic raw materials. Bioceramics may be crystalline or amorphous materials but they should be biocompatible in nature[128]. Bioceramics are mainly used in conjunction with metallic implants as coating materials. Porous bioceramics are mainly used as scaffolds. The major elements in of bioceramics are calcium (Ca), silica (Si), phosphorus (P), potassium (K), and sodium (Na). These ceramics can be classified as inert, semi-inert, and non-inert. Some of the inert bioceramics are alumina (Al_2O_3), zirconia (ZnO_2), silicon nitride (Si_3N_4), and carbons (C). Certain glass ceramics, such as dense hydroxyapatites and fluorapatite are bioactive; and calcium phosphates, aluminium calcium phosphates, coralline, tricalcium phosphates, zinc calcium phosphorus oxides, zinc sulphate calcium phosphates, ferric calcium phosphorus oxides, and calcium aluminates are biodegradable ceramics[123]. Out of these bioceramics only synthetic apatite and calcium phosphate minerals, coral-derived apatite, bioactive glass, and demineralised bone particle are widely used in hard tissue engineering due to the results of extensive research and development being available [120, 123, 124].

1.6.3 Methods of scaffold fabrication

Engineering scaffolds are most useful for treating the deceased organs in the body. This scaffold supports cells and tissue adhesion and provides enhanced healing around the deceased site of the implant [126, 129]. The requirements of the tissue engineering scaffolds are large surface area and pore size of minimum 100μmwith interconnectivity in a three dimensions. Porosity plays a major role in providing an adequate space and allowing cell suspension in the three-dimensional structure [129]. This pore structure promotes extra cellar matrix production,

transporting nutrients from nutrient media, and excreting waste products. Adequate pore size and uniform distribution with interconnected pore is necessary for the equal distribution of cells in the scaffold [130]. There are various methods and mechanisms available to achieve the above properties to fabricate a scaffold, which are listed in the Table 1 Comparing commonly used methods for the fabrication of bioceramics scaffolds a different method of approach was attempted to fabricate a glass ceramic scaffold. The method that was followed is a common engineering technique, called extrusion, which is used for shaping of ceramics, glass, and many other materials. In this work honeycomb extrusion was used to produce the porous glass for scaffold applications.

Table 1: Various methods of scaffolds fabrication technique [131]

Mechanism	**Methods**
Leaching method	Solvent-casting/salt-leaching method, Ice particle–leaching method,Gas-foaming/salt-leaching,method.Gel-pressing method
Microsphere	Biodegradable microsphere,Macro porous bead ,Particle-aggregated scaffold
Phase separation	Freeze-drying method,Thermally induced phase separation,Centrifugation method
Injectable gel	Polyphosphazene gel
A cellular method	Decellularisation process
Keratin scaffold	Self-assembled process
Fibre spinning	Nanofibre electro spinning process,Microfiber wet spinning process,Nonwoven PGA fibre
Printing and prototyping	Inkjet printing process Melt-based rapid prototyping
Functional scaffold	Growth factor release process
Ceramic scaffold	Sponge replication method,Simple calcium phosphate coating

1.7 Honeycomb extrusion process

In order to obtain successful honeycomb products the powdered materials need to be mixed with the binding agents in a ratio to form a paste that retains its shape after the extrusion and sintering processes. The extrusion of honeycombs needs the materials to be viscoelastic to form an extrudate [132]. The melt based shaping and paste based shaping of honeycomb can be done if the material is plastically deformable [133]. Glass is good example for the melt based extrusion. The glass melt is fed through the shaping die to form a solidified extrudate [134]. The melt based process is a homogeneous continuous method were as pastes are a mixture of

liquid, binder, and particles. In powder extrusion binder plays the important role in forming a visccoplastic materials [134]. In order for a powder to be plastically shaped the binder selection and mixing is critical. The binders must not leek through the packed particulate during application of pressure. The role of the binder is to form a paste which can create sufficient yield stress to maintain the shape of wet-green body upon exiting the die [134]. The binder is often a soluble high molecular weight of polymer. The required concentration and molecular weight depends on the particle size of the materials to be bonded. This concentration can be low for the materials like clay but higher for the inert solids such as glass powders [135]. The total binder system may contain a liquid, surface active agents such as lubricants, and plasticisers [135, 136].

1.7.1 Honeycomb geometry

The honeycomb structure is a linear cellular structure, which is popular in the automobile industry as catalytic supports [137]. This type of honeycomb has two type of pores structure which are the channel pores and microstructural pores [137, 138]. The channel geometry of the extruded ceramics or glass materials can be any shape which are reflection of the design of the honeycomb die. There are many varieties of honeycomb shaped ceramic compositions that are fabricated and commercially available in market which includes alumina, carbon, cordierite, fused silica, mullite, potassium borosilicate glass, and silicon carbide.[136]. The various channel geometry structures and compositions are formed to meet the requirements of the specific applications. Honeycomb structures can be obtained by direct extrusion using the honeycomb die. The advantage of this method is that up to 50000 channels can be produced simultaneously. During the extrusion of the honeycomb structure the paste flows through the honeycomb shaped die. Figure 9 shows the typical honeycomb die assembly.

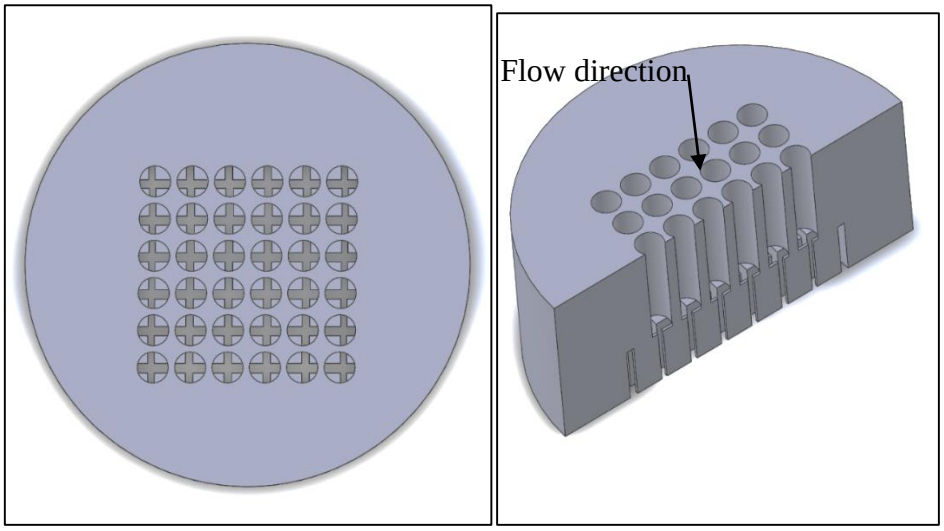

Figure 9: Honeycomb die design [136]

1.7.2 Honeycomb die design

Honeycomb structures can be formed from a plastically formable mixture or from hot melts. To manufacture a honeycomb extrusion die, precession machining of solid metal to give holes on one side and slots on other side as shown in the figure 10 is required. Such a machined die was first invented by J.J.Benbow [139]. A drilled a metal plate with an array of holes arranged hexagonal on a triangular grid and then on each alternative holes they screwed hexagonal bolt to form a true honey comb structure. This design helps to keep the continuous flow of the paste to form a honeycomb structure. Metal honeycomb die should be formed from high strength materials in order to avoid the deformation during extrusion. The length of the holes and slots should be calculated to have the continuous flow under the constant of reducing pressure. During extrusion, the plastic mixture will flow through the holes and spread evenly along the slots due to plasticity and form the honeycomb which then exits the die. The important feature of this kind of die is to maintain the uniform extrudate velocity across the section to avoid preferential flow which causes the internal weakness or curved extrudates. Using this type of geometry an array of channel pores can be attained in the paste materials. Figure 10 shows the schematic details of the honeycomb die

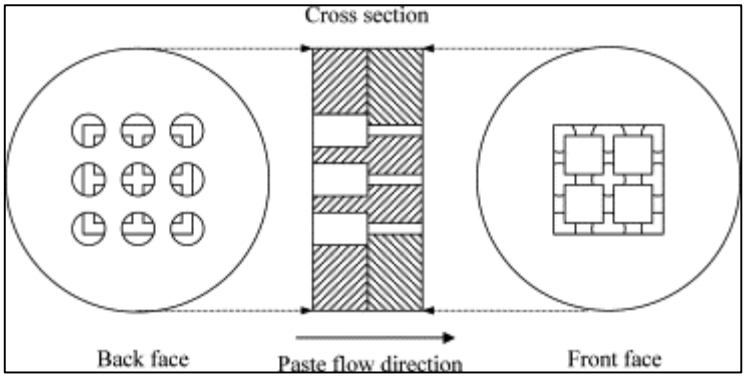

Figure 10: Honeycomb die structure design [140]

1.7.3 Types of Extruder

The extrusion process plays a major role in various industries, it is necessary to consider the types of extruder that are used for the shaping process. There are three major types of extruder that are used for the ceramic shaping process which are rotary extruders, ram extruders, and screw extruders [135].

Rotatory extruders are often used when there is no need of specific control of length of the extrudates. In this process paste is fed in between two counter rotating cylinders. One of the cylinder is solid but the other one is hollow when the rotation takes places paste are forced to flow to the tip of the rollers and creates pressure which allows the past to come out through the attached die [141].

Ram extruders are used for producing complicated geometries. The paste is fed into the barrel in batches. The ram is used to force the material to flow through a die. The ram is pressed by either hydraulic or mechanical system with given pressure, fixed force or rate. The extrudates can be treated either by cutting using a blade or it may drop. The ram extruder can be used continuously to produce the extrudates by using the suitable fed system. The main advantage of this system is accurate flow control and high pressure developed during the extrusion [141].

Screw extruder equipment is used for extruding the soft materials and continuous extrusion can be performed. The mixed paste is fed into the extruder and the screw system pushes the paste

to the end and through a die attachment to form a shape. There are single screw extruders and twin screw extruder which can be used for extrusion. In twin screw equipment the arrangements of screw rotation can be either of counter or co-rotating [135].

1.8 Paste formulation

The formulated ceramic paste can be considered to be a two phase system of binders and solid. The binder phase can be a mixture of several materials and used to support the solid phases for the shaping. Various compositions of binders and lubricants are reported for paste formulation [140]. More often this binder phase is removed either by sintering after the extrusion. The removal of binder from the materials by sintering will potentially create pores in the structure [142]. In the solid phase the properties such as particle size and shape plays major role in the paste formulation. Understanding these properties helps in the paste formulation for the extrusion process. To extrude a paste the size of the particles needs to be much smaller than dimension of the extrusion die [140]. During the paste formulation the amount solid to be added to liquid should be calculated. If the concentration of the solid particles is too high in relation to liquid higher pressure is needed for extrusion. On other hand if the liquid content is high then the extrudate will suffer from poor shape retention. Formation of paste starts with mixing of liquid and solid content. The mixing the both phases uniformly helps in producing the closely packed particles with voids filed by the binders in the interparticle region [142]. In order to obtain well mixed paste optimisation of mixing process is needed [140, 142].

1.8.1 Rheology of paste flow

Extrusion is one of the types of processing used in the ceramic industries. This method is used in catalysts production and brick manufacture. Extrusion is one of the oldest method for producing the ceramic masses and has been practiced since 1835 [135]. The first extruded product was brick made from stiff clay. To achieve the required ceramics shapes, the compounds should satisfy the necessary plasticity which is not easy to achieve. According to

Haase “plasticity is defined as the ability of a solid substance to react to externally applied forces with permanent changes in shape without loss of cohesion of the particles which form that substance” [135]. More recently Schulle proposed a definition based on the rheological behaviour of the materials. Using rheometric test researchers in the field of ceramics are able to characterise plastically deformable bodies which helps in design of extrusion materials and optimization of the process [133]. Benbow and co-workers have performed several studies on developing an understanding the rheology [135]. They used a simple capillary rheometer and were able to understand the connection between the extrusion pressure and the extrudate delivery rate [135]. These were used to formulate a paste that can be shaped.

1.8.2 Analysis of paste flow by Benbow/Bridgwater and co-workers using ram extruder

An extruder is a machine designed to generate the pressure difference required to shape the paste through a die. This pressure difference changes considerably from one material to another but the flow is common in all types of extruder [142]. The important aspect of paste extrusion is the relation between the extrusion pressure and velocity of the extrudate. Figure 11 shows a simple illustration of flow of paste in a ram extruder. The ceramic paste is confined in the barrel with a known inner diameter D_o and pressure is applied via ram to the paste until it reaches die land with the diameter of D and length L. When the paste flows through the die it will have a mean velocity V and it will have to overcome the associated wall shear stresses [142]. In this analysis two systems of flow needs to be considered the flow from the barrel to the die and the flow inside the die land. Where there is a square entry to the die a static region is produced at end of the barrel.

When pressure is applied paste undergoes a uniaxial yield stress which is denoted σ, this is assumed to be 0 due to the linear extension of stress on the planes is perpendicular to the direction of strain [142]. The amount of work done in order to increases the length of the paste l and cross section area A can be represented as dl is σA dl if the volume is unchanged.

$$A_0 l_0 = Al$$ Equation 4

Where A_o is the initial area of cross-section and l_o is the initial length, by differentiation the above equation 6 and represented as

$$\frac{dA}{A} + \frac{dl}{l} = 0$$ Equation 5

Or

$$\frac{\mathrm{dA}}{A} + \frac{A\,dl}{A_0 l_0} = 0$$ Equation 6

The amount of work done is this:

$$\int_{Ao}^{A} -\frac{\sigma A_0 l_0 dA}{A} = [-\sigma A_0 l_0 InA]_{A_0}^{A} = \sigma A_0 l_0 ln(\frac{A_0}{A})$$ Equation 7

Considering the paste is extending from the barrel by forcing it from a barrel A_o through the die. The amount of work done by extrusion pressure for extrusion is P which is $P_1 A_o l_o$ by equating this expression for the circular barrel and circular die gives equation 10 [142]

$$P1 = \sigma In(\frac{A}{A_0})$$ Equation 8

$$P1 = 2\sigma In(\frac{D_0}{D})$$ Equation 9

In the flow of a paste a viscous effect is also taking place with amount of stress generated and it is related to the strain [142]. If the liquid phase is viscous it is found that $\sigma = (\sigma_0 + \alpha V)$ and hence by substituting for σ gives equation 6 [142].

$$P1 = 2(\sigma_0 + \alpha V) In(\frac{D_0}{D})$$ Equation 10

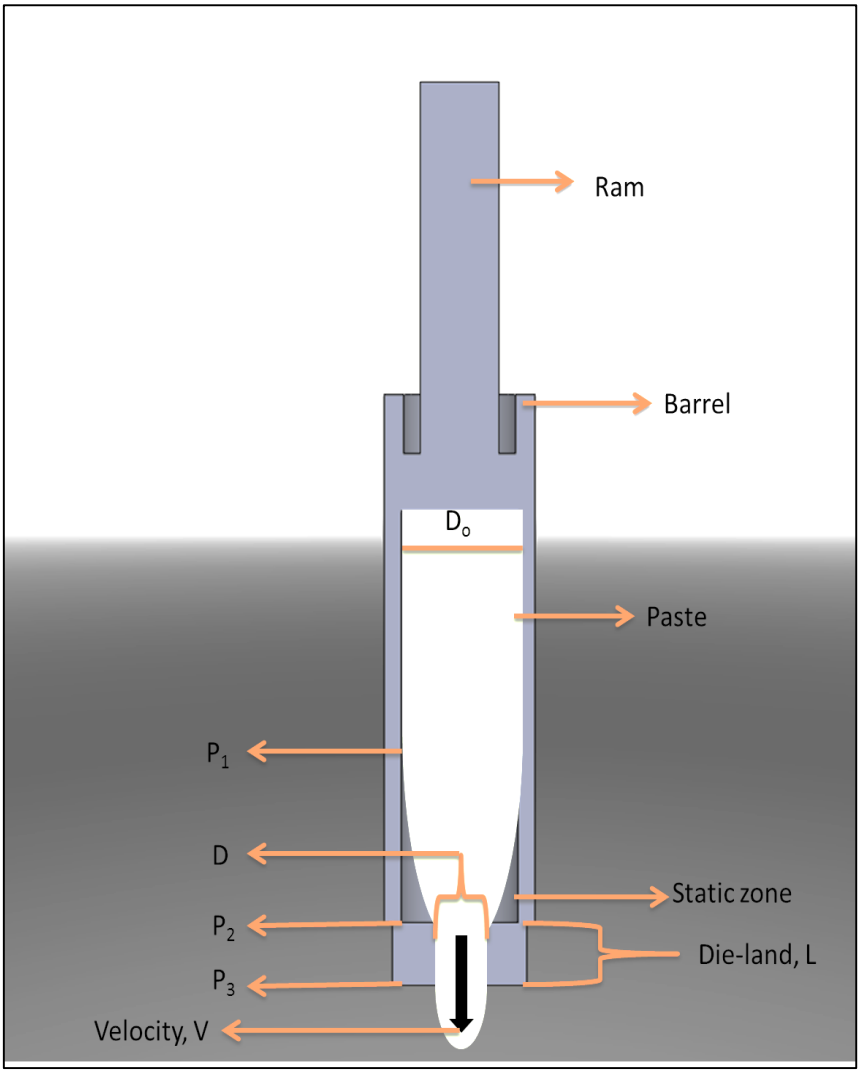

Figure 11: Illustration of ram extrusion analysis of flow[142]

Equation 11 represents the pressure drop into a circular die from a circular barrel for paste with extrudate velocity V in the die land and σ_0 is the yield stress at zero velocity and α is the characterizing factor of velocity of the paste in the die. The extension of the paste is proportional to velocity V and thus it can be related to yield stress corrected to the shear rate ($\sigma_0 + \propto V$). Positron imaging of extrusion and the sectioning of stained pastes have shown that the paste move as a plug lubricated by a thin layer at the wall [142]. This is true for the capillary at least but in convergent flow there is parabolic flow. The pressure drop P_2 in the die is opposed by the wall shear force which due to stress in die which is given in equation 12 [142].

$$P_1 = 4\tau(\frac{L}{D}) \qquad \text{Equation 11}$$

If the wall shear is due to the thin layer of liquid then V is proportional to P with a Newtonian approach then the equation 12 can be rewritten as

$$P_2 = 4(\tau_0 + \beta V)(\frac{L}{D}) \quad \text{Equation 12}$$

In equation 13 τ_0 and β represents the paste parameters where τ_0 is die wall shear stress zero velocity and β wall velocity factor which depends on the velocity at the wall. The pressure drop P during the extrusion from the ram extruder of the type shown in the figure 11 given in a form of equation 14 [142].

$$P = P_1 + P_2 = 2(\sigma + \alpha V)In\left(\frac{Do}{D}\right) + 4(\tau_0 + \beta V)(\frac{L}{D}) \quad \text{Equation 13}$$

The four parameters properties which are yield stress σ_0, bulk velocity function $\propto$, intial wall stress σ_0 and wall velocity function β are used to analyse the paste properties but in many cases the liquid phase behaves in non-linear manner and the equation 14 can be rewritten as [142].

$$P = P_1 + P_2 = 2(\sigma_o + \alpha_1 V^m)In\left(\frac{Do}{D}\right) + 4(\tau_0 + \beta_1 V^n)(\frac{L}{D}) \quad \text{Equation 14}$$

In this equation 15 m and n are the velocity exponent of die entry and die land. These increase the maximum characterizing properties to six parameters, three associated with barrel and three associated with the die. These equations set a base for the approach of understanding the pressure drop and paste properties for extrusion application. These study are based on the extension of the paste materials with the characterizing properties obtained from both the barrel and the die. This model only works on the assumption of the plug flow [141, 143-145]. The Benbow/Bridgwater model is based on the assumption that the wall shear is independent for the local pressure. In case of unsaturated material a high extrusion pressure is needed and this pressure has to overcome before the material reaches the steady state without any phase migration. [146]

1.8.3 Calculation of Pressure drop in honeycomb die

The pressure drop during the extrusion of a honeycomb structure can be calculated using the model developed by Blackburn and H.Böhm [147]. This model was developed based on the equation proposed by Benbow et al [142]. They proposed an equation based on equation 15. The honeycomb die can be broken down into four parts.

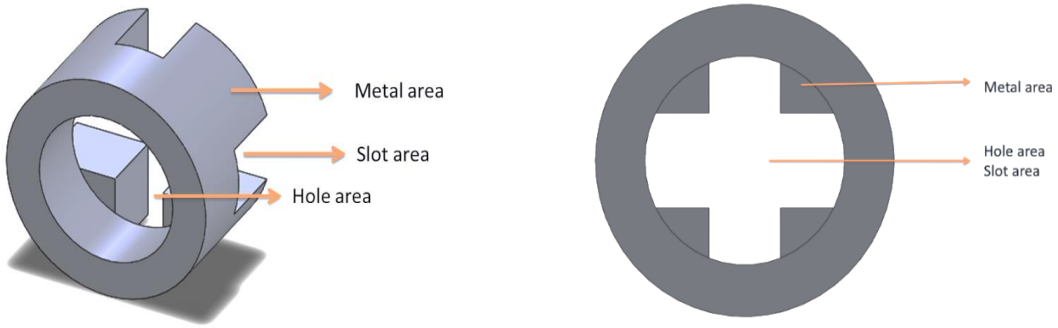

Figure 12: Area used in the calculation of holes to slot transition in the equation 17 and equation 18.

1. Entry of paste in the multiple hole
2. Flow of paste in the multiple holes
3. Transition of paste from the holes to slots
4. Flow of the paste in the slots

The modelling of the flow of the paste to the multiple hole section was carried out based on the using equation 15 to calculate the pressure drop in the honey comb die [142].

$$P_1 = Ln\{\frac{A_o}{A}\}\{\sigma_0 + \alpha_0 V^m\} + \frac{LM}{A}\{\tau_0 + \beta V^n\} \quad \text{(Six Parameter)} \qquad \text{Equation 15}$$

In equation 16 P_1 is pressure drop at the exit of multiple holes. V is volumetric flow rate that passes through N holes, A_o is the area of barrel. A is the area of N number of holes, α is the velocity factor of bulk yield stress and σ is the yield stress. m is the bulk velocity, n is the wall velocity, τ is the wall shear stress and β is the velocity factor of the wall shear stress L is the length of holes and M is the open perimeter area of the holes

The pressure drop in the holes to slot and the slot can be calculated using the equation 16 and 17

$$P_2 = \{\sigma_0 + \alpha_0 V_1^m\} \mathrm{Ln}\left(\frac{A}{A_1}\right) + \{\tau_0 + \beta V_1^n\}\left(\frac{ML_1}{A}\right) \text{ (Six parameter)} \quad \text{Equation 16}$$

In this equation P_2 is the pressure drop in the entry of the slot and the slot L is the length of slot and M is the open perimeter area of the slots and V_1 is the velocity of the flow in the slot area.

Using the equation 16 and 17 the pressure drop during the honeycomb extrusion can be calculated by adding both the equation for the four parameter and the six parameter

$$P_a = P_1 + P_2 \quad \text{Equation 17}$$

In summary the pressure drop in the honeycomb die can be calculated using the above equation. In this proposed equation the area used for calculating the honeycomb pressure drop was area of holes to slots and no alternative approach were applied [147]. Figure 13 shows the honey comb die design with the all the parameters mentioned in the equations.

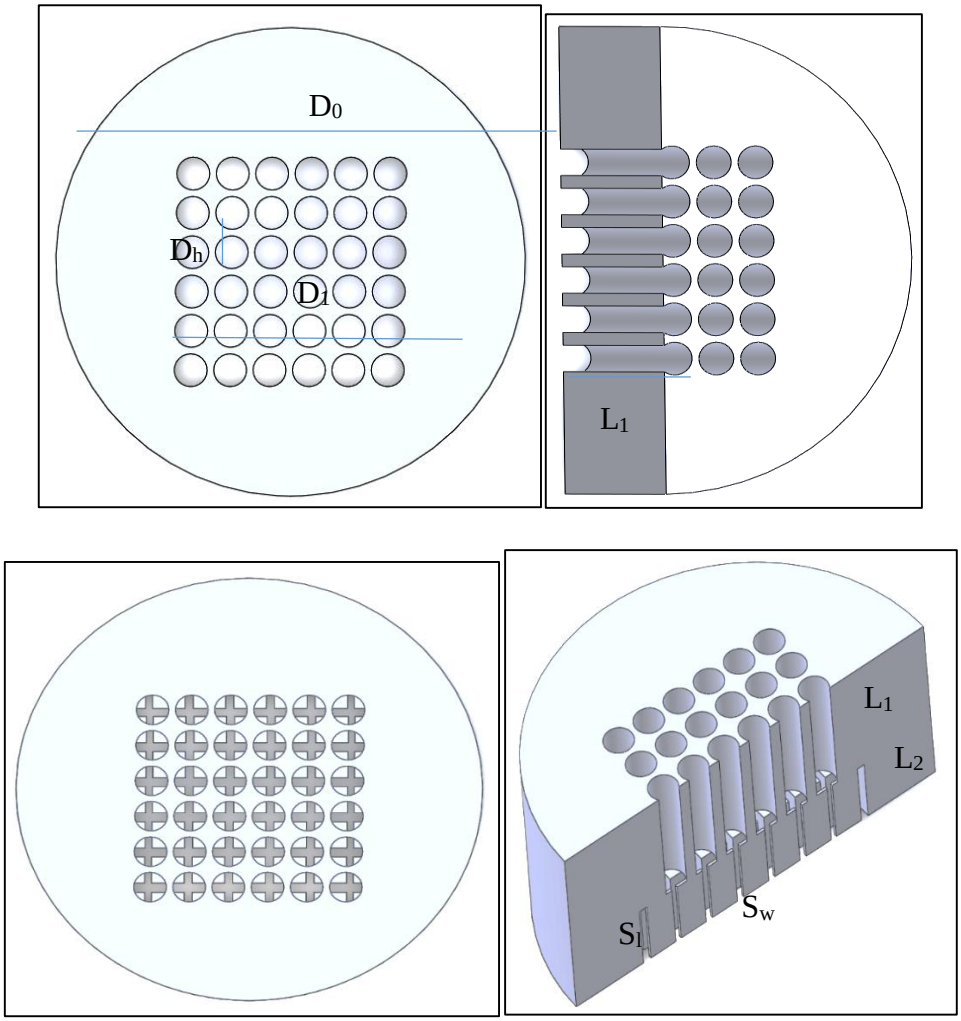

Figure 13: Honeycomb die design

1.9 Aims and objectives

The present study deals with two different processing techniques for the production of glass ceramics. The first technique is FAST sintering process and the second technique is the honeycomb extrusion process.

1.9.1 FAST sintering process

The aim of this research is to optimise the processing conditions for crystallisation of fluoro alumino silicate glasses using FAST. The sintered glasses were characterised using techniques like X-ray diffraction for crystallography analysis, microscopy for microstructural analysis, and nano-indentation for surface mechanical properties analysis. The glass with the composition of $4.5SiO2–3Al_2O_3–1.5P_2O_5–3CaO–2CaF_2$ as well as glasses with Sr and Mg substitution for Ca were studied. The obtained results from the FAST process were compared with conventional sintering to understand the differences between these two processing methods.

1.9.2 Honeycomb extrusion process

This study deals with the extrusion of glass powders using an organic binder. In the development of the processing technique, waste glass was used to optimise the extrusion rheology. The optimised conditions were used to get initial extrusion parameters for Ca, Sr, and Mg containing aluminosilicate glasses. Further optimisation was carried out for each glass system to attain the best extrusion rheology of the glass paste (glass and binder). In this optimisation process, the Benbow/Bridgwater rheology model was used. The rheology parameters obtained using the Benbow/Bridgwater model, were used to predict the pressure drop in the honeycomb die. After the characterisation of the paste parameters, 3D porous glass scaffolds were prepared. All the honeycomb extrudates were sintered using a conventional furnace. The sintered samples were characterised using XRD and SEM to understand the crystallization and the porosity generated during the crystallisation and debinding process.

CHAPTER II-Materials and Methods

2.1 Materials

2.1.1 Ca containing Alumino Silicate Glass

The Ca containing alumino-silicate glass of $4.5SiO_2$-$3Al_2O_3$-$1.5P_2O_5$-$3CaO$-$2CaF_2$ composition was produced by a melt quench route [148]. All the oxides of puriss grade silica (SiO_2), alumina (Al_2O_3), phosphorus pentoxide (P_2O_5), calcium carbonate ($CaCO_3$) and calcium fluoride (CaF_2) were supplied by Sigma-Aldrich. The required amounts of oxides were weighed out to obtain 1000 g of glass. The oxides were then mixed by shaking for 45 min. The mixture of oxides was then transferred to a platinum crucible and melted at 1475^{o}C for 1 hour using a conventional furnace (Elite Thermal Systems Ltd, Leicestershire). The melt was then quenched into cold water in order to prevent phase separation and crystallization to form frit glass. The frit glass was subsequently grounded using a TEMA mill (TEMA (Machinery) Limited, Germany) for 15 min. The obtained powder was sieved to receive fine particles of <45μm. In addition, the glasses were cast in a graphite mould with dimensions of 9 cm in length x 1 cm of width x 1 cm of depth were used for conventional sintering. The molar composition of the calcium glass is listed in Table 2.

Table 2: Molar composition of the base calcium glass**.**

Glass code	SiO_2	Al_2O_3	P_2O_5	CaO	CaF_2
LG26	4.5	3	1.5	3	2

2.1.2 Sr-containing alumino-silicate glasses

In the calcium base glass, strontium in the form of SrO and SrF_2 were introduced in the molar percentage of 25, 50, 75, and 100% (first SrO was substituted for CaO and then depending on the level of substitution SrF_2 was substituted for CaF_2). A similar melt quenching route as described earlier for the calcium glass compositions was followed for the production of the above glasses. All oxides were of puriss grade and were also supplied by Sigma-Aldrich.

Instead of SrO, $SrCO_3$ was used and the appropriate correction in the weight was calculated. The glasses were ground as described above and then were sieved to a particle size of <45 μm. The glasses cast in a graphite mould with dimensions of 9 cm in length x 1 cm of width x 1 cm of depth were used for conventional sintering. The composition of strontium substituted glasses is presented in Table 3.

Table 3: Molar composition of Sr substituted alumino-silicate glasses.

Glass code	SiO_2	Al_2O_3	P_2O_5	CaO	CaF_2	SrO	SrF_2
LG26Sr1	4.5	3	1.5	1.75	2	1.25	0
LG26Sr2	4.5	3	1.5	0.5	2	2.5	0
LG26Sr3	4.5	3	1.5	0	1.25	3	0.75
LG26Sr	4.5	3	1.5	0	0	3	2

2.1.3 Mg-containing Alumino-Silicate Glasses

Table 4: Composition of Mg substituted alumino-silicate glasses

Glass code	SiO_2	Al_2O_3	P_2O_5	MgO	MgF_2
LG26Mg	4.5	3	1.5	3	2

Magnesium containing alumino silicate glasses were prepared by replacing calcium in the base glass composition of $4.5SiO_2$-$3Al_2O_3$-$1.5P_2O_5$-3CaO-$2CaF_2$ with magnesium. The glass compositions are shown in Table 4. All the oxides were supplied by Sigma-Aldrich as mentioned previously. The glasses were produced, ground and cast following a similar methodology as described earlier.

2.1.4 Waste Glass

The waste glass powder was obtained from the Potters-Ballotini Limited UK. These glass powders were sieved to less than 45 micron. The sieved glass powder was used as the test material for the development of extrusion paste modelling method to measure the pressure drop during the extrusion process. The same mixtures of binder composition were applied to the alumino silicate glasses which were produced as part of this project, in order to measure the

pressure drop during the extrusion process. The alumino silicate glass used in the experiments are listed in the Table 5 on molar basis. The properties and potential application in biomaterials of this glass were discussed in Chapter 1. All these glasses were produced by the melt quench route. The methods of producing these glasses were discussed in section 2.1 and 2.3

Table 5: Molar composition of Alumino silicate glasses

Glass code	***SiO_2***	***Al_2O_3***	***P_2O_5***	***CaO***	***CaF_2***	***MgO***	***MgF_2***
LG26	4.5	3	1.5	3	2	-	-
LG26Mg	4.5	3	1.5	-	-	3	2

2.2 Methods

2.2.1 Processing of Materials Using FAST and Honeycombe Extrusion

2.2.1.1 FAST Sintering using FCT system

The FAST Sintering was performed using the FCT HP D 20 (FCT System GmbH, Rauenstein, Germany) at Queen Mary University of London, United Kingdom. All the sintering experiments performed under vacuum using a 20 mm of diameter cylindrical graphite die. All the ground glass powders were kept in the oven so that the powders were completely dried prior to processing.

Table 6: Sintering of calcium base glass using FCT.

Sample	Sintering temperature (ºC)	Heating rate (ºC)	Cooling rate (ºC)	Heating pressure (kN)	Holding time (min)	Cooling pressure (kN)
1	700	100	100	5	1	5
2	800	100	100	5	1	5
3	900	100	100	5	1	5
4	1000	100	100	5	1	5
5	800	100	100	5	5	5
6	900	100	100	5	5	5
7	800	300	300	5	1	5
8	800	500	500	5	1	5

The dried glass powder was confined in the graphite die and placed in between two graphite punches. A uniaxial pressure of 5kN was applied throughout the entire sintering process. A thermocouple was used to measure temperature from starting at room temperature to 400ºC. The pyrometer was used from 400ºC to the final sintering temperature. A systematic study of the sintering temperatures from 700 to 1000ºC was initially used with 1 min sintering time to study the crystallisation behaviour of these glasses. All sintering experiments were carried out under vacuum with a heating rate of 100ºC/min at 5 kN of applied pressure. Based on the results of the above experiments, sintering was finally carried out along with a holding time of 5 min at 800ºC and 900ºC and a heating rate of 100ºC/min. This experiment was carried out in

order to understand the crystallisation behaviour of glass under the increased holding time during FAST. Based on the obtained results another set of sintering experiments was carried out where the heating rate was increased to 300ºC/min and 500ºC/min. In this experiment, the final sintering temperature was set at 800ºC with 5 min holding time at 5kN of applied pressure. All the obtained glass ceramics exhibited a thickness ranging from 2 to 3 mm. The sintering programme is summarised in Table 6.

2.2.1.2 FAST Sintering using Dr Sinter

FAST sintering of glasses was performed using a Dr Sinter 515S SPS, Japan, under vacuum. The graphite die was cylindrical with an internal diameter of 10 mm. Dried glass powders were placed inside the die and confined with two graphite punches. A uniaxial pressure of 38 MPa was applied throughout the entire sintering process. A K-type thermocouple was used to measure the temperature change throughout the study. A two-step sintering procedure was carried out to obtain the final glass-ceramics.

Table 7: FAST sintering of LG26.

Sample	Glass-ceramic	Temperature (ºC)	Holding time (min)	Pressure (MPa)
1	LG26	700	5	38
2	LG26	700	10	38
3	LG26	700/750	5/0	38
4	LG26	700/750	5/5	38
5	LG26	700/800	5/5	38
6	LG26	800	5	38

The sintering experiments were conducted at three different temperatures 700, 750 and 800ºC, applying a holding time of 5 min for each temperature. The procedure involved heating a sample to the first temperature at a heating rate of 100ºC/min, holding for 5 minutes followed by heating the sample to the second temperature and holding for another 5 minutes, prior to cooling down to the room temperature. A one-step sintering procedure was also performed for comparison. In this case, the powder glass samples were heated up to the desired temperature

at a rate of 100°C/min. All sintered samples were disks with a diameter of 10 mm and a thickness of ~1.5-2 mm. Tables 7 present the sintering profiles of the calcium base glass.

2.2.1.3 Paste formulation

Table 8: Glass paste formulation

Paste	Glass	Binders	Binder content in weight percentage	Glass content in weight Percentage
Paste 1	Waste glass	Hydroxypropyl Methylcellulose + water	23 %	77%
Paste 2	Waste glass	polyvinyl butyral + Stericacid + Dibutyl phthalate + Cyclohexane	23 %	77%
Paste 3	Waste glass	polyvinyl butyral + Stericacid + Dibutyl phthalate + Cyclohexane	20 %	80%
Paste 4	LG26	polyvinyl butyral + Stericacid + Dibutyl phthalate + Cyclohexane	17	83
Paste 5	LG26	polyvinyl butyral + Stericacid + Dibutyl phthalate + Cyclohexane	15	85
Paste 6	LG26Mg	polyvinyl butyral + Stericacid + Dibutyl phthalate + Cyclohexane	16	84

The glass paste was formulated based on the water absorption test performed on each glass powder to find the exact volume percentage of binder need to form a paste. In developing this paste formulation waste glass was initially used as the trail material to calculate the pressure drop during extrusion process. In waste glass two different type of paste were formulated. Paste 1 was formulated using 23% of hydroxyl propyl methyl cellulose (HPMC) (Grade b2/15, Courtaulds, Chemicals, UK) of 4 wt% and 19 wt% of water was mixed to form a aqueous solution. This aqueous solution was mixed in 77 wt% of waste glass powder to form a glass paste.

Paste 2 was formulated using a binder composition of 26.66 wt% of polyvinyl butyral (PVB), 1.26 wt% of steric acid, 1.89 wt% of dibutyl phthalate (DBP) and 69.19 wt% of cyclohexane. 23 wt% organic binders were mixed with 77% wt waste glass as the paste 2 the paste 3 was formulated by reducing the 3 wt% of binder content. The 20 wt% of organic binder was mixed with 80 wt% of the glass as paste 3.

The organic binders were used for experimental glass powder based on the water absorption test of LG26 and LG26Mg. In LG26 and LG26Mg two glass pastes was formulated one based on water absorption test and other one with reduction of 2 wt% of organic binder. In LG26 glass 83 wt% of powder was mixed in the 17 wt% of organic binder as paste 4. Paste 5 was formulated with 85 wt% of glass and 15 wt% of binder content to form a glass paste. In LG26Mg 82% of glass powder were mixed in the 16% of organic binders to form a paste 6. This glass paste was formulated by reducing the 2 wt% from the values obtained in water absorption test.

2.2.1.4 Paste characterisation

Pressure drop during the extrusion of glass paste were characterised using both four and six parameter model proposed by Benbow/Bridgwater using the equation 14 and equation 15 [142]. Paste was placed in the barrel with the diameter of 25.4 mm. This glass paste was tapped using the wooden rod to remove as many air bubbles as possible. The paste were extruded through a circular die with 3 mm diameter. Three dies were used with the L/D ratio of 1, 8, and 16 using the extrudate velocity of 0.059, 0.023, 0.011, 0.005, 0.002 and 0.001 $m \cdot sec^{-1}$. All the pressure was recorded using attached load cell. The calculation of pressure drop was carried using computer programs for the automated calculations developed by L.Swain 2013. This process was carried out for all the 6 pastes given in the table 8

2.2.1.5 Honeycomb Extrusion

All the pastes modelled using the Benbow/Bridgwater equations [142] were passed through the honeycomb die with the geometry given in Figure 13. The geometry of honeycomb die used in this experiments were similar to the one used by S.Blackburn and H.Böhm [147]. The various extrudate velocities and the force required to form an extrudate were recorded using the attached load cell on Instron mechanical testing machine. The expected pressure drops for the pastes were calculated by the using equation (17 and 18) and from the paste parameters derived by the methods given in section 3.1.3.4 The percentage difference of between the experimental values and the theoretical values were also calculated for the honeycomb equations.

2.2.2 Characterization techniques

2.2.2.1 Density Measurements

The density of all FAST samples was measured following the Archimedes Principle. Samples were weighed in air and distilled water separately. The density of glass ceramics was calculated following Equation 1. In order to find the water absorption of the samples and to identify porosity in the glass ceramics, the weight of the immersed sample was also measured in air.

$$Density = \frac{Weight\ of\ glass\ in\ air\ X\ Density\ of\ distilled\ water}{weight\ of\ dry\ glass - weight\ of\ immersed\ glass} \qquad \text{Equation 18}$$

The density of distilled water is 0.9973 g/cm^3. All measurements were conducted at room temperature.

2.2.2.2 X-ray Powder Diffraction

X-ray diffraction analysis was conducted for all FAST sintered glasses. The X-ray diffractograms were obtained using a Philips Panalytical X-Pert X-ray diffractometer. The diffractograms were obtained from 2θ = 10° to 60° with a step size of 2θ = 0.0200° and Cu Kα at 40 kV and 40 mA.

2.2.2.3 Vickers Hardness experiments

The hardness of all samples was tested using the Vickers hardness technique. The specimens for the H_V experiment were tested in accordance with the ASTM standard C1327-08 [149]. A Vickers micro intender (MVK-H1 Mitutoyo, UK) fitted with optical microscope was used to measure the H_V of the samples with a load of 100g for 10 s. The surface of the specimens was mirror polished with 800 and 1200-grit silicon carbide discs prior to testing. The indenter had a pyramid shape with an angle of 136º and a square base. Five indents were applied on each sample surface to receive an average hardness value. The indents on the samples surface were observed under SEM (Joel 6060) and two diagonals of each indentation were measured and averaged. The hardness was calculated using Equation 19.

$H_v = (1.854) \times (P/D^2)$ Equation 19

Where H_v is the Vickers hardness number in (Kg/mm^2), P is the applied load in Kg and D is the average diagonal length in mm. The hardness values were converted to GPa using Equation 20 [150]:

$H_v\ (GPA) = 9.81 / (1000 \times H_v)$ Equation 20

2.2.2.4 Fracture toughness

The fracture toughness of selected sintered samples surface was measured from the micrograph of the indentation made using a Vickers hardness indenter. A load of 2 Kg was applied for 10 sec on the mirror polished samples. The principle behind this technique is to generate a crack on the diagonals of the indent surface. 5 indents were placed on each sample and average values were taken. The indent surface was observed in the SEM to measure the crack length (2a) as well as the indent diagonals (2c). The surface fracture toughness of the samples was measured using the Anstis formula (Equation 21) [151].

$K_{Ic}=0.016(E/H)^{1/2}(P/C^{3/2})$ Equation 21

Where K_{Ic} is the fracture toughness, E and H is the Young's modulus and hardness (HV), respectively, P is the load applied in Kg and C is the length of the crack in mm.

2.2.2.5 Nano indentation

During nano-indentation, the surface of materials is indented by application of load using an indenter. The tip of the indenter is made of diamond or is diamond coated. Using the nano indentation, it is possible to measure mechanical properties like elastic modulus, hardness, and fracture toughness. In this work, nano-indentation was used in order to measure the elastic modulus and hardness of materials.

The glass ceramic samples sintered using Dr Sinter were indented at Queen Mary University of London using a UMIS 2000 nanoindentation instrument (CSIRO, Linfield, NSW, and Australia). The elastic modulus of sintered samples was measured using a series of 49 indents

placed on the samples using a spherical indenter with the nominal radius of 5 μm. The indentation modulus was calculated from the slope of the tangent from the indentation hardness data. A partial-unloading method was followed for each indentation test that consisted of 40 load increments. Unloading of 75% of each load was followed between increments. The nanoindentation data were collected from sample surfaces using a square of 7X7 arrays with 20 μm spacing between each indentations.

The glass samples sintered using the FCT system were indented at the University of Birmingham using the NanoTest (MicroMaterials, UK) facility. During this experiment, 36 indents were conducted using a pyramidal indenter and an average load of 300mN at a rate of 15 mN/s. The load was held for 30 sec before retrieval with 15 mN/s of retrieval was applied. The mean hardness and mean E-modulus were calculated.

2.2.2.6 Scanning Electron Microscopy

Microstructural studies of selected sintered samples were carried out using a Joel 6060 scanning electron microscopy (SEM) for the glasses sintered at the FCT system whereas an EVO ZEISS was used for the glasses sintered using Dr Sinter. The microstructural study was carried out after chemical etching using 48% hydrofluoric acid for 1 sec. The etched samples were carbon coated in order to make the sample conductive for image analysis. SEM images of Vickers hardness and fracture surfaces were captured.

Chapter III: Results and Discussion

3.1 FAST Sintering of Glass using FCT-System

3.1.1 Temperature profile and relative shrinkage on crystallisation of glasses

Figure 14 shows the sintering program of both LG26 and LG26Sr glasses using FAST. These results were obtained using a pyrometer fitted on the top of the graphite die. The results were generated based on the programme temperature used for sintering. The sintering temperature and the movement of the upper punch for compacting the glass powder was recorded in the computer programme attached with in the FCT system. Due to pyrometer limitations, the temperature and movement of the upper punch was recorded only from 400°C to the relevant maximum temperature. A thermocouple was used for monitoring the sintering temperature below 400°C but only the pyrometer reading was taken into consideration due to the lack of accuracy of temperature and punch movement measurements.

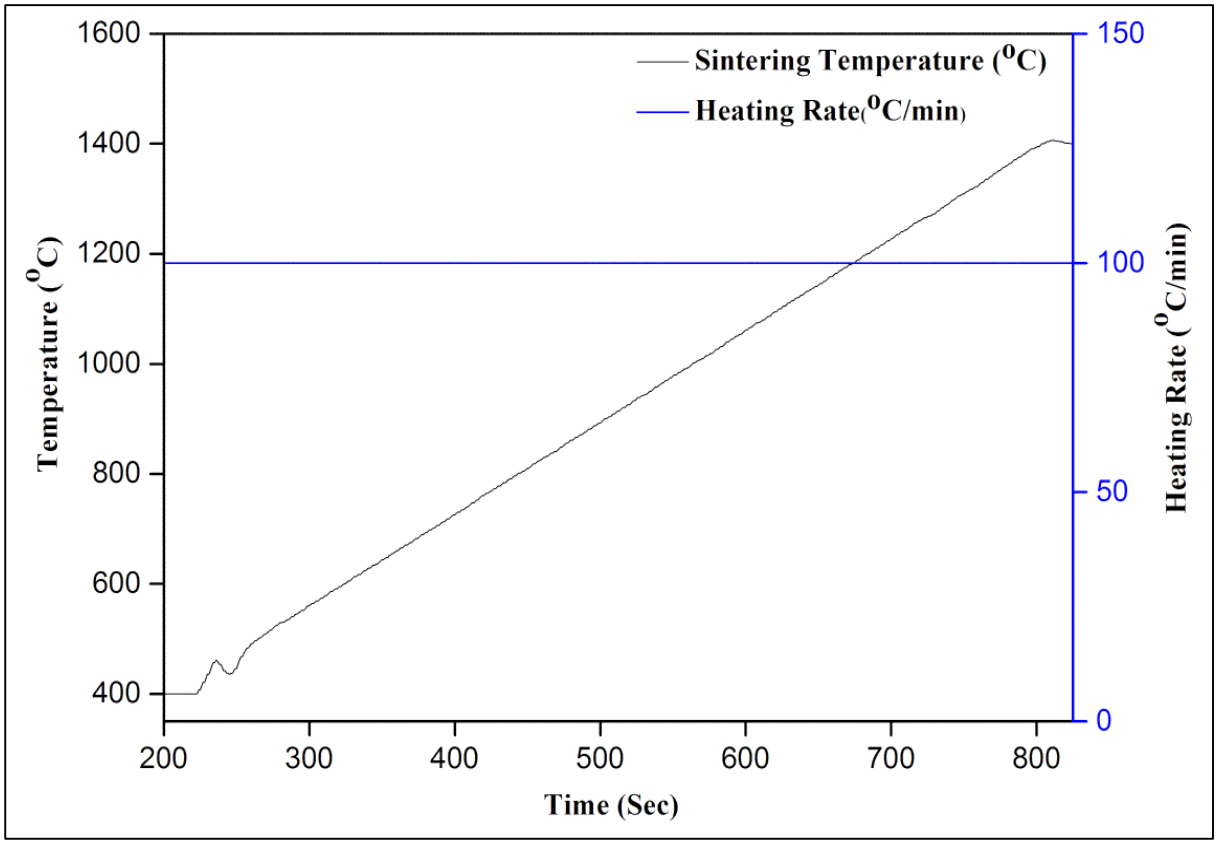

Figure 14: LG26 glass sintering profile in relation with time, temperature and heating rate.

Since the FAST method was used for the first time in order to sinter these glasses and no high heating rate DSC thermal analysis data for the crystallisation of glasses were available, a trial and error method of sintering was carried out. A 5 g of glass powder was used initially with particle size less than 45 µm. The glass powder was placed inside the graphite die between both upper and lower punch and surrounded by graphite foil inside the graphite die. The diameter of 20 mm graphite die was used and the powder was packed closely using a hydraulic pressure before the heat treatment. This graphite die was heat treated up to 1400 ^{o}C under a constant heating rate of 100 ^{o}C/min with an applied force of 5 kN throughout the heat treatment process. The experiment was designed for developing an understanding of the behaviour of glasses at high heating rate and constant pressure.

In the FAST sintering process the application of pressure increased the packing density of the powder particles. In Figure 15, the relative punch movement was shown in accordance with the temperature which shows the packing of LG26 glass powder during the sintering process.

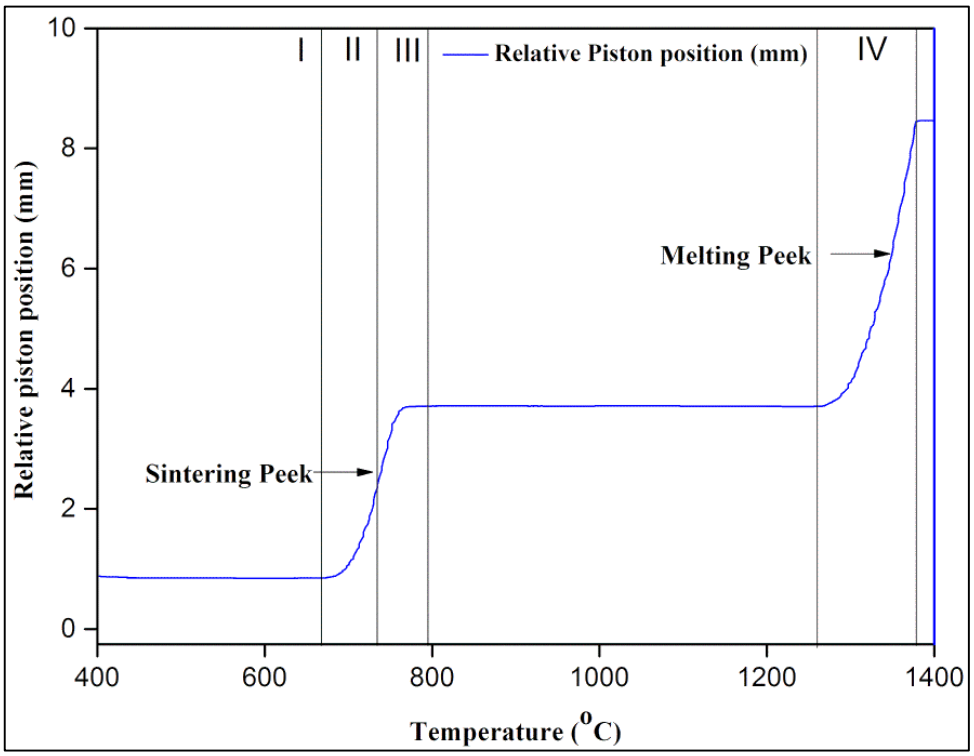

Figure 15: Relative punch movement during the heat treatment of LG26.

The piston position can signify the following four stages:

I. Increased packing density

II. Increased diffusion of the power particles

III. Removal of the pores by diffusion

IV. Melting or breaking of the graphite die

Figures 16 and 17 present the rate of shrinkage and piston movement that took place during the FAST sintering of LG26 and LG26Sr, respectively, against the sintering temperature.

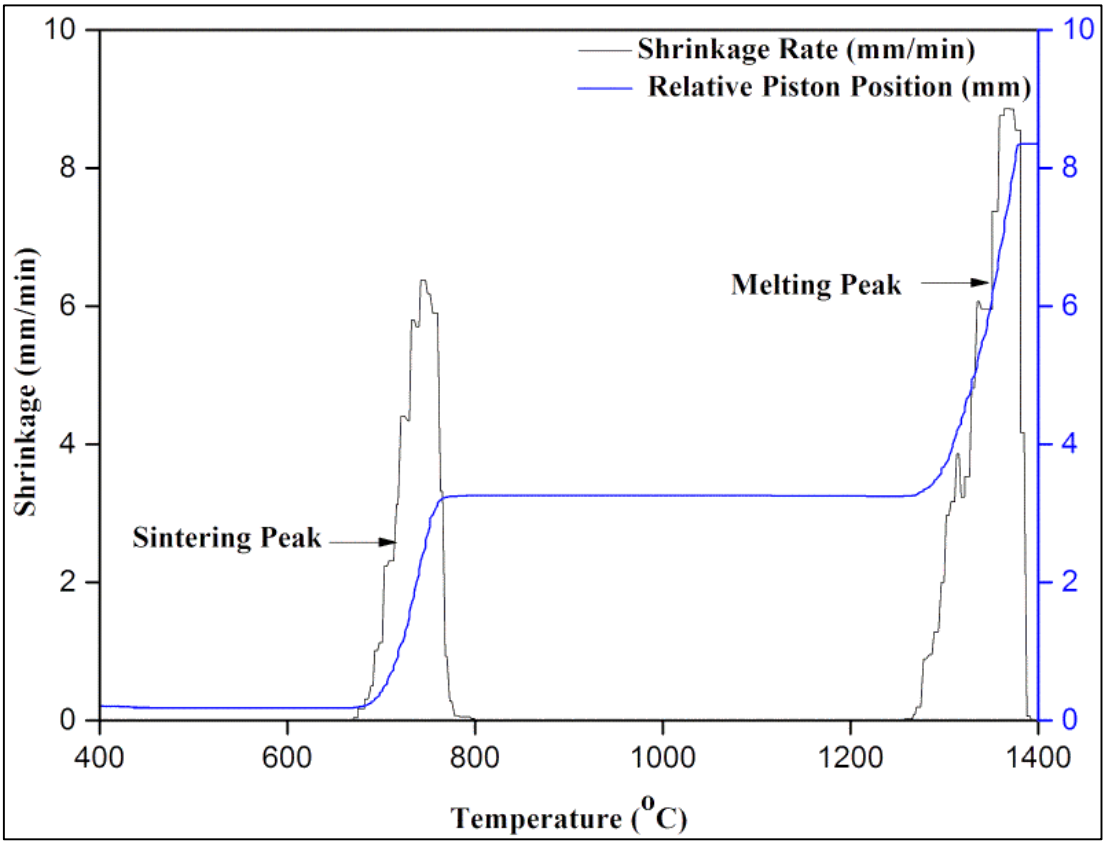

Figure 16: LG26 glass shrinkage in relation to applied force and temperature.

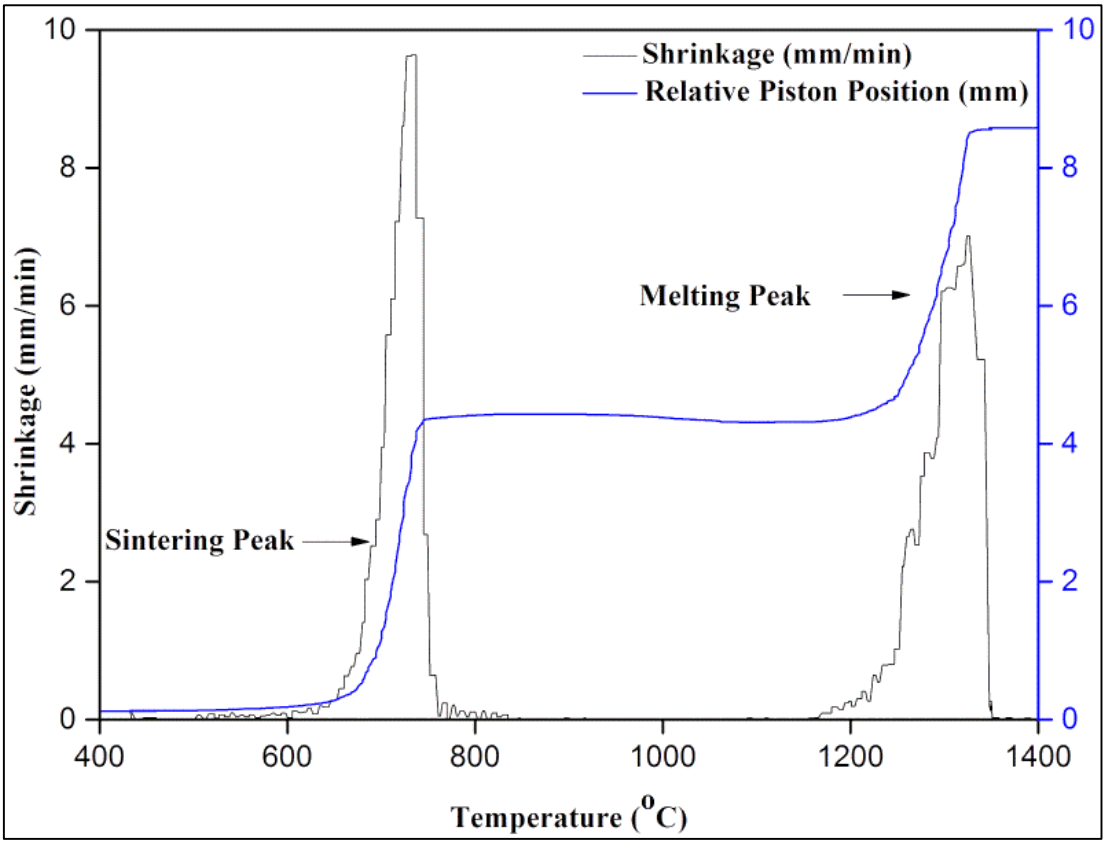

Figure 17: LG26Sr glass shrinkage in relation to applied force and temperature.

Two major peaks were identified. The first peak was associated with the speed of shrinkage or compaction of glass powder (particle packing temperature) and the elimination of voids (pores) formed during glass particles fusion. This peak coincided with the glass transition temperature that was measured by DSC and a heating rate of 10°C/min however this was purely due to coincidence as the two phenomena particle packing temperature and glass transition temperature) are not related. In order to find the glass transition temperature at fast heating rates (e.g. for sintering with FAST), thermal analysis at high heating rates should be carried out. The second peak was related to the melting of the glass powder. As the glass melts the pressure within the die increased resulting in the fracture of the graphite die. During conventional heat treatments, dissolution of crystal phases was reported by Hill et al. at 1200°C [152]. The second peak therefore can be related to the dissolution of crystal phases resulting in the formation of a highly viscous melt which is shown in the shrinkage curves in Figures 16

and 17 by a sudden drop in the peak. Table 9 shows the melting peak at 1250^{o}C in the case of LG26 and at 1150^{o}C in the case of LG26Sr. In the case of LG26Mg, the final sintering temperature was 1000^{o}C in order to avoid fracture of the graphite die and because of this the melting peak was not recorded. Based on these results from FAST, further heat treatment of the glasses was performed. The heat treatments performed on the glasses are given in Table 10.

The heat treatments helped to develop an understanding of the changes taken place in the crystallisation of glasses during shrinkage and after shrinkage. Sintering with different holding times and sintering with different heating rates were also carried out. In the case of LG26Mg, the heat treatment was performed up to 1000^{o}C only to avoid breaking of the die. Only the shrinkage rate and the piston movement were recorded. The results of the LG26Mg are shown in Figure 18. Table 11 shows the glass transition and crystallisation temperature reported by Wang for all the glass compositions [46].

Table 9: Sintering and melting temperature of LG26, Lg26Sr and Lg26Mg

Sample	**Rate of Shrinkage**			**Maximum shrinkage Rate (mm)**	**Piston Position at final sintering temperature (mm)**
	Starting Temperature (^{o}C)	**Peak Temperature (^{o}C)**	**End Temperature (^{o}C)**		
Sintering Peak					
LG26-1000-100-1	650	738	760	6.80	2.85
LG26Sr-1000-100-1	620	722	750	6.58	2.75
LG26Mg-1000-100-1	660	736	770	6.37	3.29
Melting Peak					
LG26-1400-100-1	1260	1369	1400	8.80	8.34
LG26Sr-1400-100-1	1169	1324	1400	6.97	8.59

Table 10: FCT Sintering Program of LG26, LG26Sr and LG26Mg.

Sample Name (glass name-sintering temperature-heating rate –holding time)	Sintering temperature (ºC)	Heating rate (ºC)	Cooling rate (ºC)	Heating pressure (kN)	Holding time (min)	Cooling pressure (kN)
LG26-700-100-1 LG26Sr-700-100-1 LG26Mg-700-100-1	700	100	100	5	1	5
LG26-800-100-1 LG26Sr-800-100-1 LG26Mg-800-100-1	800	100	100	5	1	5
LG26-900-100-1 LG26Sr-900-100-1 LG26Mg-900-100-1	900	100	100	5	1	5
LG26-1000-100-1 LG26Sr-1000-100-1 LG26Mg-1000-100-1	1000	100	100	5	1	5
LG26-800-100-5 LG26Sr-800-100-5 LG26Mg-800-100-5	800	100	100	5	5	5
LG26-900-100-5 LG26Sr-900-100-5 LG26Mg-900-100-5	900	100	100	5	5	5
LG26-800-300-5 LG26Sr-800-300-5 LG26Mg-800-300-5	800	300	300	5	1	5
LG26-800-500-5 LG26Sr-800-500-5 LG26Mg-800-500-5	800	500	500	5	1	5

Table 11: DSC analysis of LG26, LG26Sr and LG26Mg glasses [46].

Glass	Glass Transition Temperature (Tg) (ºC)	First Crystallisation Temperature (Tp1) (ºC)	Second Crystallisation Temperature (Tp2) (ºC)
LG26	667	793	1008
LG26Sr	659	894	N
LG26Mg	658	946	998

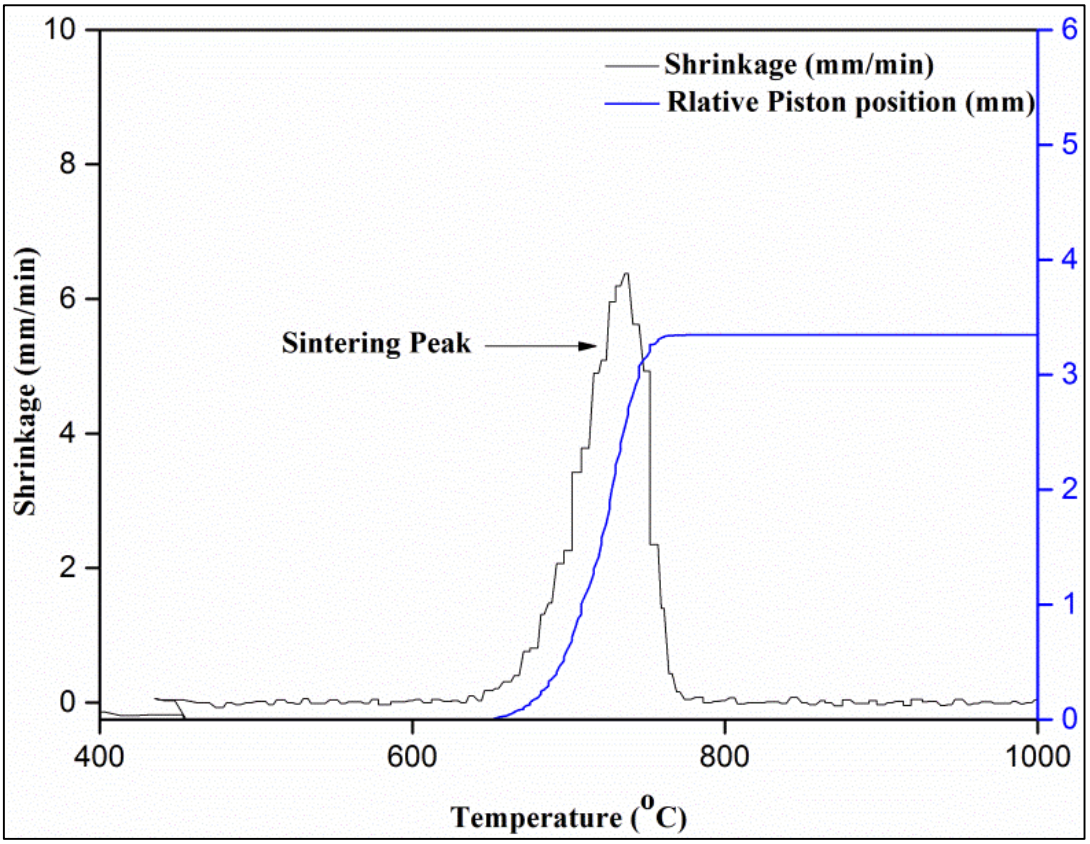

Figure 18: Shrinkage of LG26Mg during the FAST sintering process.

Figure 19 shows the rate of shrinkage and the piston position during the sintering of the LG26 at four different final sintering temperatures. In LG26-700-100-1 the compaction of the glass started at 650°C with maximum rate of shrinkage 2.83 mm at 700°C. The rate of compaction carried out in this glass is 0.43 mm based on the piston position from the starting to final temperature of 700°C. In LG26-800-100-1 the compaction started at 650°C and lasted up to 760°C. The maximum rate of shrinkage was at 725°C at the rate of 6.87 mm/min. In this sample (LG26-800-100-1) complete compaction of the glass was achieved and the glass was compacted to 3.08 mm at the final sintering temperature of 800°C.

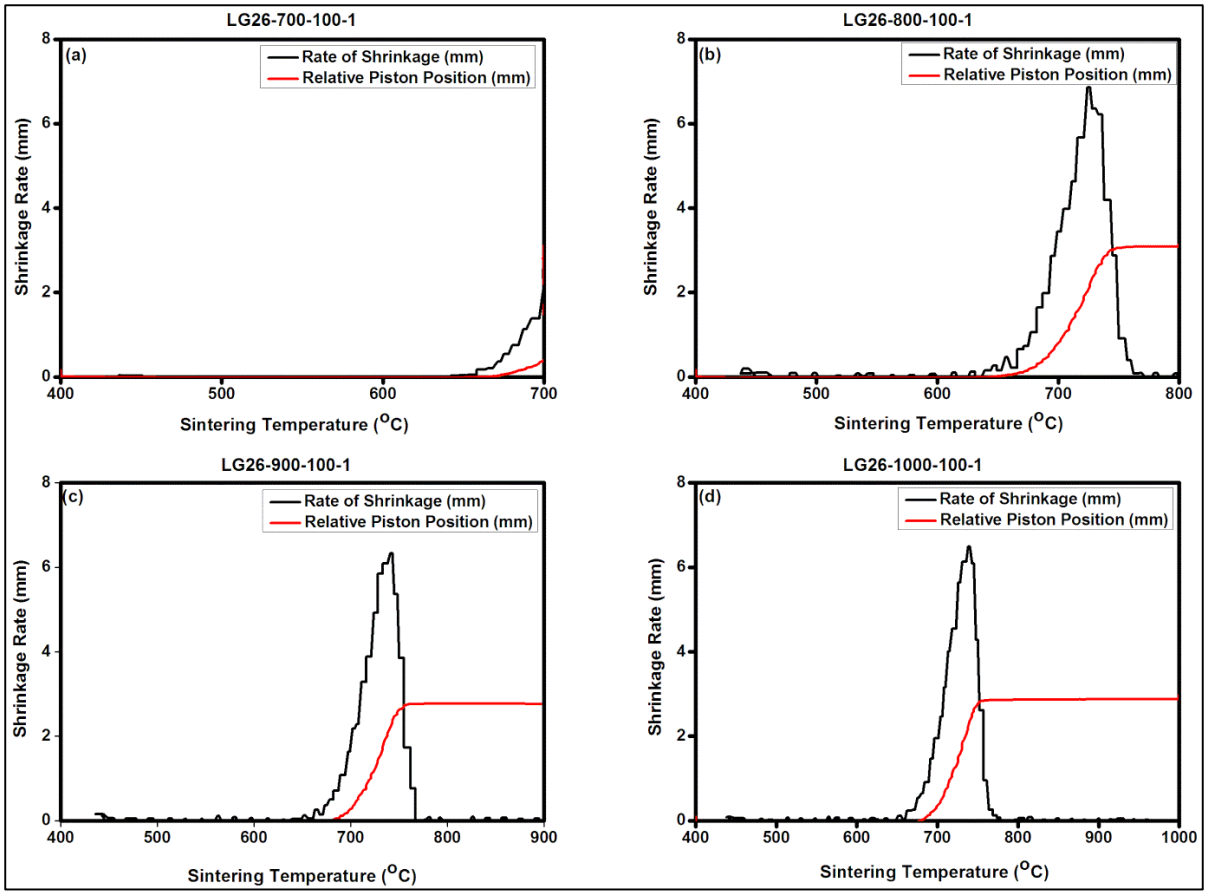

Figure 19: LG26 shrinkage and compaction rate of (a) LG26-700-100-1, (b) LG26-800-100-1, (c) LG26-900-100-1 and (d) Lg26-1000-100-1

LG26-900-100-1 shows similar compaction like LG26-800-100-1 with the maximum rate of 6.82 mm at 742°C. The glass was compacted to 2.76 mm at final sintering temperature of 900°C. LG26-1000-100-1 shows the similar compaction like the previous sintered samples. The maximum shrinkage rate was achieved at the temperature of 738°C with rate of 6.80 mm in this sample. The rate of compaction in this glass from the starting to the final temperature of 1000°C was 2.85 mm. Table 12 shows the detail rate of shrinkage and the compaction temperature of the glass crystallised at four different final sintering temperatures.

Table 12: Shrinkage and compaction rate of LG26

Sample Name (glass name-sintering temperature-heating rate – holding time)	Rate of shrinkage			Maximum shrinkage Rate (mm)	Piston Position at final sintering temperature (mm)
	Starting Temperature (°C)	Peak Temperature (°C)	End Temperature (°C)		
LG26-700-100-1	650	700	700	2.83	0.43
LG26-800-100-1	650	735	760	6.87	3.08
LG26-900-100-1	650	738	760	6.82	2.87
LG26-1000-100-1	650	738	760	6.80	2.85

Figure 20 (a) shows the rate of shrinkage and the compaction of LG26 glass based on the piston movement. LG26-800-100-5 shows the compaction of 2.8 mm from the room temperature to the final sintering temperature with holding time of 5 min. There is no change in the shrinkage starting temperature and the final end temperature when compared with the previous sintered sample of 1 min sintering time. The shrinkage starting temperature is 650°C and final end temperature is 760°C. The maximum shrinkage rate was 6.44 mm when this glass was at 729°C.

Figure 20 (b) shows the rate of shrinkage and the compaction of the glass LG26-900-100-5. The glass shows a similar shrinkage start and end temperature with LG26-800-100-5. The rate of shrinkage of 7.2 mm at 739°C was observed. The compaction that was achieved was 2.8 mm. Table 13 shows the rate shrinkage and piston position at the final sintering temperature for both of the above glass samples.

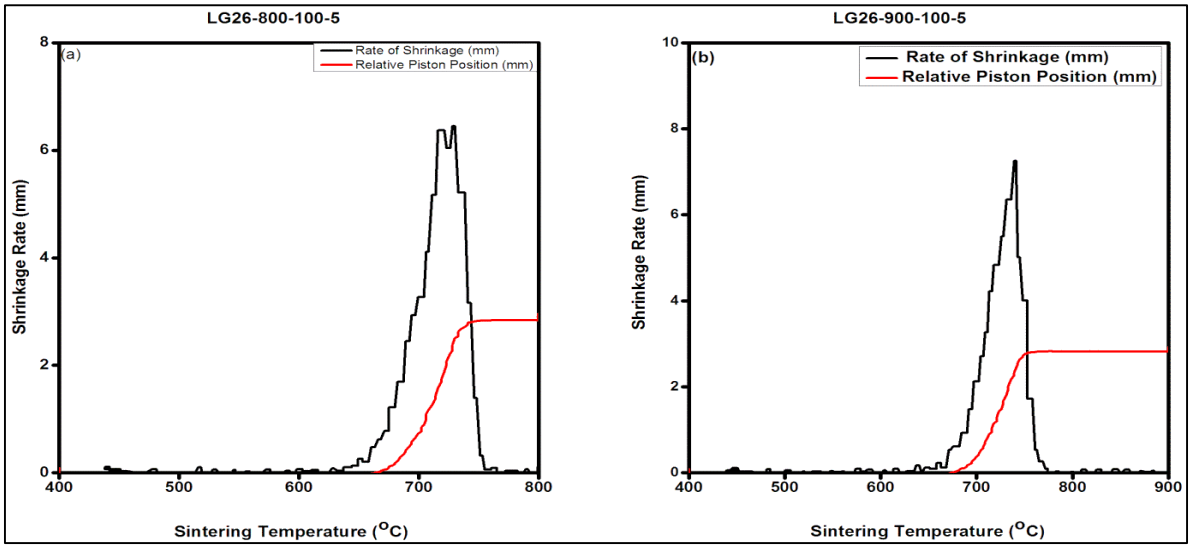

Figure 20: The rate of shrinkage and the compaction of LG26 glass based on the piston movement (a) LG26-800-100-5 and (b) LG-900-100-5

Figure 21 shows the shrinkage and compaction of LG26 at the heating rate of 300°C and 500°C/min. In both these experiments, the final sintering temperature was kept constant at 800°C while the applied force was 5kN. Figure 21(a) shows the shrinkage of LG26-800-300-5. In this sample, the recorded shrinkage temperature was 690°C and 800°C and the rate of shrinkage was 10.5 mm at 779°C.

The shrinkage in this glass was taken place at much higher temperature compared to all previous sintered samples of LG26. This is due to increased heating rate applied in this glass. The final compaction 3.06 mm was achieved which is higher than all previous results for the LG26 glass.

Figure 21(b) shows the shrinkage rate and the compaction of LG26-800-500-5. This sample shows lower shrinkage rate of 8.3mm/min and shrinkage started from the temperature of 750°C and ended at 800°C and compaction of 3.09 mm was achieved at final sintering temperature. The reasons for the very narrow peak for this sample is due to the final sintering temperature 800°C, were the compaction was stopped in the middle because of final sintering temperature.

It is to be mentioned that the pyrometer temperature reading are based on the surface of the graphite die not on the sample temperature. During FAST sintering process few researchers noticed the temperature difference during sintering.

Table 13: Shrinkage rate and piston position of LG26 sintering with 5 min holding time

Sample Name (glass name-sintering temperature-heating rate – holding time)	Shrinkage Starting Temperature (°C)	Shrinkage Peak Temperature (°C)	Shrinkage End Temperature (°C)	Maximum shrinkage Rate (mm)	Piston Position at final sintering temperature (mm)
LG26-800-100-5	650	729	760	6.4	2.8
LG26-900-100-5	650	739	760	7.2	2.8

Table 14: The difference in the shrinkage rate and piston position

Sample Name (glass name-sintering temperature-heating rate – holding time)	Shrinkage Starting Temperature (°C)	Shrinkage Peak Temperature (°C)	Shrinkage End Temperature (°C)	Maximum shrinkage Rate (mm)	Piston Position at final sintering temperature (mm)
LG26-800-300-5	690	779	800	10.5	3.06
LG26-800-500-5	750	790	800	7.65	3.09

This temperature difference is due to the conductivity of the sintered sample. If the sample is conductive then the pyrometer temperature is accurate due to the flow of current through the sample. In the case of non-conductive samples, the pyrometer temperature is not accurate for the sample temperature because the heating of the sample is carried out from the surrounding die wall to the centre of the sample. This can result in significant differences between the surface temperature and the sample bulk temperature.

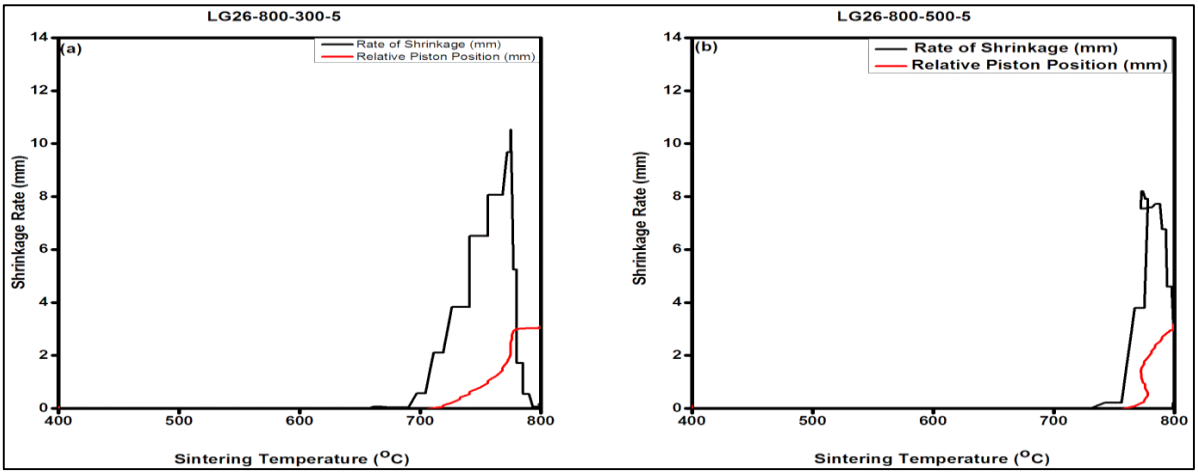

Figure 21: The shrinkage and compaction of LG26 at the heating rate of 300ºC and 500ºC/min (a) LG26-800-300-5 and (b) LG26-800-500-5.

Table 15: Shrinkage and compaction rate of LG26Sr

Sample Name (glass name-sintering temperature-heating rate – holding time)	Shrinkage Starting Temperature (ºC)	Shrinkage Peak Temperature (ºC)	Shrinkage End Temperature (ºC)	Maximum shrinkage Rate (mm)	Piston Position at final sintering temperature (mm)
LG26Sr-700-100-1	620	700	700	5.37	1.62
LG26Sr-800-100-1	620	726	750	5.95	2.50
LG26Sr-900-100-1	620	725	750	6.32	2.50
LG26Sr-1000-100-1	620	722	750	6.58	2.75

Figure 22 shows the rate of shrinkage of the glass and the piston position during the FAST sintering of the LG26Sr at four different final sintering temperatures. In LG26Sr-700-100-1 shows the compaction of this glass was taken place in between the sintering temperature of 620ºC and 700ºC with the maximum shrinkage rate of 5.37 mm at 700ºC. The rate of compaction based on the piston position from the starting to the final temperature of 700ºC was 1.62 mm.

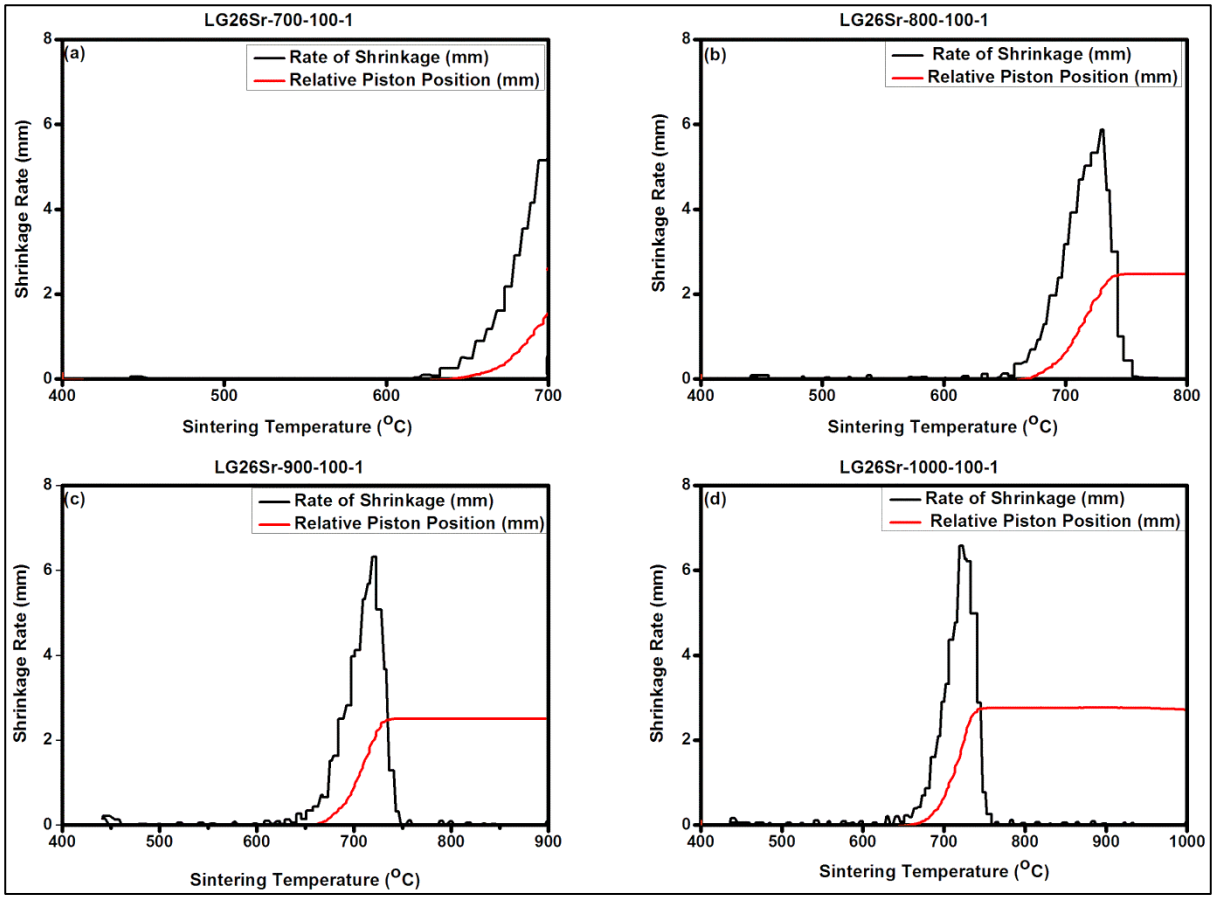

Figure 22:LG26Sr shrinkage and compaction rate of (a) LG26Sr-700-100-1, (b) LG26Sr-800-100-1, (c) LG26Sr-900-100-1 and (d) LG26Sr-1000-100-1

The LG26Sr-800-100-1 exhibits a compaction temperature of 620°C and 750°C. The maximum rate of shrinkage was at 726°C with the rate of 5.95 mm/min. The complete compaction of the glass was achieved and the glass was compacted to 2.50 mm from the position of the piston at the final sintering temperature of 800°C. In the case of LG26Sr-900-100-1, the shrinkage of the glass started from 620°C and 750°C similar to LG26Sr-800-100-1 with maximum rate of 6.32 mm at 725°C. The glass was compacted to 2.50 mm from the starting to final sintering temperature of 900°C. LG26Sr-1000-100-1 shows a similar shrinkage to the previous glasses sintered at 800°C and 900°C. The maximum shrinkage rate was achieved at the temperature of 722°C with rate of 6.58 mm. The rate of compaction in this glass from the starting to the final

temperature of 1000°C was 2.75 mm. Table 15 shows the shrinkage temperature and the compaction temperature of the glass crystallised at four different final sintering temperatures.

Figure 23 (a) shows the rate of shrinkage and the compaction of LG26Sr glass based on the piston movement. LG26Sr-800-100-5 shows the compaction of 3.26 mm at the final sintering temperature with holding time of 5 min. There is no change in the compaction starting temperature and the final end temperature shown in Table 15 when compared with Table 16 The shrinkage starting temperature is 620°C and final end temperature is 750°C. The maximum shrinkage rate was 6.64 mm when this glass was at 717°C.

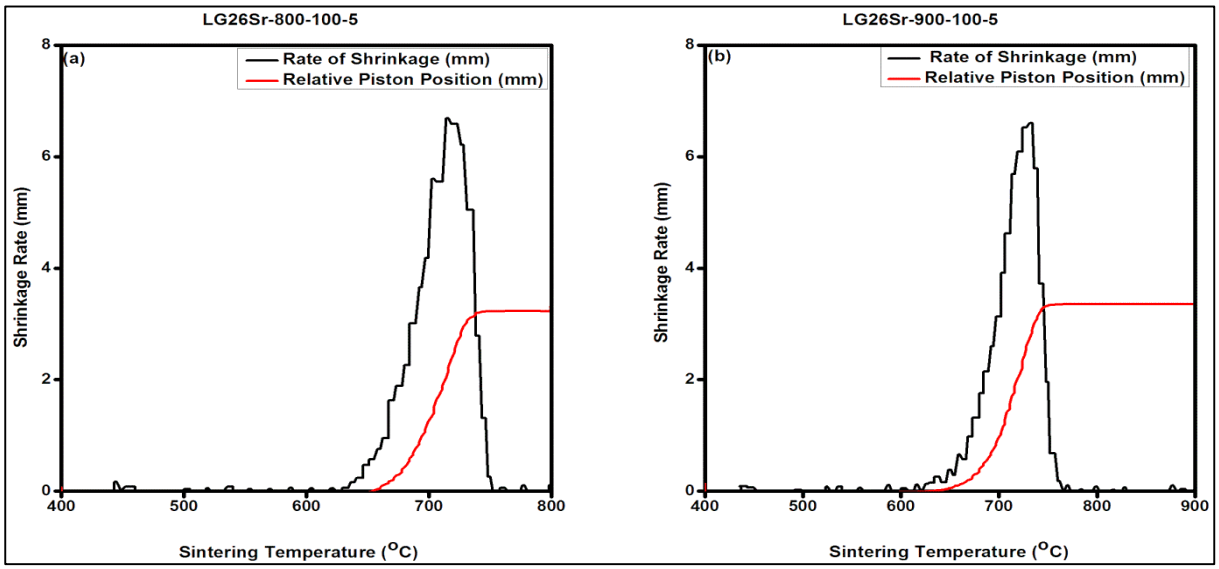

Figure 23: The shrinkage and compaction of LG26Sr at the heating rate of 300°C and 500°C/min (a) LG26Sr-800-100-5 and (b) LG26Sr-800-100-5

Figure 23 (b) shows the rate of shrinkage and the compaction of the glass LG26-900-100-5. The glass also shows the similar compaction temperature like LG26-800-100-5 with the rate of shrinkage of 6.58 mm at 720°C. The compaction of 3.29 mm was achieved.

Table 16: Difference in the shrinkage rate and piston position during FAST sintering of LG26Sr with 5 mins of holding time and at two different final sintering temperatures

Sample Name (glass name-sintering temperature-heating rate – holding time)	Shrinkage Starting Temperature (ºC)	Shrinkage Peak Temperature (ºC)	Shrinkage End Temperature (ºC)	Maximum shrinkage Rate (mm)	Piston Position at final sintering temperature (mm)
LG26Sr-800-100-5	620	717	750	6.64	3.26
LG26Sr-900-100-5	620	720	750	6.58	3.29

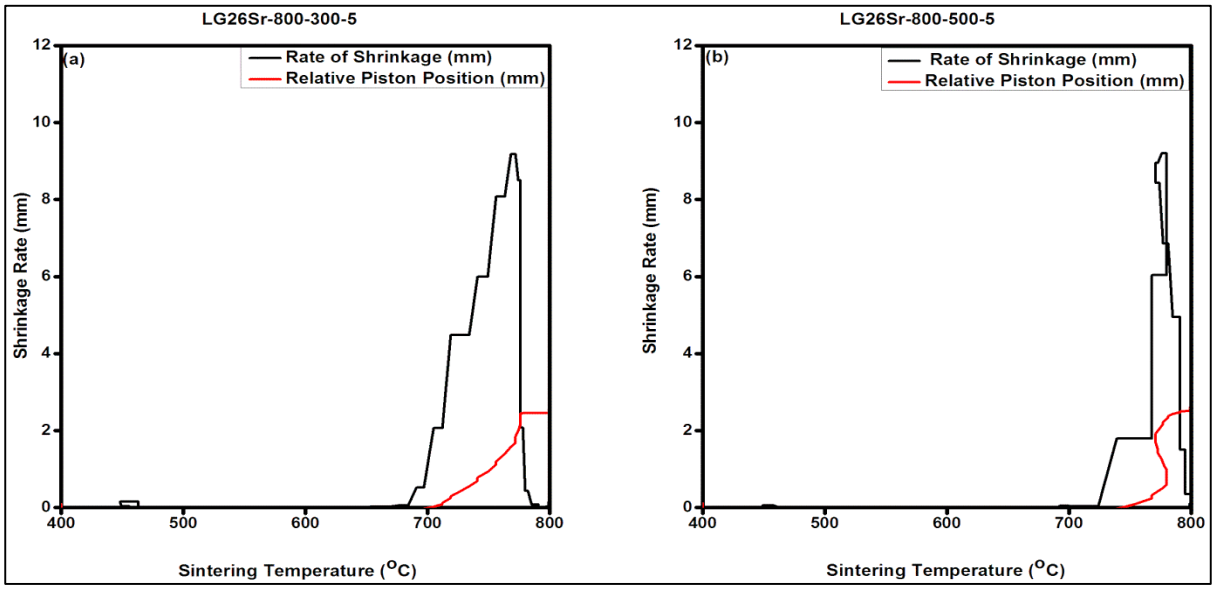

Figure 24: The shrinkage and compaction of LG26Sr at the heating rate of 300ºC and 500ºC/min (a) LG26Sr-800-300-5 and (b) LG26Sr-800-500-5

Figure 24 and Table 17 show the shrinkage and compaction of LG26Sr at the heating rates of 300ºC and 500ºC/min. In both experiments the final sintering temperature was kept constant at 800ºC and the applied force was 5kN. Figure 24 (a) shows the compaction of LG26Sr-800-300-5. In this sample a broad compaction peak was recorded between 680ºC and 771ºC at a rate of shrinkage is 9.71 mm/s. The shrinkage in this glass was taken place at higher temperature due to increased heating rate and final compaction 2.46 mm was achieved. Figure 24 (b) shows the shrinkage and the compaction of Lg26Sr-800-500-5. This sample shows lower shrinkage rate 9.17 mm/min when compared with LG26Sr-800-300-5 and compaction started

in between the temperature of 725ºC and 800ºC and compaction of 2.53 mm was achieved at final sintering temperature.

Table 17: Difference in the shrinkage rate and piston position of LG26Sr at different heating rate

Sample Name (glass name-sintering temperature-heating rate – holding time)	Shrinkage Starting Temperature (ºC)	Shrinkage Peak Temperature (ºC)	Shrinkage End Temperature (ºC)	Maximum shrinkage Rate (mm)	Piston Position at final sintering temperature (mm)
LG26Sr-800-300-5	680	771	790	9.71	2.46
LG26Sr-800-500-5	725	780	800	9.17	2.53

Figure 25 shows the rate of shrinkage of the glass and the piston position during the FAST sintering of LG26Mg at four different final sintering temperatures. In LG26Mg-700-100-1 shows the compaction of the glass was taken place at sintering temperature of 660ºC with the maximum rate of shrinkage of 1.97 mm at 700ºC. The glass was compacted to 0.54 mm at final sintering temperature. LG26Mg-800-100-1 shows the compaction temperature of 660ºC and 770ºC. The maximum rate of shrinkage of glass was at 739ºC at the rate of 6.85 mm/min. In this LG26Mg-800-100-1 the complete compaction of the glass was achieved and the glass was compacted to 3.30 mm from at final sintering temperature of 800ºC.

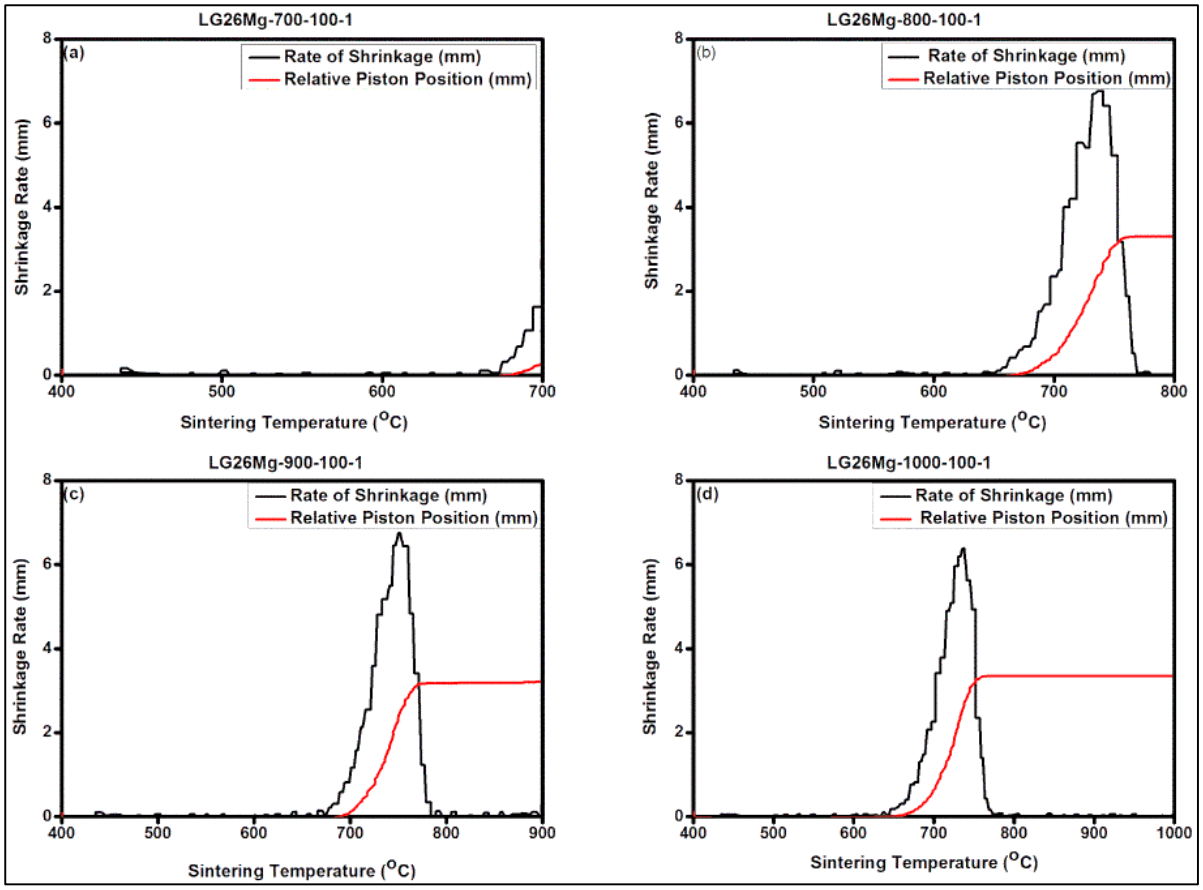

Figure 25: LG26Mg shrinkage and compaction rate of (a) LG26Mg-700-100-1, (b) LG26Mg-800-100-1, (c) LG26Mg-900-100-1 and (d) LG26Mg-1000-100-1

The LG26Mg-900-100-1 shows a compaction temperature similar to LG26Mg-800-100-1 with shrinkage rate of 6.75 mm at 751°C. The glass was compacted to 3.17 mm at the final sintering temperature of 900°C. LG26Mg-1000-100-1 shows a similar compaction temperature to LG26Mg-800-100-1 and LG26Mg-900-100-1. The maximum shrinkage rate achieved at the temperature of 736°C with rate of 6.37 mm. The rate of compaction in this glass was 3.29 mm. Table 18 shows the detail shrinkage temperature and the compaction temperature of the glass crystallised at four different final sintering temperatures.

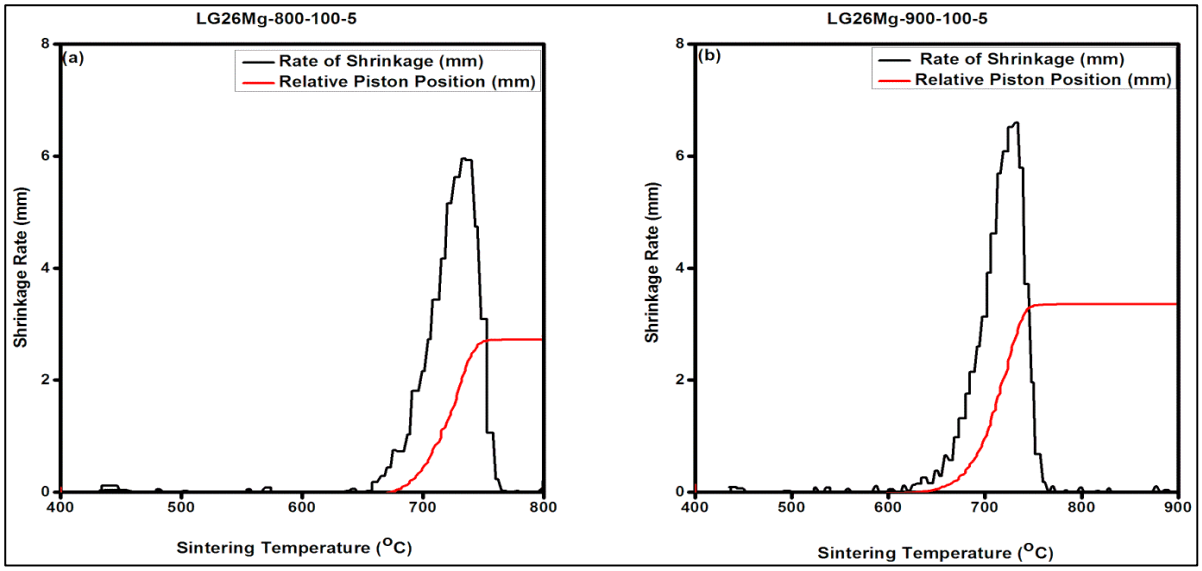

Figure 26: Shrinkage rate and piston position of LG26Mg (a) LG26Mg-800-100-5 and (b) LG26Mg-900-100-5

Figure 26 (a) shows the rate of shrinkage and the compaction of LG26Mg glass based on the piston movement. LG26Mg-800-100-5 shows the compaction of 2.68 mm starting from room temperature to the final sintering temperature with holding time of 5 min. There is no change in the shrinkage starting temperature and the final end temperature when compared with the previous sintered samples of 1 min holding time. The shrinkage starting temperature is 660^{o}C and final end temperature is 770^{o}C. The maximum shrinkage rate was 5.95 mm when this glass was at 736^{o}C.

Figure 26 (b) shows the rate of shrinkage and the compaction of the glass LG26Mg-900-100-5. The glass also shows the similar shrinkage start and the end temperature like LG26Mg-800-100-5 but the rate of shrinkage and peak sintering temperature was increases to 733^{o}C with the rate of 6.61 mm. The compaction of 3.36 mm based on the piston movement from the starting temperature to final sintering temperature was achieved.

Table 18: shrinkage and compaction rate of LG26Mg

Sample Name (glass name-sintering temperature-heating rate –holding time)	Shrinkage Starting Temperature (ºC)	Shrinkage Peak Temperature (ºC)	Shrinkage End Temperature (ºC)	Maximum shrinkage Rate (mm)	Piston Position at final sintering temperature (mm)
LG26Mg-700-100-1	660	700	700	1.97	0.54
LG26Mg-800-100-1	660	739	770	6.85	3.30
LG26Mg-900-100-1	660	751	770	6.75	3.17
LG26Mg-1000-100-1	660	736	770	6.37	3.29

Table 19: Difference in the shrinkage rate and piston position of LG26Mg

Sample Name (glass name-sintering temperature-heating rate – holding time)	Shrinkage Starting Temperature (ºC)	Shrinkage Peak Temperature (ºC)	Shrinkage End Temperature (ºC)	Maximum shrinkage Rate (mm)	Piston Position at final sintering temperature (mm)
LG26Mg-800-100-5	660	736	770	5.95	2.68
LG26Mg-900-100-5	660	733	770	6.61	3.36

Figure 27 shows the shrinkage and compaction of LG26Mg at the heating rate of 300ºC and 500ºC/min. In both this experiments the final sintering temperature was kept constant at 800ºC and applied force was 5kN. In Figure 27(a) of LG26Mg-800-300-5 shows shrinkage peak between the temperature of 700ºC and 800ºC and rate of shrinkage is increased to 9.68 mm at 769ºC. The shrinkage in this glass was taken place at much higher temperature due to increased heating rate and final compaction 3.25 mm was achieved

In Figure 27 (b) shows the shrinkage and the compaction of Lg26Mg-800-500-5. This sample shows shrinkage rate of 12.29 mm/min and shrinkage started from the temperature at 700ºC and ended at 800ºC and compaction of 3.15 mm was achieved at final sintering temperature. The reason from compaction at higher temperature is due to the heating rate of 500ºC the compaction was not completed because of final sintering temperature.

Table 20: The difference in the shrinkage rate and piston position of LG26Mg

Sample Name (glass name-sintering temperature-heating rate – holding time)	Shrinkage Starting Temperature (ºC)	Shrinkage Peak Temperature (ºC)	Shrinkage End Temperature (ºC)	Maximum shrinkage Rate (mm)	Piston Position at final sintering temperature (mm)
LG26Mg-800-300-5	700	769	800	9.68	3.25
LG26Mg-800-500-5	700	779	800	12.29	3.15

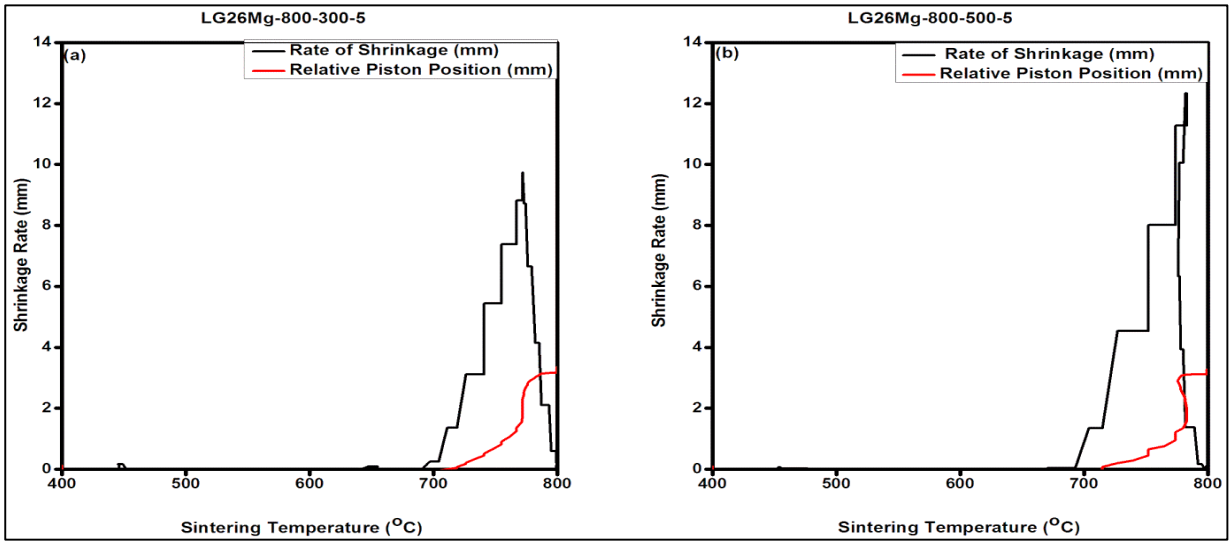

Figure 27: The shrinkage and compaction of LG26Mg at the heating rate of 300ºC and 500ºC/min (a) LG26Mg-800-300-5 and (b) LG26Mg-800-500-5

In summary, all glasses compact at the temperature of glass transition where the speed of shrinkage is high, which is possible due to softening point and the molecular moments at Tg. This case was clearly able to see on all the samples sintered using FAST. This can also be related to the elimination of pores and air trapped in pre compacted glass powder used in the graphite die for sintering in FAST. During this compaction region itself this glass starts to crystallise to its first crystal phases which can be clearly seen from the X-ray diffraction in section 5.1.3. The density and mechanical properties also shows the similar effect on the glass

crystallised which is related to formation of crystal phases the lowest value was achieved on the glass with no formation of crystal phases while increasing the temperature along with the formation of respective crystal phase the values tend to increase which can be seen in the section 5.21 and 5.14

3.1.2 Density

All the density measurement were carried on single sample produced at different temperature using FCT system. Due to this reason standard error bar was not included on this results

Figure 28a and table 21 shows the density of glass ceramics sintered using FAST technique at four different sintering temperatures. This table also compares with the relative piston position at the final sintering temperature.

The LG26Mg glass ceramics shows the lowest density value when compared with LG26 glass ceramics and Sr glass ceramics. This is due to the replacement of Ca with Mg cations. Magnesium has a smaller atomic weight (24.3) and ionic radius (0.086 nm) compared to calcium and strontium which resulting in a lower density of the glass and consequently the glass ceramic [76]. Previous reported work on this magnesium-substituted glass shows similar effects when increasing the molar concentration of Mg in the expense of Ca [76]. The reported oxygen density in these glass shows an increase in value when increasing Mg substitution which clearly shows the close packing of the network cations in the glass [76]. The size of cations plays a major role in density of all these glass ceramics. The expected density based on the conventional sintering of this Mg glass ceramics is 2.84 g/cm^3 but the obtained density is lower.

Table 21: Density of LG26,LG26Sr and LG26Mg

Sample Name (glass name-sintering temperature-heating rate –holding time)	Density (g/cm^3)	Piston position at final sintering temperature (mm)
LG26Mg-700-100-1	2.65	0.54
LG26Mg-800-100-1	2.66	3.30
LG26Mg-900-100-1	2.71	3.17
LG26Mg-1000-100-1	2.74	3.29
LG26-700-100-1	2.76	0.43
LG26-800-100-1	2.78	3.08
LG26-900-100-1	2.8	2.87
LG26-1000-100-1	2.86	2.85
LG26Sr-700-100-1	3.1	1.62
LG26Sr-800-100-1	3.12	2.50
LG26Sr-900-100-1	3.14	2.50
LG26Sr-1000-100-1	3.19	2.75

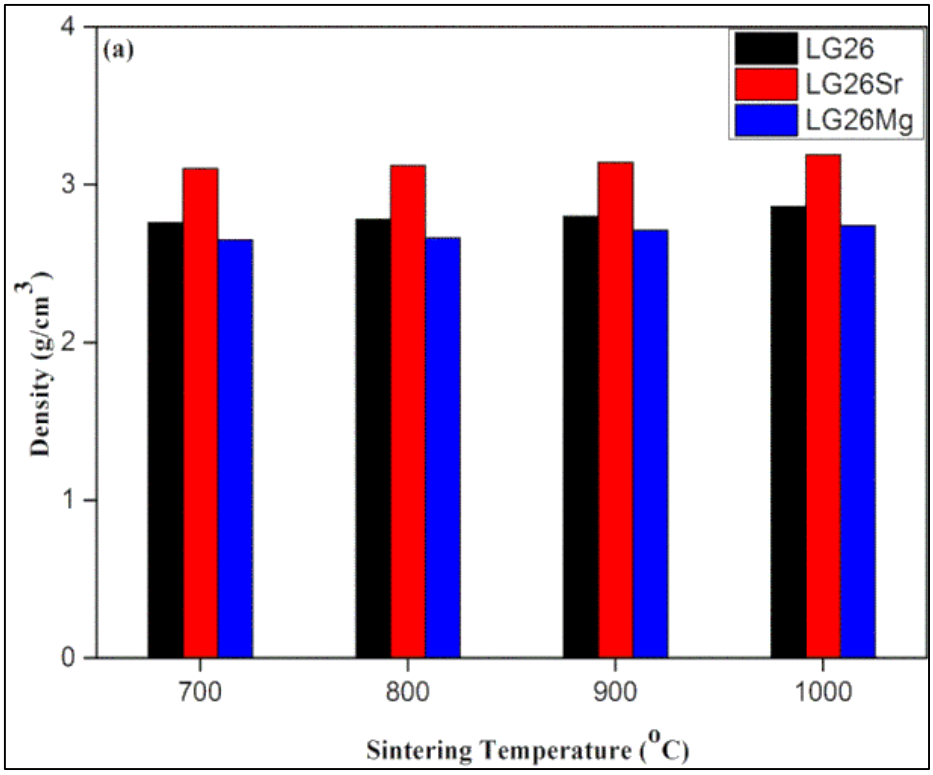

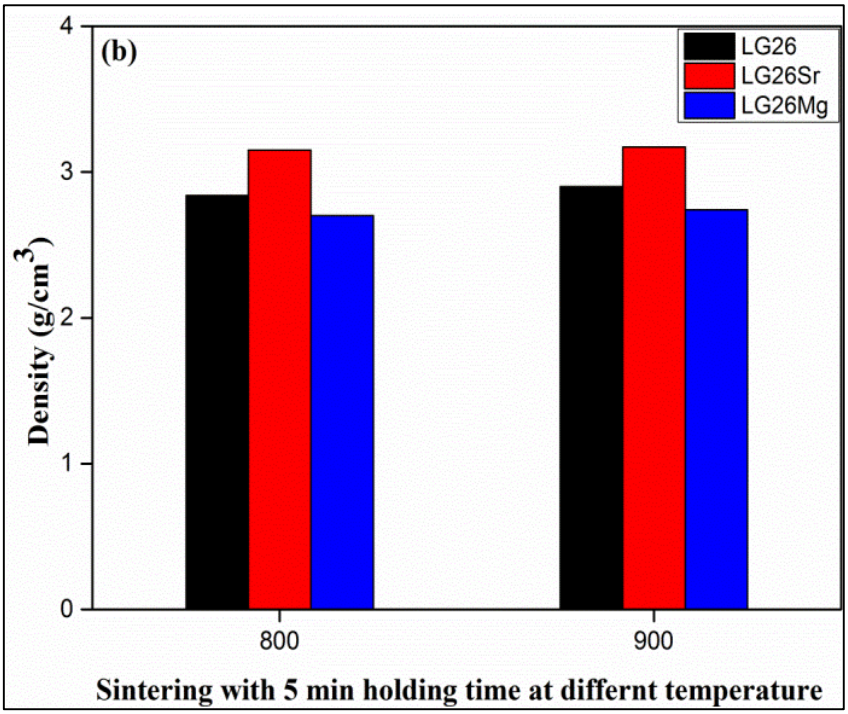

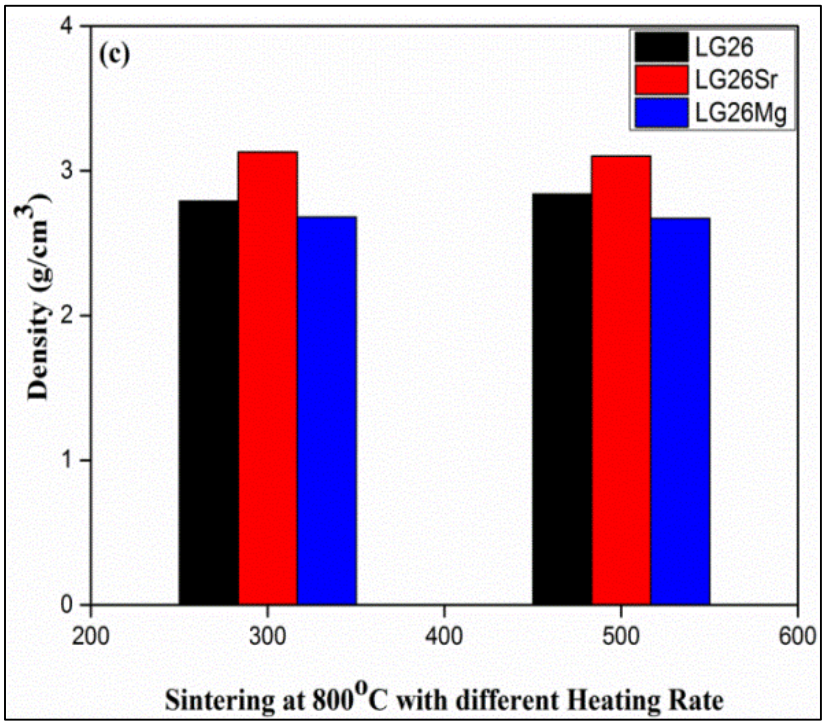

Figure 28: (a) Density of FAST sintered LG26, LG26Sr and LG26Mg sintered at different temperature, (b) Density of FAST sintering at different temperature with holding time of 5 min, (c)Density of LG26,LG26Sr and LG26Mg sintered at 800°C using different heating rate temperature

The reason for the low density is most likely due to the presence of amorphous glass in the sintered glass ceramic. A linear increase in density was observed, when the sintering temperature was increased. Table 21 shows the density of LG26Mg glass ceramics sintered at four different sintering temperatures using FAST.

In Figure 28a, LG26 shows a higher density value when compared with Mg glass ceramics. This is due to the presence of much larger cations of in the LG26 glass network. The Ca atom with an atomic weight of 40 and ionic radius of 0.1124 nm leads to the formation of larger amount of non-bridging oxygens and therefore a more expanded glass network was formed when compared to Mg glass network [46]. This in combination with the large calcium cation results in increased density for the LG26 when compared with LG26Mg [46]. The densities of LG26 glass ceramics also increased with increasing the sintering temperature from 700-1000^{o}C. This shows the influence of the sintering temperature in increasing the glass ceramics density.

The LG26Sr glass ceramics, which show the highest density, value when compared with Ca and Mg. This is due to the presence of larger cations of Sr which has the atomic weight of 87.6 and ionic radii of 0.132. The substitution of Sr for Ca results in increased density value due to the glass expansion of glass network because of the larger cation [46]. In the LG26Sr the change in density is not much when compared with LG26 and LG26Mg.

The value of density increased from 3.09 to 3.19 g/cm^3 when increasing the sintering temperature. The crystallographic analysis of these samples shows that this glass crystallised at much lower temperature when compared with the other glass ceramics.

Figure 28b and table 22 shows comparative density with the density of LG26Mg, LG26 and LG26Sr heat-treated at 800^{o}C and 900^{o}C. These glass ceramics were produced with a holding time of 5 min at the final sintering temperature. The density of the LG26Mg increased from

2.65 g/cm^3 to 2.7 g/cm^3 for the glass crystallised with 1 min to 5min and 2.7 to 2.74 g/cm^{3}of glass crystallised at 900^{o}C from 1 to 5 min sintering time. This density is much lower when compared with other two glasses. In the case of LG26 with longer holding time a similar increase in density was observed in both the temperature when compared with 1 min sintering time. LG26Sr shows the highest density when compared with the LG26 and LG26Mg. This Lg26Sr glass ceramics showed increase in the density value of 3.12 and 3.25 g/cm^3 at both the sintering temperature with longer holding time. This results shows that using FAST sintering technique this glass can be densified even at low temperature with longer sintering time.

Table 22: Density of LG26Mg with 5 min sintering time

Sample Name (glass name-sintering temperature-heating rate – holding time)	**Density (g/cm^3)**	**Final piston position (mm)**
LG26Mg-800-100-5	2.7	2.68
LG26Mg-900-100-5	2.74	3.36
LG26-800-100-5	2.84	2.8
LG26-900-100-5	2.90	2.8
LG26Sr-800-100-5	3.15	3.26
LG26Sr-900-100-5	3.17	3.29

Table 23: Density of LG26Mg with different heating rate

Glass Sample Name (glass name-sintering temperature-heating rate – holding time)	**Density (g/cm^3)**	**Final piston position (mm)**
LG26Mg-800-300-5	2.68	3.25
LG26Mg-800-500-5	2.67	3.15
LG26-800-300-5	2.84	3.06
LG26-800-500-5	2.79	3.09
LG26Sr-800-300-5	3.13	2.46
LG26Sr-800-500-5	3.10	2.53

Figure 28c and table 23 shows the changes in the density of the glass crystallised with change in heating rate. LG26 Mg shows the lowest density when compared reset of the glass ceramics. The value of the density decreased when the heating rate was increased.

The similar changes was also observed in LG26 and LG26Sr. this shows that with increase in the heating rate this glass require a longer sintering time to crystallise the X-ray diffraction of this glass also shows the presence of amorphous bump in the lower diffraction angle.

In general, the density of the glass to glass ceramics increased from LG26Mg(2.66 g/cm^3), LG26 (2.7g/cm^3) and LG26Sr (3.10g/cm^3) to 2.75 g/cm^3 ,2.95g/cm^3 and 3.25 g/cm^3 . In compression with density of conventional crystallisation the of LG26 (2.84g/cm^3) and LG26Sr (3.12 g/cm^3) the obtained values are higher but the LG26Mg(2.84 g/cm^3) was reduced which might be due to sintering temperature [46]. Increasing sintering time with longer holding time may help to improve the density of LG26Mg. the density of all the glass-ceramics will be extensively discussed in the further section

3.1.3 X-ray Diffraction

Table 24 shows the JCPDS reference number used to match crystal peaks on the LG26 sample sintered Using FAST. Table 25 and table 26 shows the JCPDS reference used for LG26Sr and LG26Mg glass ceramic. All the crystallography analysis were carried out using X-pert high score plus software.

Table 24: Crystallographic parameters from XRD database for LG26

S.no	Major crystal phases	JCPDS reference number	Crystal structure
1	Fluorapatite $Ca_5(PO_4)_3F$	00-003-0736	Hexagonal
2	Mullite $Al_6Si_2O_{13}$	00-006-0259	Orthorhombic

Table 25: Crystallographic parameters from XRD database for LG26Sr

S.no	Major crystal phases	JCPDS reference number	Crystal structure
1	Sr Fluroapatite $Sr_5(PO_4)_3F$	00-017-0609	Hexagonal
2	Sr aluminosilicate $SrAl_2Si_2O_8$	00-038-1454	Monoclinic

Table 26: Crystallographic parameters from XRD database for LG26Mg

S.no	Major crystal phases	PDF reference number	Crystal structure
1	Wagnerite $Mg_2(PO_4)F$	00-042-1330	Monoclinic
2	Mullite ($Al_6Si_2O_{13}$)	00-006-0259	Orthorhombic

The XRD patterns of LG26, LG26Sr and LG26Mg glasses and glass ceramics sintered at 700^{o}C for 1 min at 100^{o}C heating rate are shown in Figure 29. The XRD patterns of glasses show clearly the absence of crystallinity as expected. The glass ceramics formed after sintering at 700^{o}C however showed no signs of crystallinity with some more obvious amorphous peaks indicating that FAST process glass did not crystallise or the crystals formed were very small. In the first case, the glass network did not have the time to respond to the change of temperature as the heating rate was fast and therefore no phase change was possible to be observed.

In the second case, if there was formation of crystals, the crystals formed may have been very small or both the number and the size of crystals were small. The crystals would not have the time to grow as the heating rate was fast and there was not enough energy offered from the external environment to the glass network. As a result the XRD pattern would not change significantly and amorphous broad areas would continue to appear in the diffractogramm [1, 2].

Taking into consideration of previous work carried on this glass system, it was mentioned that the LG26 glass crystallises into two phases; fluorapatite ($Ca_5(PO_4)_3F$) at 793^{o}C (first crystallisation temperature) and mullite ($Al_6Si_2O_{13}$) at 1008^{o}C (second crystallisation temperature). The first crystallisation temperature is not far from the FAST sintering temperature of 700^{o}C and one would have expected to be able to observe some crystallisation in the glass network.

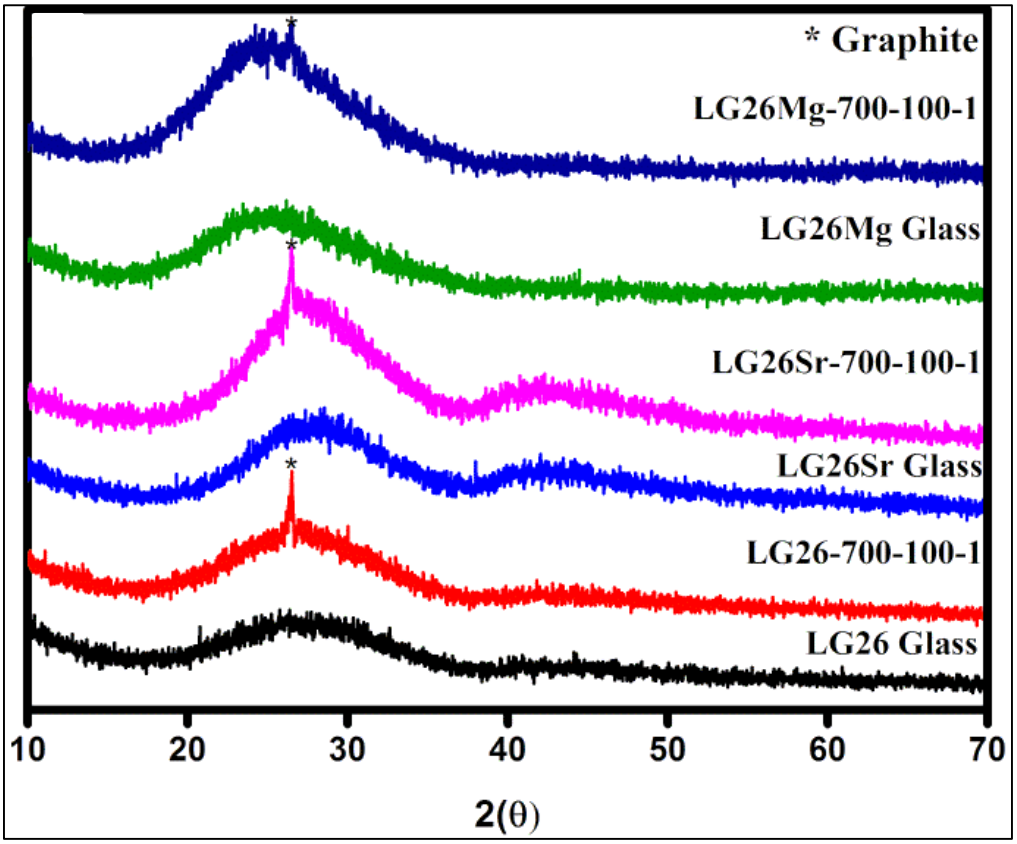

Figure 29: XRD patterns of LG26, LG26Sr and LG26Mg glass powder and glass ceramics

During the FAST sintering process, there are three parameters which play a major role in the sintering of any material:

1. High heating rate: the heating rate is high when compared with conventional sintering process. If the glass is conductive then the heat can pass through the glass powder [3].

2. The sintering time: sintering time is interlinked with the heating rate. If the sample is conductive, the 1 min sintering time is more than enough for crystallisation but if it is non-conductive then longer sintering time plays a major role in crystallisation due to the temperature difference between the die and the sample centre [5, 153].

3. The applied pressure: this helps to eliminate the pores between the inter particular region of powder materials and helps to form nano crystals [6].

A minor peak at 2 theta of LG26 at 25^{o} is associated with the presence of graphite. This is due to the graphite mould used for the sintering process. During the FAST process migration of

graphite from the surrounding foils to the sample occurs resulting in the appearance of the graphite peak in all XRDs. To eliminate the graphite from the sample, post heat treatment at 750^{o}C for 1 hour is required. This temperature is very close to the first crystallisation temperature and such a post-treatment would affect the crystallisation of the sample.

The XRD patterns of LG26, LG26Sr and LG26Mg glass sintered using FAST at 800^{o}C with 1min sintering time are shown in Figure 30. The sintered glasses show the presence of crystalline peaks from the reflections of X-Ray beam of the diffractogram with the exception of LG26Mg which shows to be amorphous. In all diffracotgrams graphite is present as has been already explained above. In the LG26 diffractogramm the identified crystal phases are fluorapatite ($Ca_5(PO_4)_3F$) with a minor formation of mullite ($Al_6Si_2O_{13}$) whereas LG26Sr exhibits the presence of Sr fluorapatite ($Sr_5(PO_4)_3F$) only.

In the case of LG26 the formation of fluorapatite can be seen at this sintering temperature of 800^{o}C. This sintering temperature is higher than the first crystallisation temperature of fluorapatite crystals (793^{o}C) measured by thermal analysis at a heating rate of 10^{o}C/min. Minor formation of mullite can also be observed at 800^{o}C indicating that the crystallisation of mullite is started but its limited due to the sintering temperature and the sintering time .

This mullite crystal peak also overlaps with the graphite peak which appears at same degree in 2Θ. During the conventional sintering process this glass is sintered in two steps; one with nucleation hold for 1 hr and final crystallisation at 1100^{o}C with holding time of 1hr to form a glass ceramic with crystal phases of fluorapatite and mullite. The conventional sintering was carried out at the heating rate of 10^{o}C/min. During the FAST sintering process, LG26 glass was sintered using a single step process.

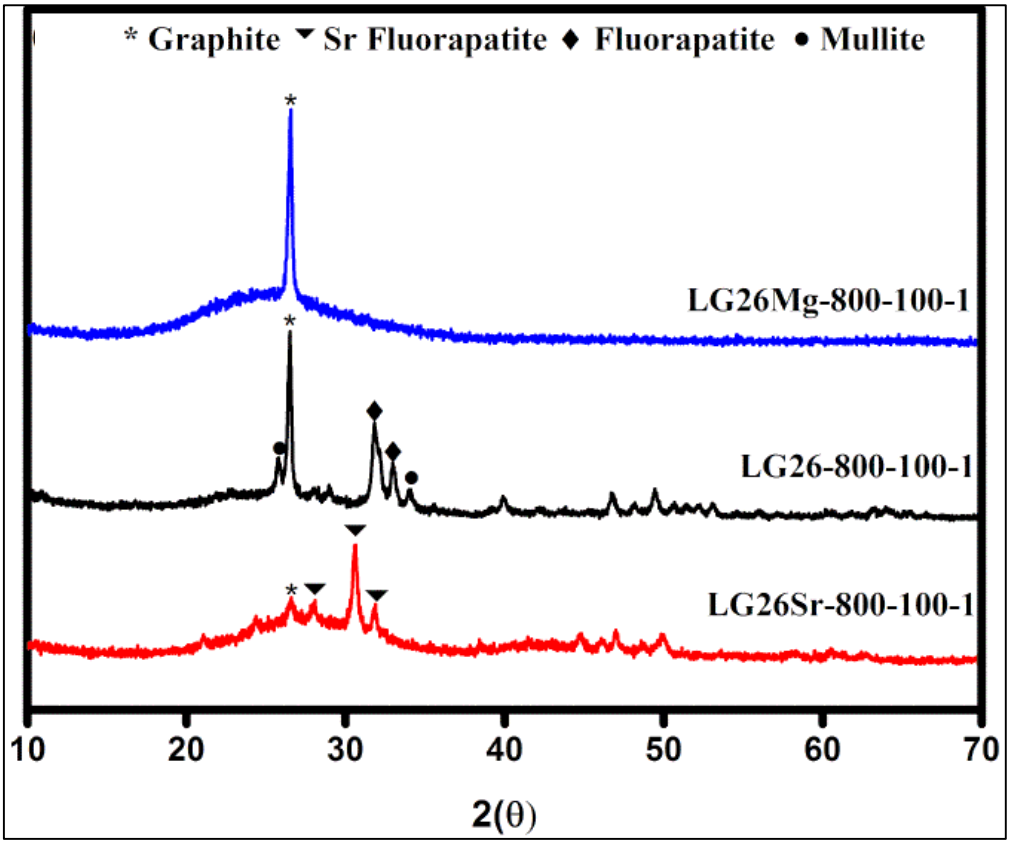

Figure 30: XRD patterns of LG26, LG26Sr and LG26Mg glass ceramics after FAST sintering at 800°C for 1 min

During this single step process, the formation of both crystal phases at 800°C with 1 min holding time was observed. The differences between the two processes are high heating rate, applied pressure and sintered for few minutes under vacuum environment in FAST, whereas in conventional sintering low heating, longer sintering time and no vacuum environment was used. It is worth mentioning that the peak intensity of fluorapatite and mullite were smaller and the peaks broader due to probably low degree of crystallisation and the presence of a significant amount of amorphous glass.

In the case of LG26Sr, the graphite peak intensity is much smaller when compared with LG26 which shows the presence of graphite is lower in this glass network once glass started to crystallise this can also be observed in the figure 33 were this LG26Sr glass crystallised with 5 min holding time at 800°C. The formation of Sr fluorapatite can also be seen at this

temperature. According to previous research only one crystallisation temperature at 894^{o}C was observed for this glass composition [46]. This reported crystallisation temperature is shared between its two crystal phase (Sr fluorapatite and Sr celsian). In this case of FAST sintered LG26Sr only the formation of Sr fluorapatite at 800^{o}C occurred. This temperature is below the previously reported crystallisation temperature indicating perhaps that Sr fluorapatite forms first with Sr celsian crystallising perhaps at a higher temperature or at longer sintering times. The absence of Sr celsian also indicates that most of the sintered materials remain amorphous.

LG26Mg shows no formation of crystal phases during sintering at 800^{o}C with 1 min holding time at 100^{o}C heating rate. This shows that this glass needs either higher temperature or longer sintering time to crystallise. During a convention sintering process, the first crystallisation took place at 946^{o}C and the second crystallisation took place at 998^{o}C higher to the sintering temperature during the FAST process. Looking at the crystallisation behaviour of all glasses it is worth mentioning, that both of the glasses that crystallised LG26 and LG26Sr, formed crystal phases at a temperature lower than their crystallisation temperatures with a low heating rate. Therefore it would be expected that LG26Mg would also crystallise at lower temperatures. In this case, 800^{o}C did not seem to be high enough for the crystallisation of the glass during the FAST process. It is obvious however that the high heating rate and the vacuum had a significant effect on the crystallisation temperatures of all the glass compositions.

Figure 31 shows the XRD of FAST sintered glass at 900^{o}C with 1 min sintering time at the heating rate of 100^{o}C/min. LG26 glass ceramics show the presence of both fluorapatite and mullite with formation of sharp peaks in Figure 31. No graphite was present at this sintering temperature for LG26 and LG26Sr but not for LG26Mg. The above results show that LG26 seems to crystallise during the FAST process at a temperature that lies in between the first and second crystallisation temperature of the glass as it was determined by a conventional low heating rate sintering process. The obtained density (2.8 g/cm^{3}) is nearly similar to the

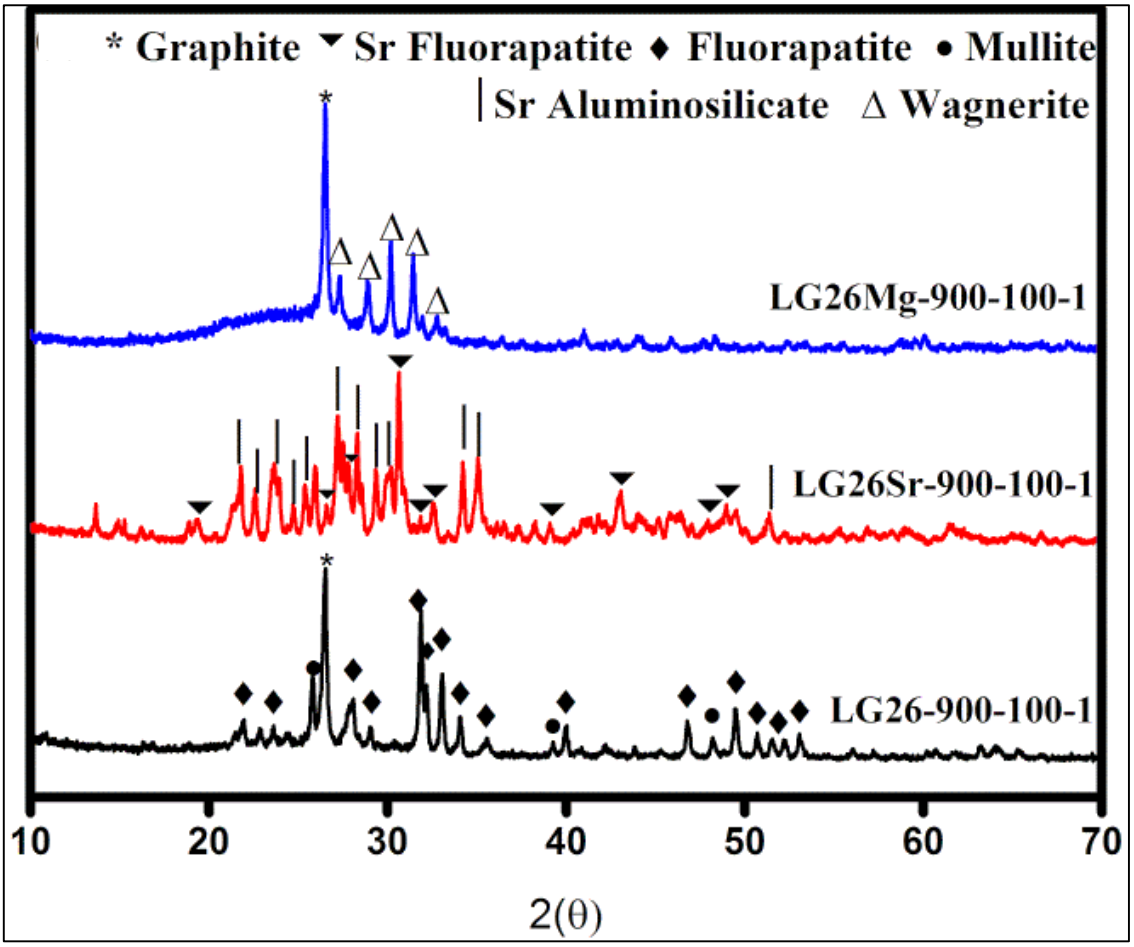

Figure 31: XRD patterns of LG26, LG26Sr and LG26Mg glass ceramics after FAST sintering at 900°C for 1 min

density measured after a conventional sintering process (2.84g/cm^3). LG26Sr also shows the complete crystallisation of both crystal phases (Sr-fluorapatite $Sr_5(PO_4)_3F$ and Sr-celsian $SrAl_2Si_2O_8$). In this case the presence of this two crystal phases at 900°C confirms that both crystal phases share single crystallisation temperature of 894°C only difference is the formation of Sr aluminium silicate second crystal phase which requires high temperature leaving Sr fluorapatite to form first from the glass network. LG26Mg shows the formation of Wagnerite Mg_2PO_4F and graphite. The absence of mullite shows that this glass requires a heat process higher than 900°C during FAST process in order to form Wagnerite and mullite as mentioned in an earlier work about conventional crystallisation of this glass composition. It is therefore clear that the Mg substituted glass composition does not behave in a similar way as the calcium

base glass and the strontium substituted glass composition. This might be due to the presence of Mg^{2+} cations which is smaller in size when compared to Sr^{2+} and Ca^{2+} cations. As mentioned above, previous thermal analysis showed that larger cations in these glass composition result in the reduction of the crystallisation temperature whereas smaller cations resulted in an increase of the crystallisation temperature [46]. These effects can maybe easily related to the presence of higher amounts of non-bridging oxygen in the case of strontium and calcium glass compositions compared to the magnesium substituted glass composition [46].

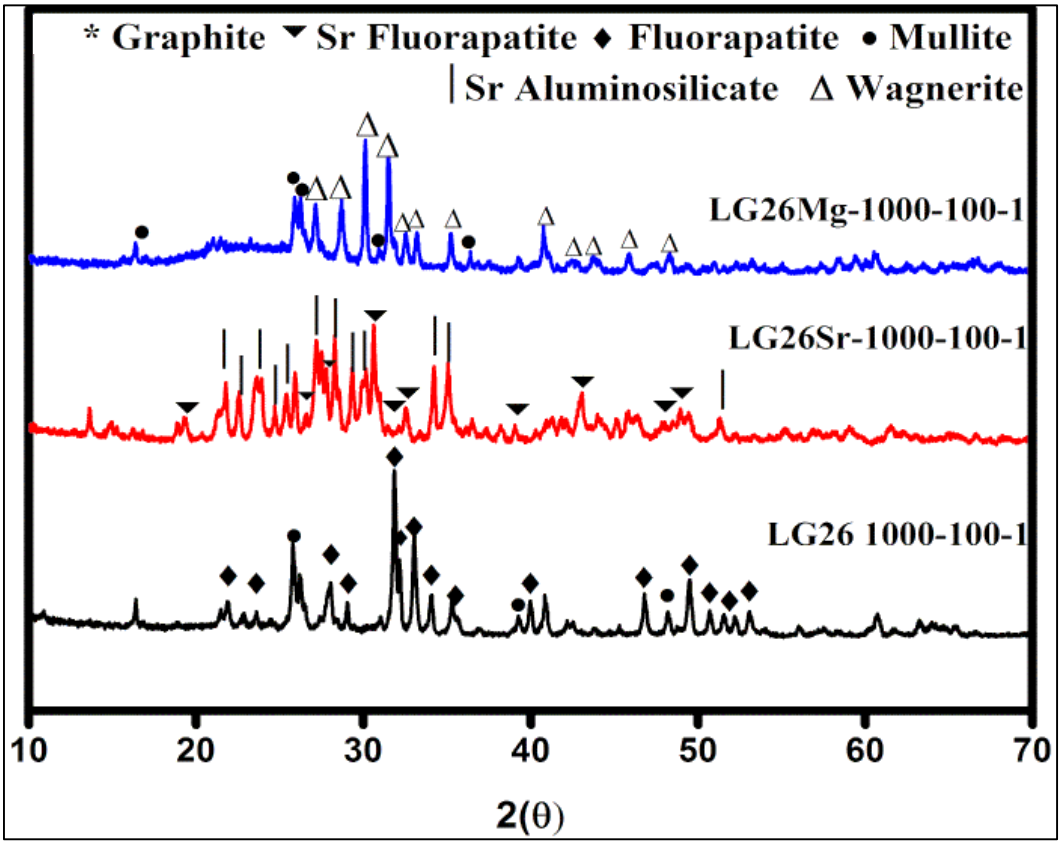

Figure 32: XRD diffractogramms of LG26, LG26Sr and LG26Mg glasses and glass ceramics: respectively after FAST sintering at 1000°C for 1 min

Figure 32 shows a comparison of FAST sintering at 1000°C for 1 min with 100°C/min heating rate of LG26, LG26Sr and LG26Mg glass ceramics. LG26 glass was crystallised to fluorapatite, and mullite at 1000°C. LG26Sr was also crystallised to a Sr-fluorapatite phase and

a Sr-celsia phase. The LG26Mg glass was crystallised in mullite and wagnerite but some amorphous glass was also observed. Graphite was not present in any of the diffractogramms. Mullite is a common phase that occurs in both LG26 and LG26Mg at the second crystallisation temperature. In all these three glasses very sharp and narrow crystal peaks can be noted. All the glasses sintered at 1000^{o}C showed crystallisation of their respective crystal phase.

Figure 33 shows the compression of XRD patterns between LG26, LG26Mg, and LG26Sr sintered at 800^{o}C for 5 min with 100^{o}C as heating rate. In the case of LG26 the fluorapatite and minor formation of mullite phase was noted similarly to the glass sintered at 800^{o}C with 1 min sintering time. When comparing the peak intensity of LG26, 5 min sintering time shows better crystal peaks than the 1 min sintering time. The longer the sintering time, the higher the degree of crystallisation. In this case, the formation of fluorapatite is much better than with longer sintering time. In LG26Sr complete crystallisation of both phases can be observed at this sintering temperature with 5 min holding time. The peak intensity of Sr fluorapatite is much higher when compared with the rest of the sintered LG26Sr glass which indicates that the formation of Sr-fluorapatite is more favourable at this temperature with holding time of 5 min. There is no graphite identified in the diffractogramm. LG26Mg shows only Wagnerite formation at 800^{o}C with longer sintering time. This is good indication when compared with figure 30 were no sign of crystal phase was observed at 1 min holding time. This shows that LG26Mg can be crystallised at lower temperature with single crystal phase when using longer sintering time. The presence of graphite is also minor when compared with the peak intensity of 1 min sintering time of all glass at 800^{o}C. This is due to decomposition of carbon at this temperature with longer sintering time. In all this glasses crystallisation can be achieved at low temperature once the sintering time is optimised.

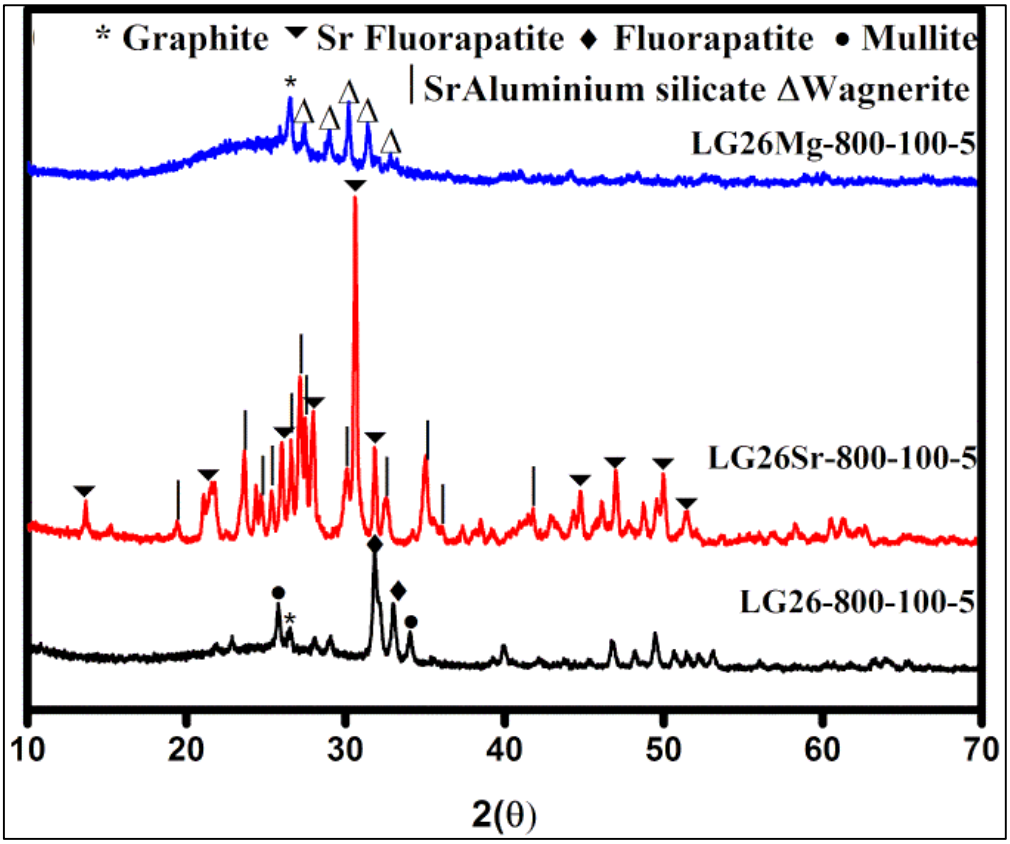

Figure 33: XRD diffractogramms of LG26, LG26Sr and LG26Mg glasses and glass ceramics: respectively after FAST sintering at 800°C for 5 min

Figure 34 shows the comparison of XRD patterns of LG26, LG26Sr and LG26Mg with sintering temperature of 900°C for 5 min with 100°C/min as heating rate. LG26 shows the presence of fluorapatite and mullite and absence of graphite and amorphous region at the lower 2 theta. In the case of LG26Sr the presence of Sr fluorapatite and Sr aluminosilicate (Sr celsian) can be noted. LG26Mg shows the presence of mullite and Wagnerite with absence of graphite peaks at 25°. All these glass ceramics show their respective crystal phase when increasing the sintering time. When comparing to the XRD of 900°C with 1 min holding time, the peaks are sharper and narrower which is a good indication that the glass was crystallised.

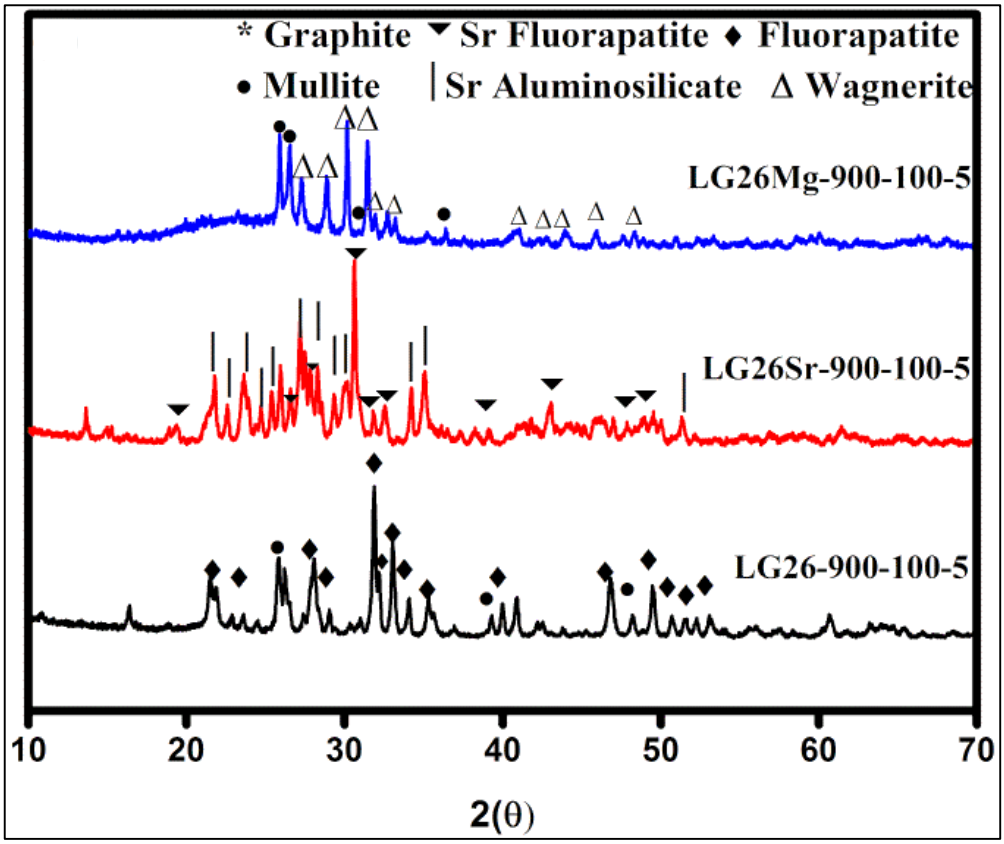

Figure 34: XRD diffractogramms of LG26, LG26Sr and LG26Mg glasses and glass ceramics: respectively after FAST sintering at 900°C for 5 min

This result also show that by using the FAST method, these glasses can be crystallised at low temperature with 5 min of sintering time. Whereas during conventional sintering methods, the crystallisation of the glass can only be achieved at 1100°C in order to form their respective crystal phases.

Figure 35 shows the difference in the XRD patterns of LG26, LG26Sr and LG26Mg sintered using FAST with heating rates of 300°C/min. The major crystal phases identified in this crystallised glass LG26 are fluorapatite, and mullite. The increase in heating rate from 100 to 300°C shows very little effects in the glass ceramics.

The presence of amorphous region can be noted in LG26. Increasing the heating rate along with 5 min sintering time has similar effects to the glass as if the glass was sintered with 100°C

heating rate for 5 min. In the case of LG26Sr, the complete crystallisation of Sr aluminium silicate (Sr celsian), Sr fluorapatite with the absence of graphite which shows that this change in heating rate has no effect in this LG26Sr glass crystallisation.

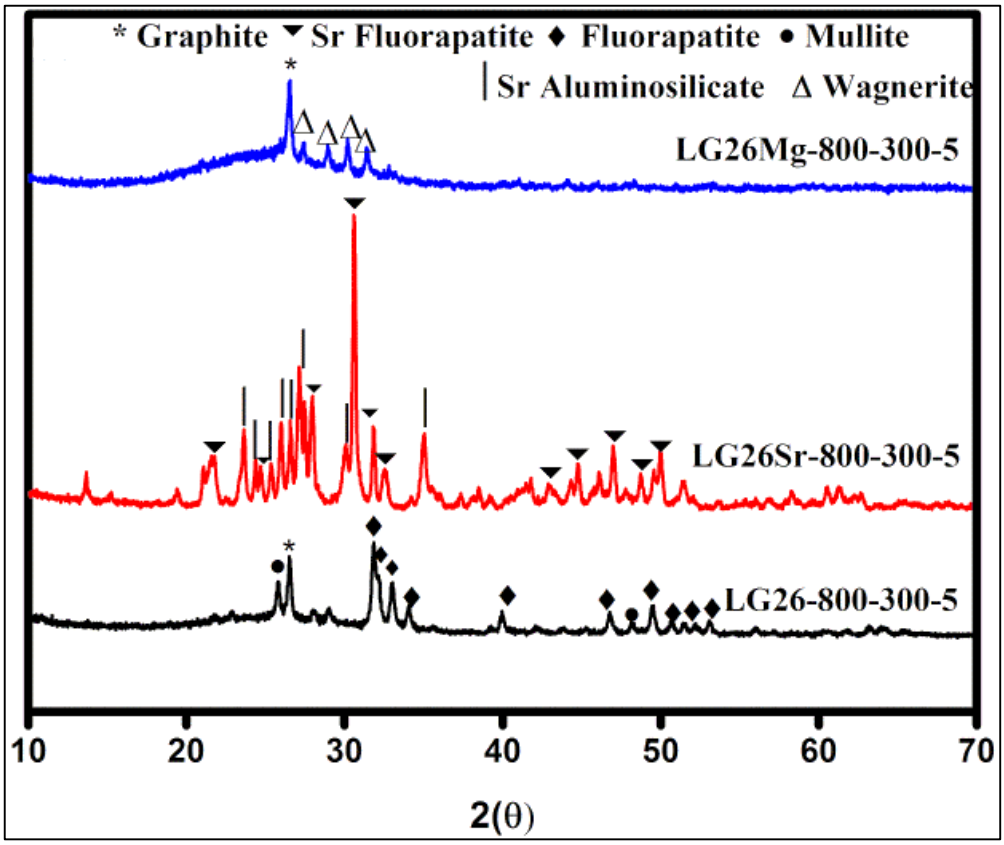

Figure 35: XRD diffractogramms of LG26, LG26Sr and LG26Mg glass ceramics after FAST sintering at 800°C for 5 min with 300°C/min as heating rate

LG26Mg also shows no effect in the crystallisation when compared with 100°C heating rate with 5 min holding time where only wagnerite and graphite were observed along with the amorphous region. Generally, the XRD pattern obtained for 300°C is similar to the XRD pattern of glasses crystallised with 100°C heating rate for 5 min sintering.

Figure 36 shows the difference in the XRD pattern of the glass crystallised at heating rate of 500°C/min with final sintering temperature of 800°C for 5 min. LG26 and LG26Mg show the presence of an amorphous bump in the lower angle of 2θ. LG26Sr shows very little area of

amorphous bump in the pattern when compared with the other two glass ceramics suggesting that the LG26Sr was crystallised much better than the other glass ceramics.

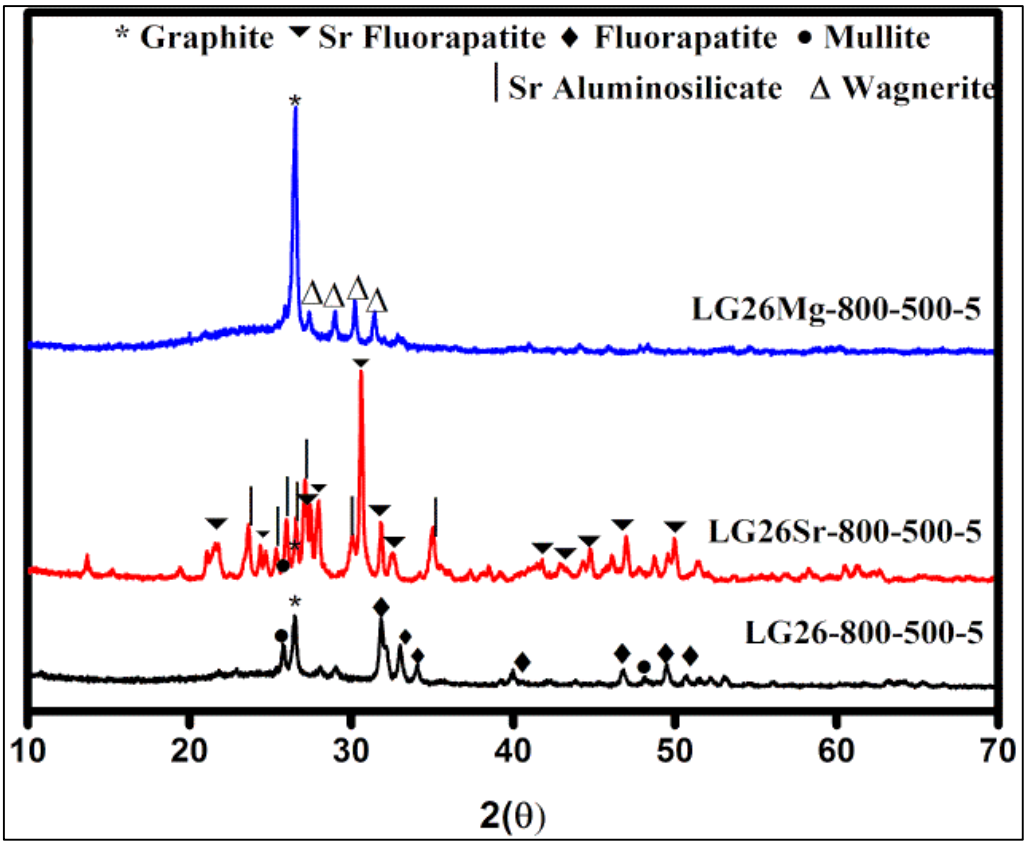

Figure 36: XRD diffractogramms of LG26, LG26Sr and LG26Mg glass ceramics after FAST sintering at 800°C for 5 min with 500°C/min as heating rate

In LG26Sr the presence of both major phases can be noticed but in the case of the other two glass ceramics only one crystal phase can be noted suggesting that increasing the heating to 500°C, the temperature difference between the centre of the glass powder in the die and to the surrounding die wall is high because of non-conductivity of the materials. In order to crystallise at 500°C heating rate and to avoid this temperature difference a longer sintering time is needed for the glass powder to crystallise. The obtained patterns are more or less similar to the patterns obtained for 100°C/min heating rate with 5 min holding time.

3.1.4 Surface Mechanical Properties

Surface mechanical properties were characterised by using the Vickers hardness and nanoindentation technique. Due to limited avalibility of the samples all the measurements were carried out in one sample with 5 indent for hardness test.

Figure 37a shows the Vickers hardness of crystallised glass sintered using FAST. The hardness of the sintered glass shows an increase with increasing the temperature from 700 to 1000ºC. At 700ºC LG26Mg exhibits the highest hardness followed by LG26 and LG26Sr. At all other temperatures, LG26 exhibits the highest value followed by LG26Mg and LG26Sr. The above values of hardness follow the transformation from glass to glass ceramics and correlate well with the obtained XRD patterns discussed in section 5.1.3

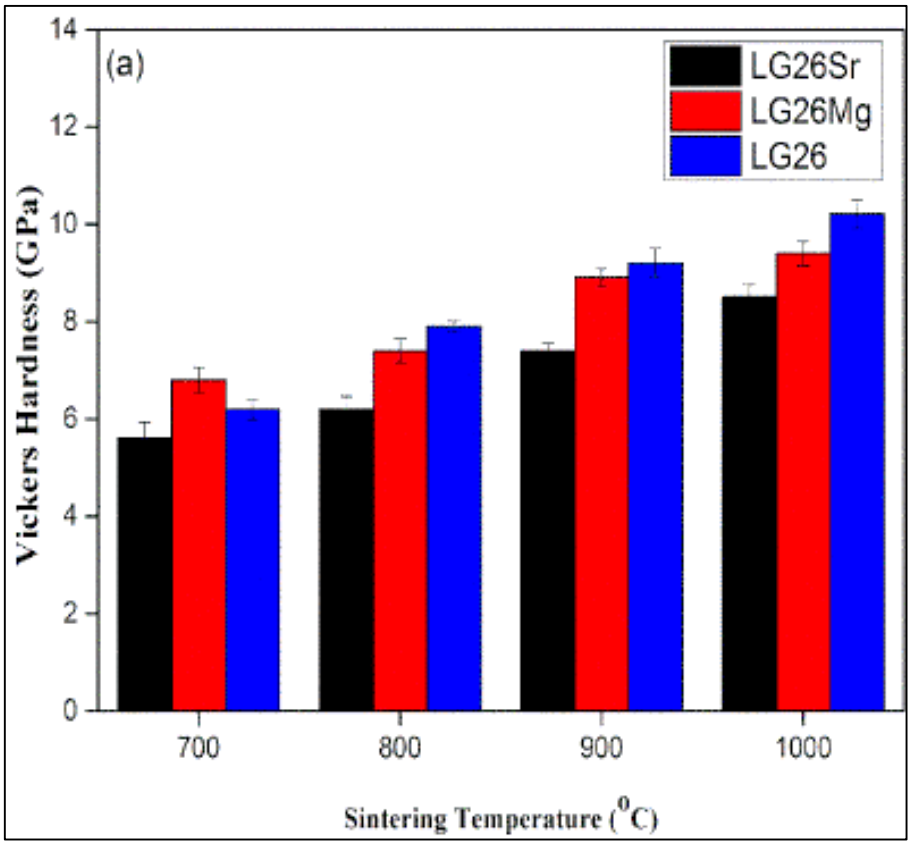

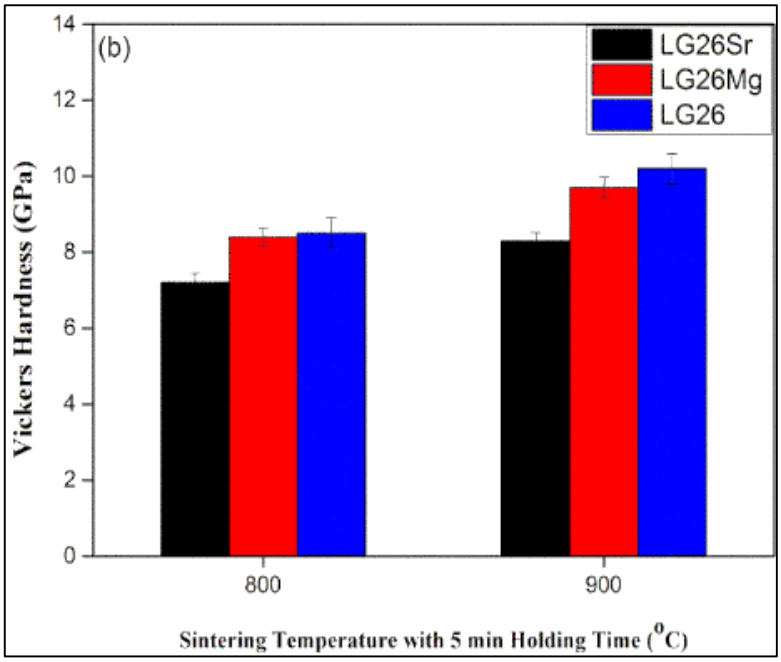

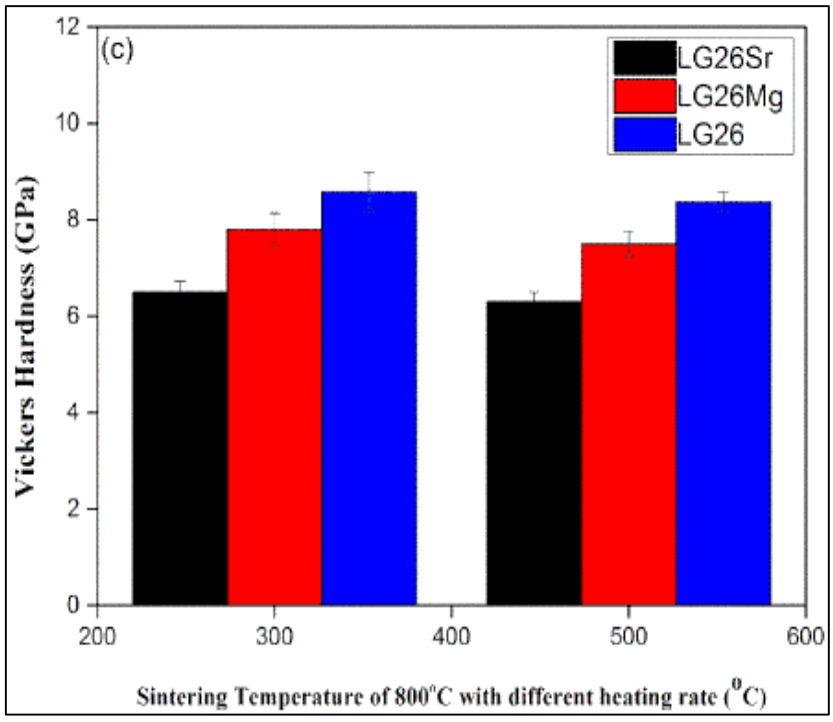

Figure 37: a) Vickers Hardness of the glass ceramics sintered at different temperature, b) Vickers hardness of the Glass sintered with 5 min holding time at two different temperature,c) Vickers hardness of the glass sintered at different heating rate

Figure 37b and Figure 37c show the change in Vickers hardness of the glass sintered with 5 min sintering time and different heating rate. The hardness of these glasses increases when the sintering time was increased showing that the glasses crystallised better with 5 mins holding rather than 1 min holding time.

Figure 38a shows the elastic modulus of the glass sintered at different temperature. Nanoindentation technique was used to measure these properties. The modulus of the LG26Mg shows the highest value when compared with all other glass ceramics. The modulus of LG26Sr remains constant even when increasing the sintering temperature. According to the XRD patterns the glasses were crystallised at lower temperature.

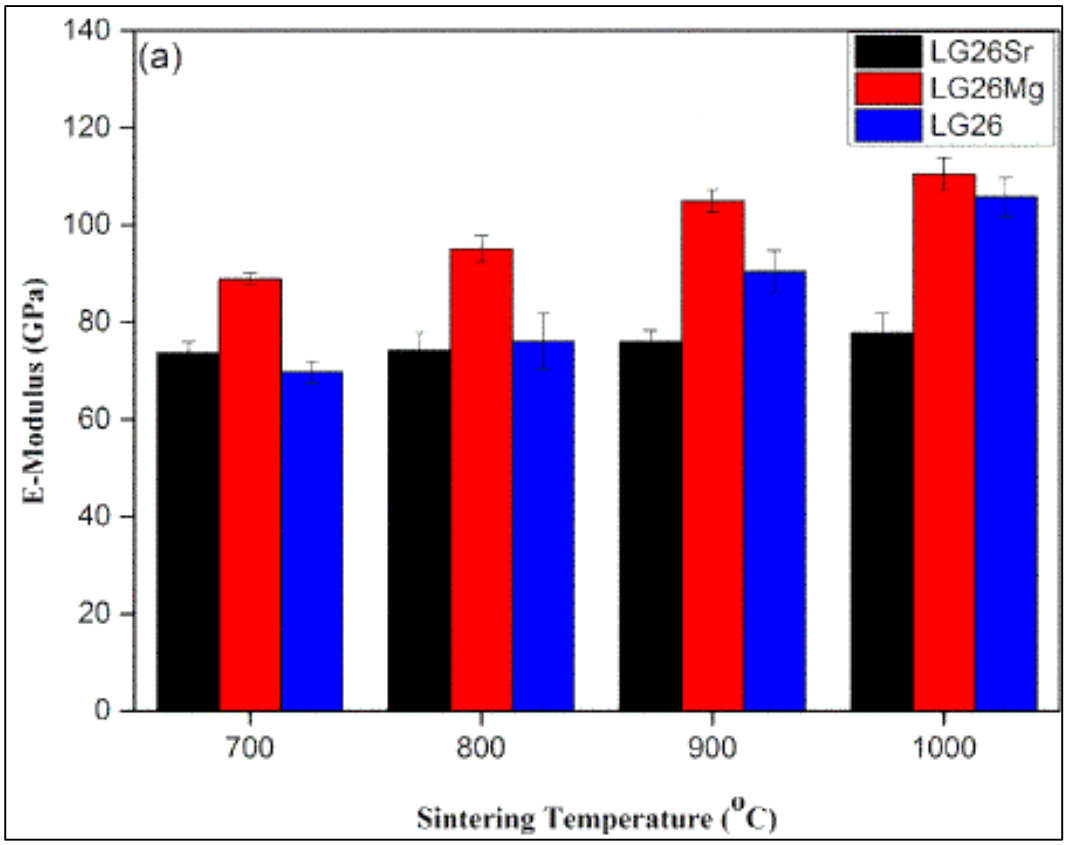

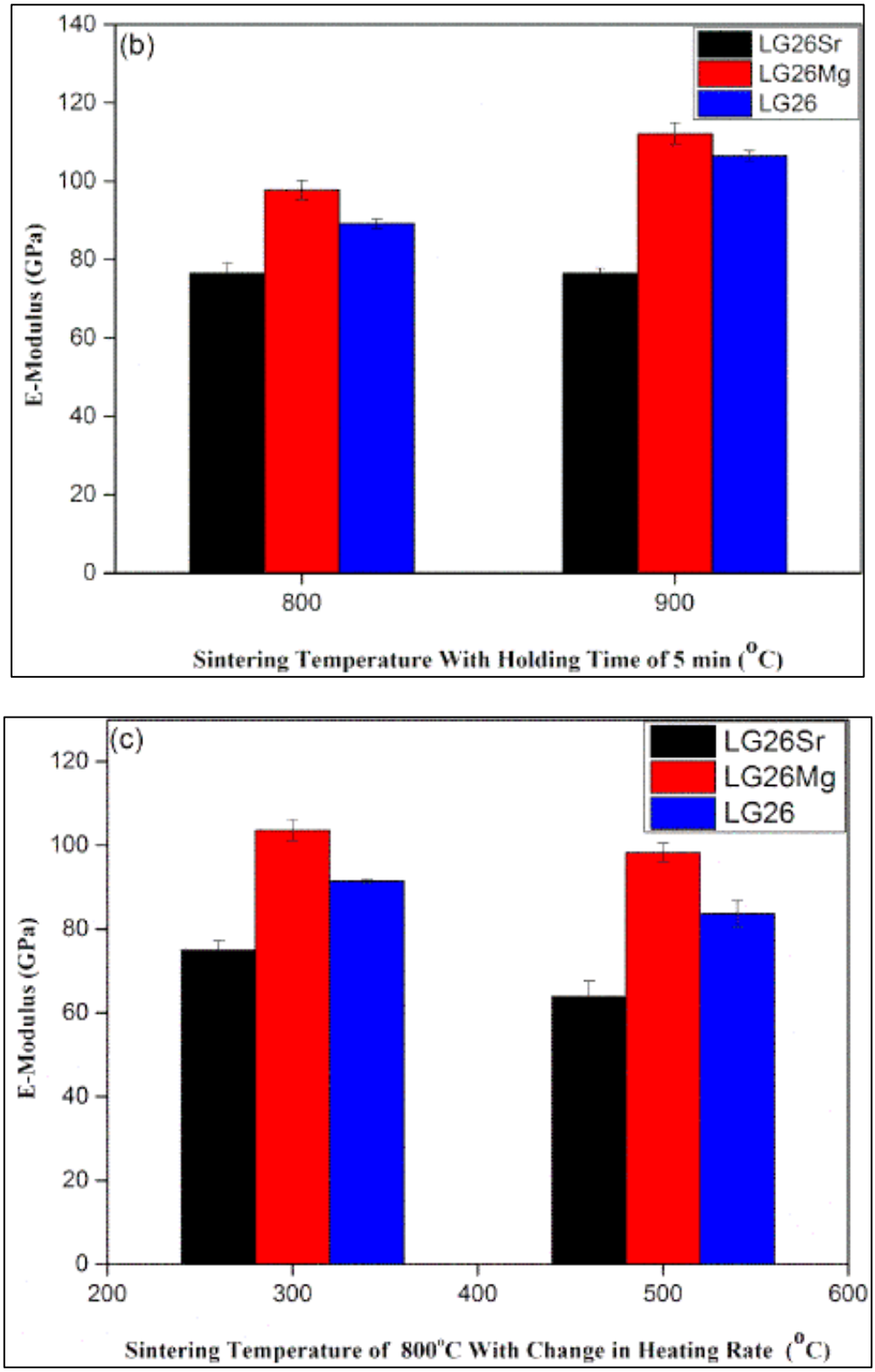

Figure 38: a) E-modulus of glass sintered at different temperature, b) E-modulus of glass sintered with 5 min holding time,c) E-modulus of the glass sintered at 800°C with different heating rate

This might be the final value of modulus that can be obtained for these glasses. During this study, LG26 showed an increase in modulus with increasing the final sintering tenpertaure. LG26Mg shows the highest value of modulus which might be due to the close packing of Mg atoms in the glass system.

Figure 38b and Figure 38c show the change in modulus when changing the sintering time and the heating rate. The value of the elastic modulus increases with increasing the sintering time showing that the glass crystallised better when the sintering time was increased. In the case of changing the heating rate, the elstic modulus decreased which might be due to the small sintering time at the final temperature.

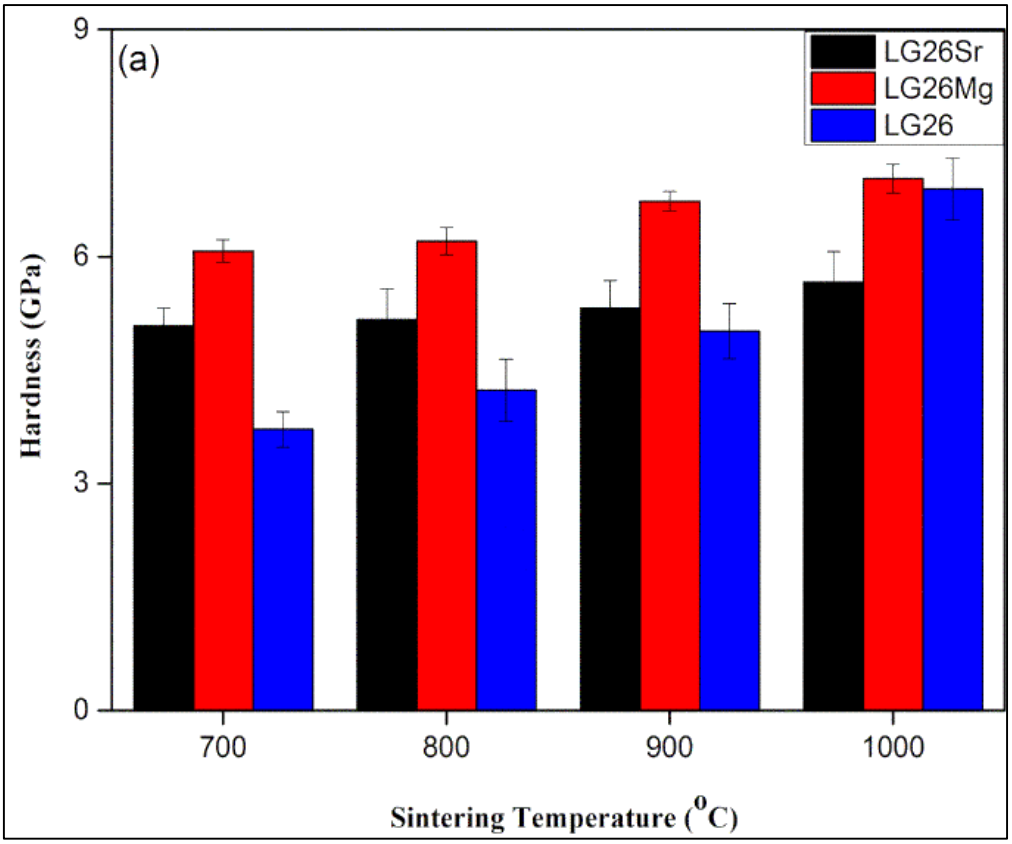

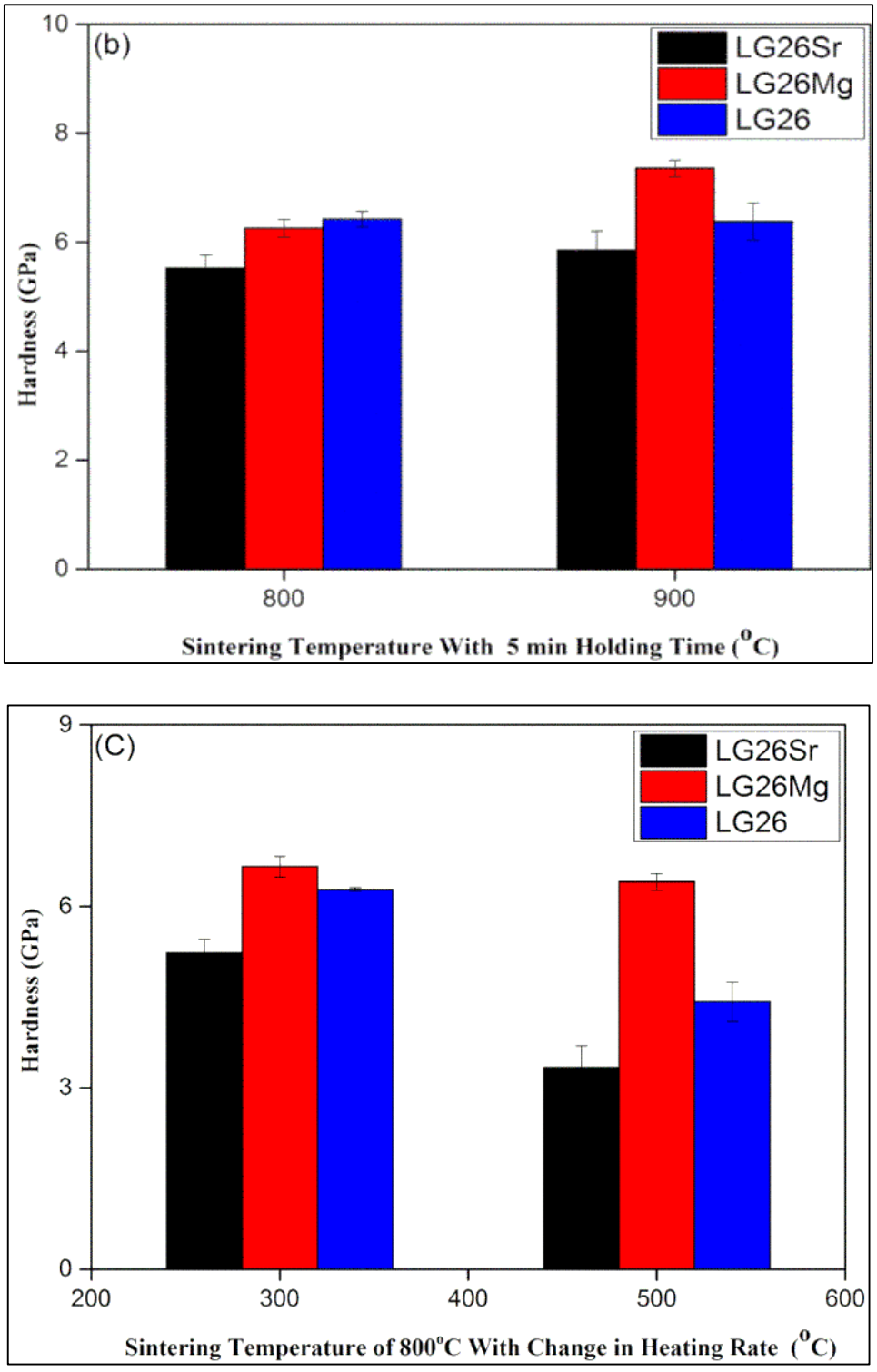

Figure 39: a)Nanoindentation hardness of the glass ceramics sintered at different temperature, b) Nanoindentation hardness of the glass ceramics sintered 5 min holding time, c) Nanoindentation hardness of the glass sintered at 800°C with different heating rate

Figure 39a shows the calculated hardness of these glass ceramics sintered at different temperatures. The value of hardness increased with increasing the final sintering temperature. The obtained hardness values are much lower when compared with the Vickers hardness which might be due to the low applied load for this testing. The hardness of LG26Mg shows the highest value when compared with the other glass compositions. This might be due to the size of Mg atoms which are closely packed in the glass network when compared with Ca and Sr glasses.

The hardness of the LG26 increases gradually along with increasing the sintering temperature which shows the crystallisation in this glass is better with increasing the temperature. In the case of LG26Sr the hardness value remains constant only slight increase can be noted which can be related to the crystallisation. This glass crystallises much better at lower temperatures. The obtained value of hardness might be the final value for this glass ceramics. The reason for the lower value can be related to the size of the Sr atom and packing of this Sr atom in the glass network.

Figure 39b and Figure 39c show the change in the hardness of this glass when changing the sintering time and heating rate. The hardness of this glass improves much better when the glass sintered with the holding time which might be due to better crystallisation with holding time. The hardness decreases when increasing the heating rate of this glass. This might be due to the holding time at the final sintering temperature where the sintering time is not optimum for the glass to crystallise at the higher heating rate.

In general, the obtained properties of this glass are much better when compared with the conventional sintering of these glasses. The Mg glasses show the highest value even when the glass was not fully crystallised. This shows that the mechanical properties of this Mg glass

ceramics can be improved better than LG26 and LG26Sr if additional optimisation of sintering temperature and time were carried out

Tables 27 shows the mechanical properties of the commercially available products of bioceramics. Table 28 shows the comparison of mechanical properties between FAST and conventional sintering process. The glass crystallised using conventional process shows very low value of all the properties when compared with the FAST sintering process. These glasses were cast glasses. The obtained results of FAST better properties when compared with HAP, BioVerit, TCP and 45S5 bioglass but the conventional sintered glass shows much lower properties than the properties of all commercially available bioceramics.

Table 27: Mechanical properties of Bioceramics [12]

Properties	**Ceramics**				**Bioglass**	**Glass-Ceramics**			
	HAP	**Alumina**	**PSZ**	**TCP**	**45S5**	**Ceravital**	**Cerabone**	**Ilmaplant**	**Bioverit**
Density $(g/cm)^3$	3.16	3.93	6	3.07	2.66		3.07		2.8
Hardness HV	600	2300	1300		460	680		500	460
Young's modulus (GPa)	80-110	380	200	33-90	35	100-150	218		70-88

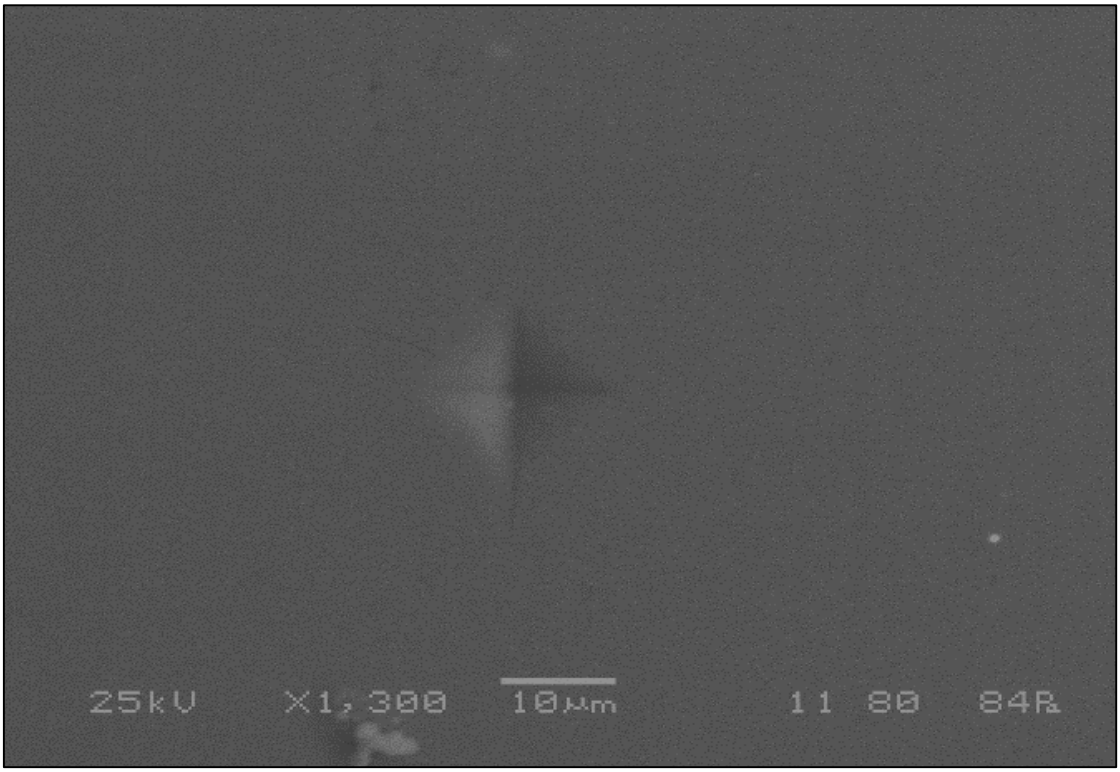

Figure 40: SEM of Vickers indent on LG26

This shows that the glass ceramics produced using the FAST method are stronger than glass ceramics obtained by the conventional sintering process which is an advantage for these glasses for the potential application as bioceramics. This shows that FAST can be used as an alternative method for the fabrication of bioceramics with improved properties in shorter sintering time.

Table 28: Comparison of mechanical properties between FAST and conventional sintering

Glass	**FAST sintering at 1000ºC**			**FAST with 5 min at 900ºC**			**Conventional sintering**		
	LG26	**LG26Sr**	**LG26Mg**	**LG26**	**LG26Sr**	**LG26Mg**	**LG26**	**LG26Sr**	**LG26Mg**
Density (g/cm)3	2.86	3.19	2.74	2.9	3.17	2.74	2.8	3.0	2.8
Hardness (GPa)	6.8	5.6	7.03	6.8	5.85	7.35	2.3	0.68	3.57
E-modulus (GPa)	105	77	110	106	76	112	76	12	80

3.1.5 Microstructure of LG26 glass ceramic

The SEM images of LG26 glass ceramic sintered at 900ºC with 5 min holding time were shown in the figure 41. This images clears show the presence of needle like crystals which belongs to

the fluorapatite crystal phases. This sample were mirror polished and etched using 48% HF for 1 sec. The results of the LG26Mg sintered at similar temperature was not present in this work due to absence of crystal phases on the surface this is due HF acid which dissolves the crystals on the surface. As reported in the previous literatures the needle like apatite crystals are clearly seen in the SEM micrograph of LG26 glass ceramic with the crystal size of more than 2 µm.

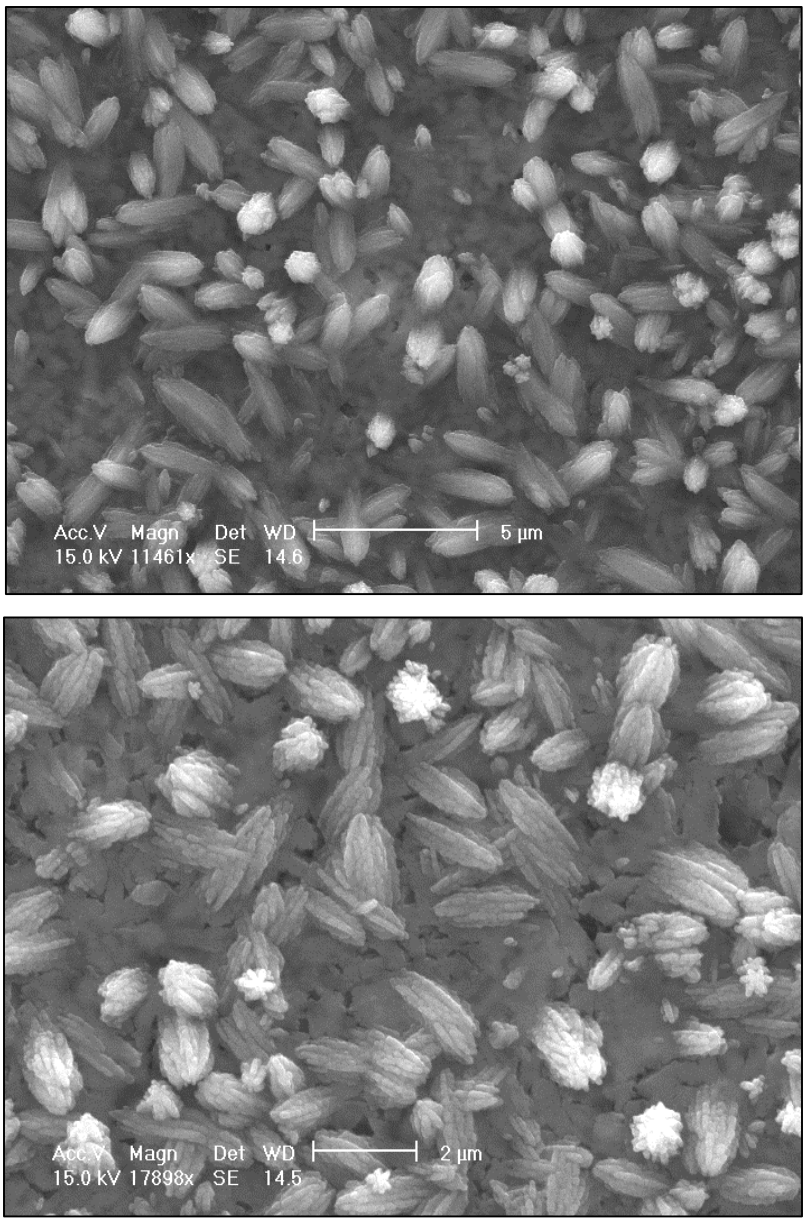

Figure 41: SEM of LG26 glass ceramic sintered at 1000^{o}C

3.1.6 Summery

In the present work, we investigated the processing, mechanical properties and microstructural development of fluoro alumina silicate glass with substitution of Calcium, Strontium and Magnesium. These glass were crystallised using the advanced sintering technique called FAST sintering and the results were compared with previous work carried out on this glass system. The FAST sintering was carried using FCT system at Queen Marry University London.

1. The process of crystallisation using FAST was studied in this work.
2. The glass with composition of $4.5SiO_2–3Al2O_3–1.5P_2O_5–3CaO–2CaF_2$ was used along with the substation of Mg and Sr for Ca
3. The optimisation process was carried out using trial and error method due to lack of thermal analysis date for high heating rate
4. Glass were sintered by change in final sintering temperature from 700 ^oC to 1000 ^oC with heating rate of 100^oC and 1 min sintering time at each final temperature
5. Sintering of glasses were also carried out using change in heating rate and also change in holding time

3.1.6.1 Glass crystallised at different sintering temperature with 1 min sintering time

1. The detail study on the crystallisation process with change in temperature gives an idea of processing condition that can be used for sintering these glasses in FAST technique
2. The Density of the glass ceramics was improved when compared with previous study on the crystallisation behaviour of this glass system [46].
3. The obtained surface mechanical properties shows an higher value for the glass crystallised at 1000^oC with 1 min holding when compared other glass system [12].

4. Crystallography studies on these glass shows no change in the crystalline phase when compared previous work [46] . The obtained XRD peaks are sharper than the one obtained from previous work.
5. The formation of both the crystals phases can be clearly seen at this glass system crystallised at 1000^{o}C using FAST for 1 min which shows that the glass can be crystallised at lower temperature with short sintering time when compared with previous reported works.

3.1.6.2 Glass crystallised with sintering time of 5 min at final sintering temperature

1. The density of these glass ceramics were improved when compared with 1 min sintering time
2. The formation first crystal phase can be seen in all the glass sintered at 800^{o}C with the presence of glassy phase at lower diffraction angle. Which shows that the partial crystallisation can be obtained using FAST
3. In the case of glass crystallised at 900^{o}C complete crystallisation was achieved with properties equal to glass crystallised at 1000^{o}C for 1 min sintering time
4. The obtained mechanical properties of the glass ceramics sintered at 900^{o}C with 5 min shows better value when compared with conventional sintering process and few commercially available bioceramics.
5. Finally with longer holding time this glass crystallise better even at low temperature with short sintering time when compared with previous works reported.

3.1.6.3 Glass crystallised with change in heating rate

1. The crystallised with different heating rate show low value of density when compared with all other processing condition used in FAST technique which is due to the presence of glassy phase.

2. The XRD of this glass crystallised at 300^{o}C/min show the crystallisation of only one phases in calcium and magnesium glass but the strontium glass shows presence of both the crystal phases.
3. The mechanical properties of these glass are much low when compared other processing conditions.
4. Finally the heating rate no effect in the crystallisation of the glass due to short sintering time at peak temperature.

3.2 Results & Discussion-FAST Sintering of Glass using Dr.Sinter

3.2.1 Density measurements

The glass powders of different composition were crystallized at different sintering schedule by changing the holding time and temperature to obtain the final glass-ceramics with better properties. Figure 42 shows the changes in the density of the samples crystallized by FAST. Table 29 shows the variations in the density of LG26 glass-ceramics samples sintered by changing the parameters of the FAST for better crystallized samples. Experimental density of the single step sintered LG26 glass powder is much lower than the samples sintered at two step sintering method. These low density value are much expected since samples are not crystallized properly which is seen from the XRD graph. This confirms that single step sintered samples were embedded with both amorphous and the crystallized phases.

Figure 42a clearly shows that the study increase in the density of the samples when changing the sintering parameters. The highest density of 3.11g/cm^3 was obtained for the samples sintered at 700/800^{o}C with holding time of 5 min at both the temperature. These were confirmed by the XRD which shows good crystal phases formation at these temperatures. However the LG26 glass powder sintered at 800^{o}C did not produce any crystallized samples due melting of the glass powder on the sides of the graphite punch. This is one of the reasons to follow the two step sintering procedure for the rest of the experiments and the Sr substituted glass powders. It is to note that the final temperature of the crystallized samples is just above the first crystallization temperature of the LG26 glasses powders.

Figure 42a clearly shows that the study increase in the density of the samples when changing the sintering parameters. The highest density of 3.11g/cm^3 was obtained for the samples sintered at 700/800^{o}C with holding time of 5 min at both the temperature. These were confirmed by the XRD which shows good crystal phases formation at these temperatures.

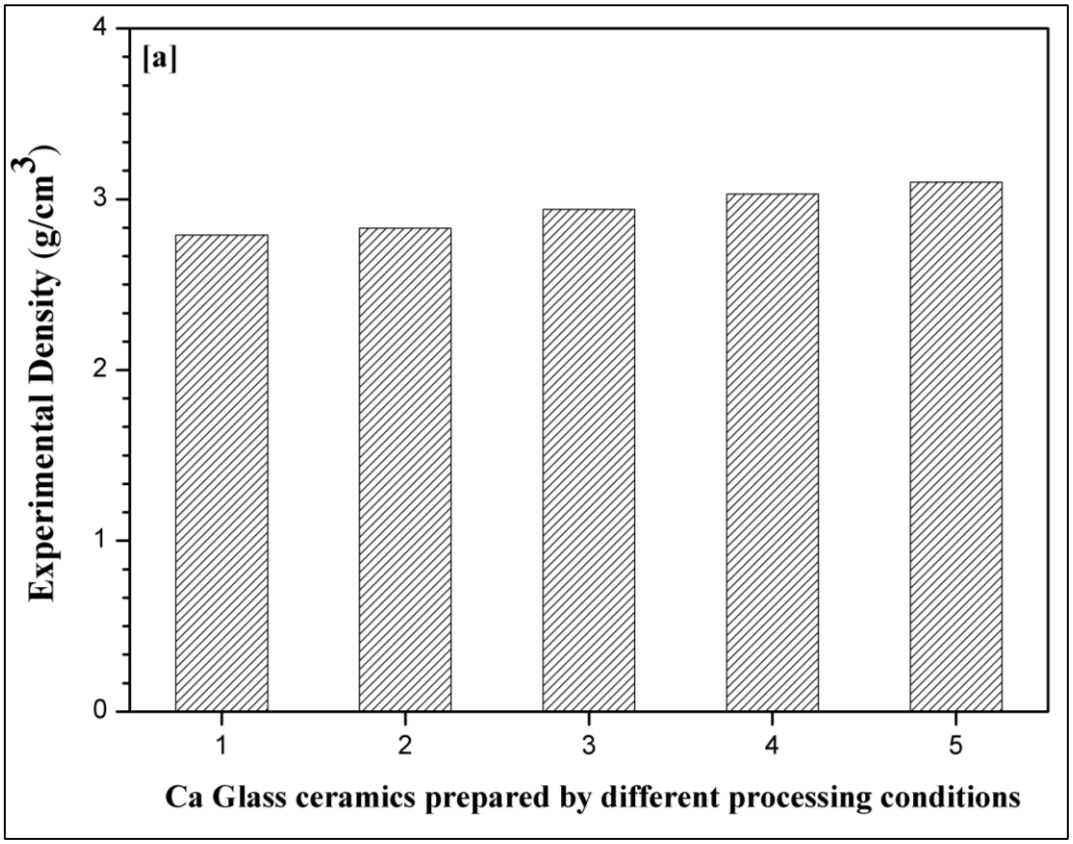

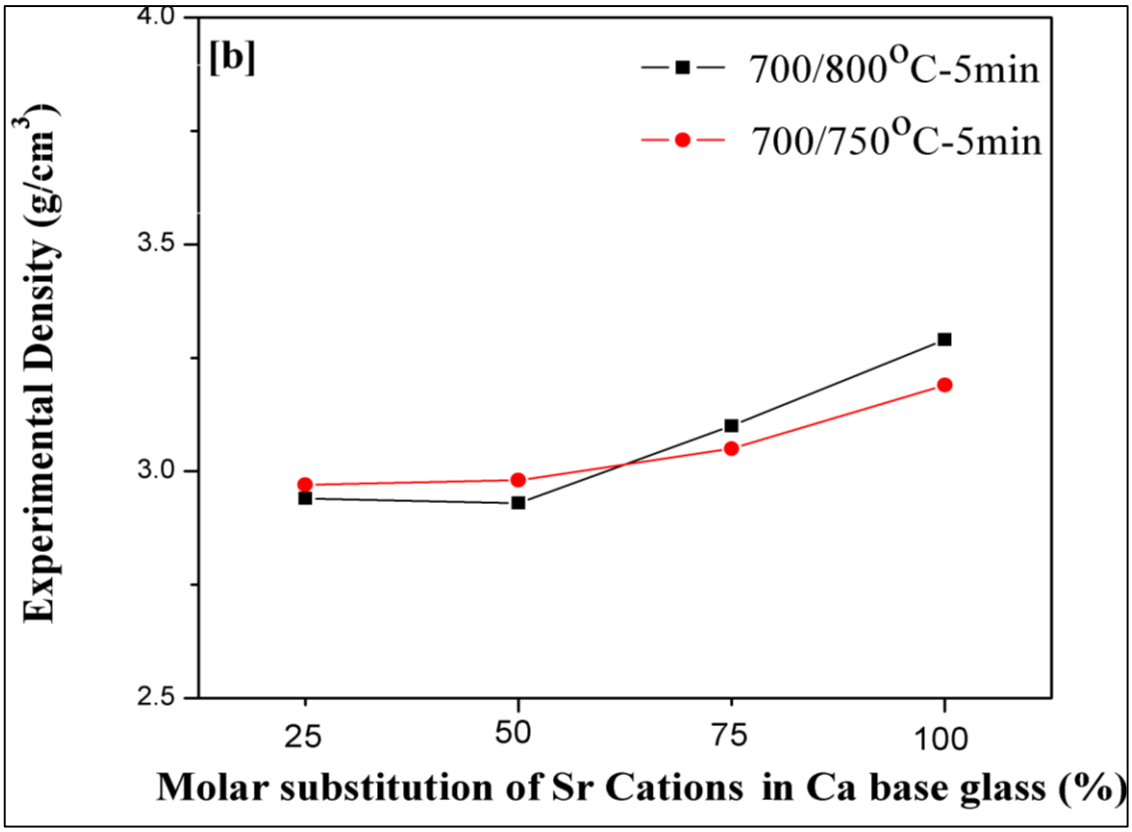

Figure 42:a) LG26 Glass ceramics sintered at different processing condition b) Density of LG26Sr substituted Glass-ceramics sintered at different temperature

However the LG26 glass powder sintered at 800ºC did not produce any crystallized samples due melting of the glass powder on the sides of the graphite punch.This is one of the reasons to follow the two step sintering procedure for the rest of the experiments and the Sr substituted glass powders. It is to note that the final temperature of the crystallized samples is just above the first crystallization temperature of the LG26 glasses powders.

Table 29: Density of Lg26 with different sintering Parameters

S.no	Glass-ceramics	Temperature	Holding time	Pressure	Experimental density
1	LG26	700ºC	5 Min	38 MPa	2.79±0.3
2	LG26	700ºC	10 Min	38 Mpa	2.83±0.37
3	LG26	700/750 ºC	5/2 Min	38 MPa	2.94±0.02
4	LG26	700/750 ºC	5/5 Min	38 MPa	3.03±0.2
5	LG26	700/800 ºC	5/5 Min	38 MPa	3.10±0.27
6	LG26	800 ºC	5 Min	38 MPa	-

Table 30: Density of the different molar content of crystallized Sr glass powder

S.No	Temperature	Holding time	Pressure	Experimental Density in (g/cm^3)				
				LG26	**LG26Sr1**	**LG26Sr2**	**LG26Sr3**	**LG26Sr4**
1	700/800ºC	5 Min	38 MPa	3.10±0.2	2.94±0.17	2.93±0.20	3.10±0.13	3.29±0.28
2	700/750ºC	5 Min	38 MPa	3.03±0.27	2.97±0.29	2.98±0.16	3.05±0.32	3.19±0.19

Figure 42b and Table 30 shows the density changes of Sr substituted samples. These Sr substituted glass powders were sintered by the two step method of sintering of 700/750ºC and 700/800ºC for 5 min with 38 Mpa as the pressure maintained inside the die. The experimental density results of different molar ratio of Sr substituted samples showed huge variations in the density results when compared with the LG26 crystallized samples. The 25% and 50% substitution of Sr showed the very low density when compared to the density of the 100% substitution. This might be the reason of the mixed cation effect since the 25% and 50% substitution of Sr glass powder is having the Ca^{2+} as major content then the Sr^{2+} and the ionic radius of Ca cations (0.94nm) is lesser then the Sr cations (1.16nm) ionic radius which might decrease the density of the crystallized samples from the LG26 glass-ceramic this will be one

of the reason for the less intensity of the peaks at XRD graph. In case of 75% and 100% substitution the density of the samples is increased much higher than the LG26 samples and very good peak profile were also noted in the XRD graph. It clearly shows that the decreases in Ca content increases the density of the crystallized samples.

3.2.2 XRD analysis

X-Ray diffraction studies were carried out to understand the crystallization of the glass powder by FAST. Figure 43a shows the XRD graph of LG26 samples using the different sintering parameters. The XRD analysis shows that the fluorapatite is dominant phases for all the crystallized samples while mullite as the secondary phase with little formation of $AlPO_4$ and Anorthite formation. However, the formation of crystal phases by changing the sintering parameters is clearly seen in the XRD graph. In the case of samples crystallized at 700^{o}C for 0 min and 10 min in single step sintering shows only the presence of fluorapatite were the secondary crystal phase of mullite is just initiated which is not crystallized fully. Comparing the peak intensity it is confirmed that fluorapatite presence is much dominant than mullite which indicate that the mullite phase is a secondary phases in this glass system. The detail real time neutron investigation on the crystallization of this glass by A.Stamboulis et al[152] reviled the fluorapatite were the first phases crystallize at low temperature leaving mullite to form at higher temperature. Interestingly their results correlate with this XRD studies on LG26 crystallization by FAST. The dominant fluorapatite phase in the XRD graphs shows that temperature is not optimum for mullite phase to crystallize in the single step sintering. However, in the case two step sintering there is a significant improvement in the crystallization of both the phases were observed. It shows that increasing the 50^{o}C from the first holding temperature is enough for mullite phase to crystallize. Further understanding this we followed to optimize the holding time for the samples to crystallize. The sintering performed with different holding time was carried out to understand the crystallization in FAST. The

temperature of 700/750 for 5/0 min shows the improve peak intensity of the mullite than the fluorapatite peaks. Crystallization of fluorapatite and mullite at 700/750 for 5 min holding shows significant improvement in the peak intensity when compared with single step of 0 and 10 min and two-step of 5 and 0 min. It clearly shows the mullite formation takes place much better by changing the holding time. Finally increasing the second temperature to 800^{o}C with the holding time of 5 min shows the better orientation of crystal phases when compared with all other temperature. Interestingly at this higher temperature we noticed the formation of small phases $AlPO_4$ and Anorthite.

Significant improvements in the crystallisation were observed in the case of the two-step sintered samples with more intense mullite and fluorapatite peaks because of this reason the two step sintering were followed for the Sr substitution.

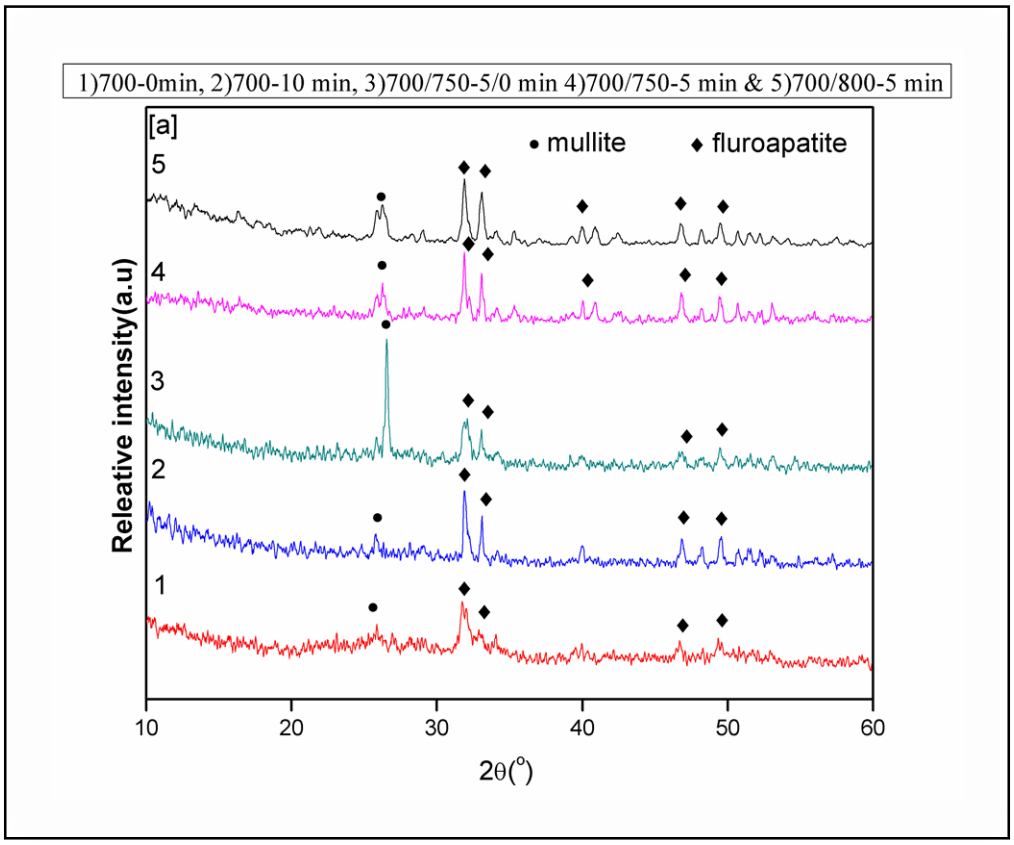

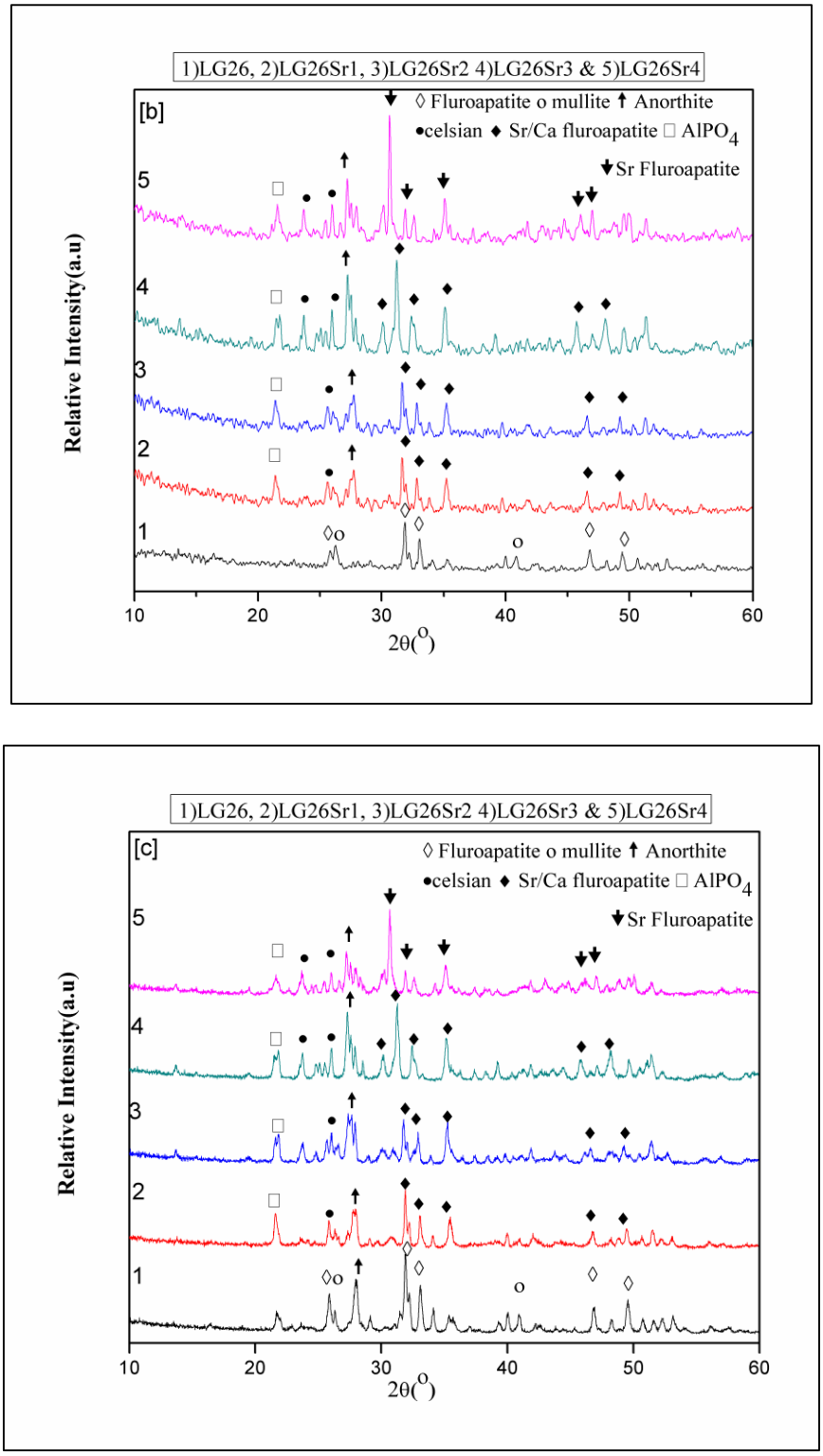

Figure 43: a) X-Ray Diffraction of LG26 Crystallized at Different Temperature, b) X-Ray Diffraction of LG26 and Sr Substitution Glass-Ceramics Crystallized at 700/750 with 5 min Holding, c) X-Ray Diffraction of LG26 and Sr Substitution Glass-Ceramics Crystallized at 700/800 with 5 min Holding

However the substitution of strontium in the LG26 base glass resulted in the formation of a different phase with changes in the peak intensity. The phases identified for the Sr substation were Sr Celsian, mixed Sr/Ca Fluorapatite and Sr fluorapatite as dominant phases shown in Figures 43b and 43c. Figure 43b shows the XRD patterns of Sr substituted samples crystallized at 700/750ºC with holding time of 5 min at both temperature and Figure 43c shows the XRD patterns of the same samples heated at a temperature of 700/800ºC with the 5 min holding time at both temperature . A lack of crystalline was noted for the 25% and 50% Sr substituted samples heated at both temperatures, This behaviour of relatively lower peak intensities and less number of distinguishable peaks can be correlated with the temperature for crystallization. The followed temperature is optimized for the LG26 only which states that the optimized temperature is not high enough for the glass powder to crystallize. However, substitution of strontium resulted in the formation of the monoclinic celsian as the secondary phase with $AlPO_4$and Anorthite was also observed in all Sr substituted compositions.

3.2.3 Surface Mechanical Properties

Figure 44 and Table 30 shows the hardness of LG26 by changing the crystallization temperature. Comparing the hardness value with single step and two step sintering method, single step sintering is relatively lower than the two step process. In Figure 44a it clearly shows the increase of hardness from single step sintering to two step sintering process. The error bars in Figure 44 represents the standard deviations for the 5 set of indentations. Changes in hardness by changing the crystallization temperature shows that sintering temperature and time plays the major role in determination of materials properties. The hardness of ~11 GPa shows that sample sintered at 700/800^{o}C for 5 min is crystallized phases are much higher than the amorphous glass phases. The higher density obtained correlates well with hardness values. It shows that Ca glass ceramics crystallized by this processes possess more brittle in nature. The low hardness value of single step sintering might be the presence of higher glass phases of final

crystallized glass ceramics is also shown in Figure 43 of XRD graph. SEM image of Vickers's Hardness is shown in Figure 45 illustrate that absence of cracks in the corners of indent. R.G.Hill et al[80]performed similar kind of experiments by using hot press sintering with varying the alumina content in the glass system their hardness result of $3Al_2O_3$ substituted crystallized glass exhibit the Vickers hardness of 645.5HV for the samples pressed at 1200^oC the obtained value by FAST shows that this materials exhibit highest hardness value.

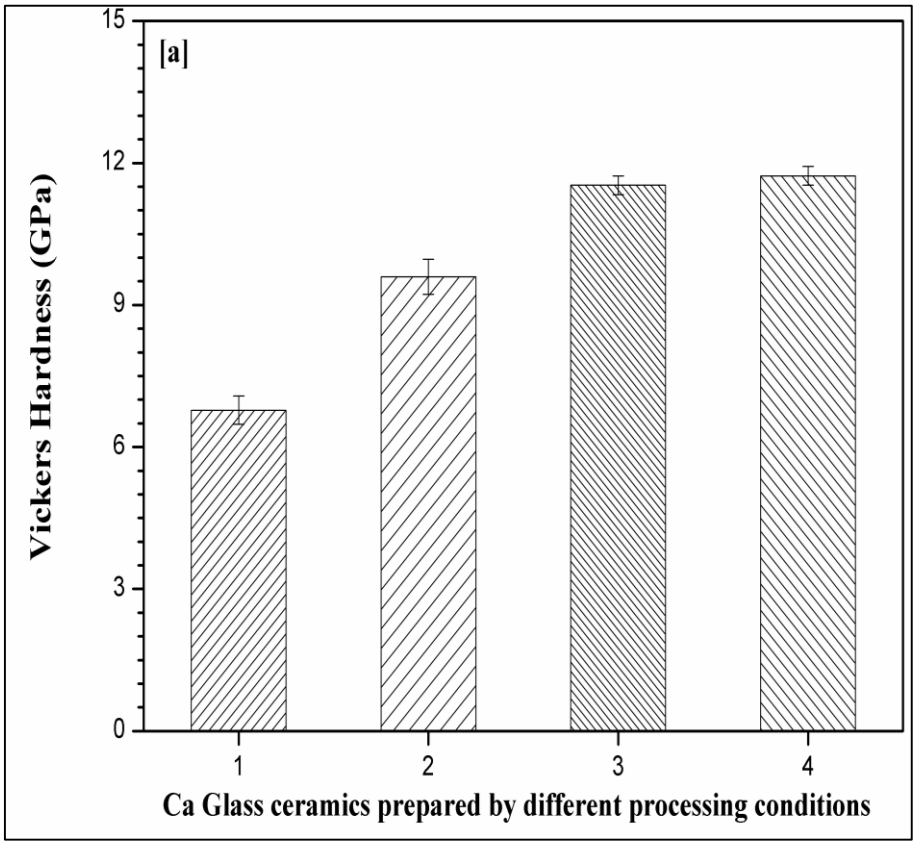

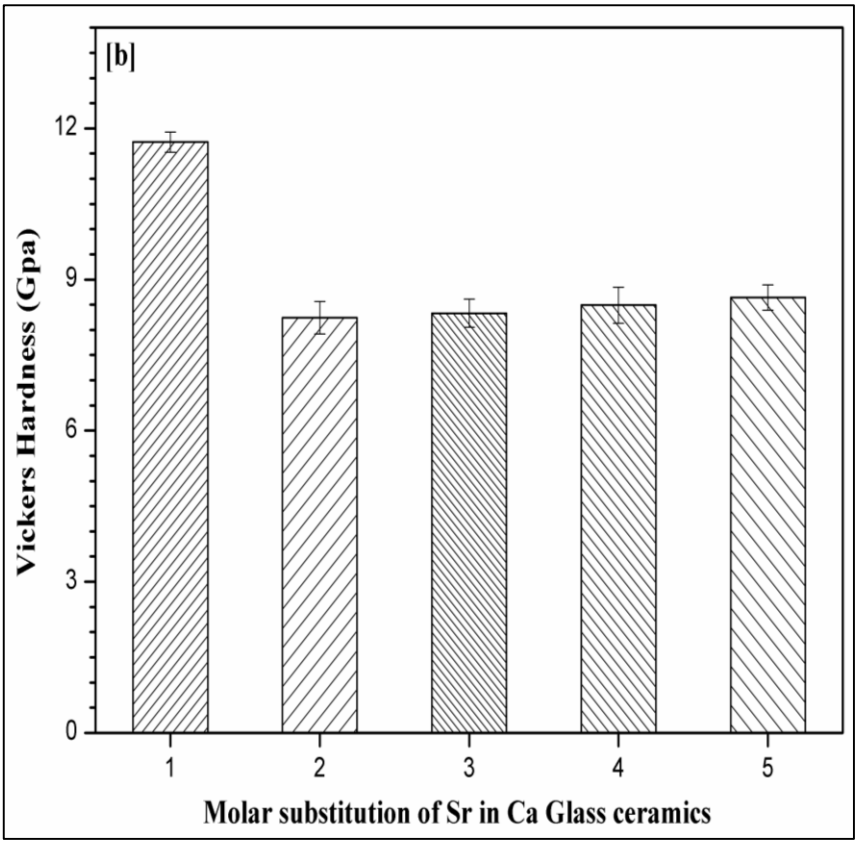

Figure 44: a) Hardness of LG26 glass ceramics crystallised at different temperature, b) Hardness of LG26 and Sr substituted glass ceramics

Figure 44 and Table 31 indicates the hardness of Sr substituted crystallized samples by two step method. There is significant reduction in the Hardness of the Sr substituted samples when compared with the Ca. Figure 44b clearly shows that increasing the Sr substitution the hardness value tends to increase. The minimum hardness value is recorded for LG26Sr1. The hardness value of Sr substituted samples clearly shows high amount of remaining amorphous glass phase in crystallized glass. This is the evidence for the obtained density. These phenomena indicate that Ca substituted glass-ceramic crystallized in bulk at the optimized temperature, but in Sr substituted samples the crystallization was taking place only on the surface of the samples and remains partially amorphous under the surface of the samples. Since most of the surface was removed during the polishing, the reported hardness is the bulk hardness of the FAST crystallized samples.

The result of the nanoindentation was shown in the Figure 46. It shows the mean E-modulus of each indentation placed in one sample. All these experiments were performed on samples crystallized at 700^{o}C and 800^{o}C for 5 min. The E- modulus of Ca is about 120GPa. Since the surface of the glass ceramic samples was polished before the measurement, it is expected that crystal phases that might be present on the surface due to surface crystallisation most likely were removed. Consequently, the measured modulus is due to the crystal phases present in the bulk of the material as well as the process followed for the crystallisation. The nanoindentation of Sr substituted glass-ceramics was very low when compared with the Ca. This is an indication that the parameters followed by FAST were not appropriate for the glass system and did not lead to a high degree of crystallisation leading to lower E-modulus values. One would expect that the presence of a celsian crystal phase would most likely improve stiffness. However, in our case there is a combination of factors including degree of crystallisation and crystal phases. Figure 47 shows the changes in the fracture toughness of Ca and Sr substituted Ca glass ceramics.

Table 31: Surface Mechanical properties of LG26 and LG26Sr Glass ceramics

Mechanical properties			
Glass ceramics	**Vickers Hardness (GPa)**	**Fracture Toughness (Mpa m$^{1/2}$)**	**E-Modulus (GPa)**
LG26	11.73±0.2	1.60±0.05	125.91±0.77
LG26Sr1	8.24±0.32	1.06±0.08	83.85±0.85
LG26Sr2	8.33±0.28	1.10±0.04	78.18±1.08
LG26Sr3	8.49±0.36	1.34±0.05	76.55±1.35
LG26Sr4	8.64±0.25	1.54±0.05	83.14±0.75

Table 31 shows the fracture toughness values. For the fracture toughness analysis we followed the Anstis method. This method is commonly used for analysing the surface fracture toughness. For measuring the fracture toughness by the Anstis method, the E-modulus of the materials is required and was obtained by conducting nanoindentation on the surface of the samples. The

measured fracture toughness values for all compositions varied in the range of 1.05-1.6 $MPa.m^{1/2}$ as shown in Table 31.

The values however, were not as high as compared to the earlier data reported elsewhere. On the other hand, it should be mentioned that the present work did not involve any post processing heat treatment, which can be very important for the degree of crystallization.

Table 32: Vickers Hardness of LG26 glass ceramics

Glass ceramics	Sintering Temperature and Time	Vickers Hardness GPa
LG26	**700ºC-10 min**	6.78±0.3
LG26	**700/750ºC-5/0 min**	9.6±0.37
LG26	**700/750ºC-5 min**	11.53±0.2
LG26	**700/800ºC- 5min**	11.73±0.2

Though the fracture toughness recorded for these samples is lower when compared with early work because the early reported work was taken place at higher temperature of above 1100ºC with varying holding time of 1 to 8 hr depending on the composition. In this work, the low fracture toughness for Sr substituted glass ceramics can be attributed to two reasons; one is the degree of crystallization and the second is the nature of crystal phases formed during crystallization. The reported early work by R.G.Hill [80] on hot press sintering suggested that the lower fracture toughness can be attributed to the formation of anorthite. In the case of Sr substituted glass ceramics, the similar phases were formed during crystallization. The SEM of 2 kg indent on the surface of the samples is shown in Figure 48 and shows that the absence of crack blunting or pull-out is due to no toughening mechanism on the surface. These measurements were carried out on the heat treated glass samples at 700/800ºC for 5 min.

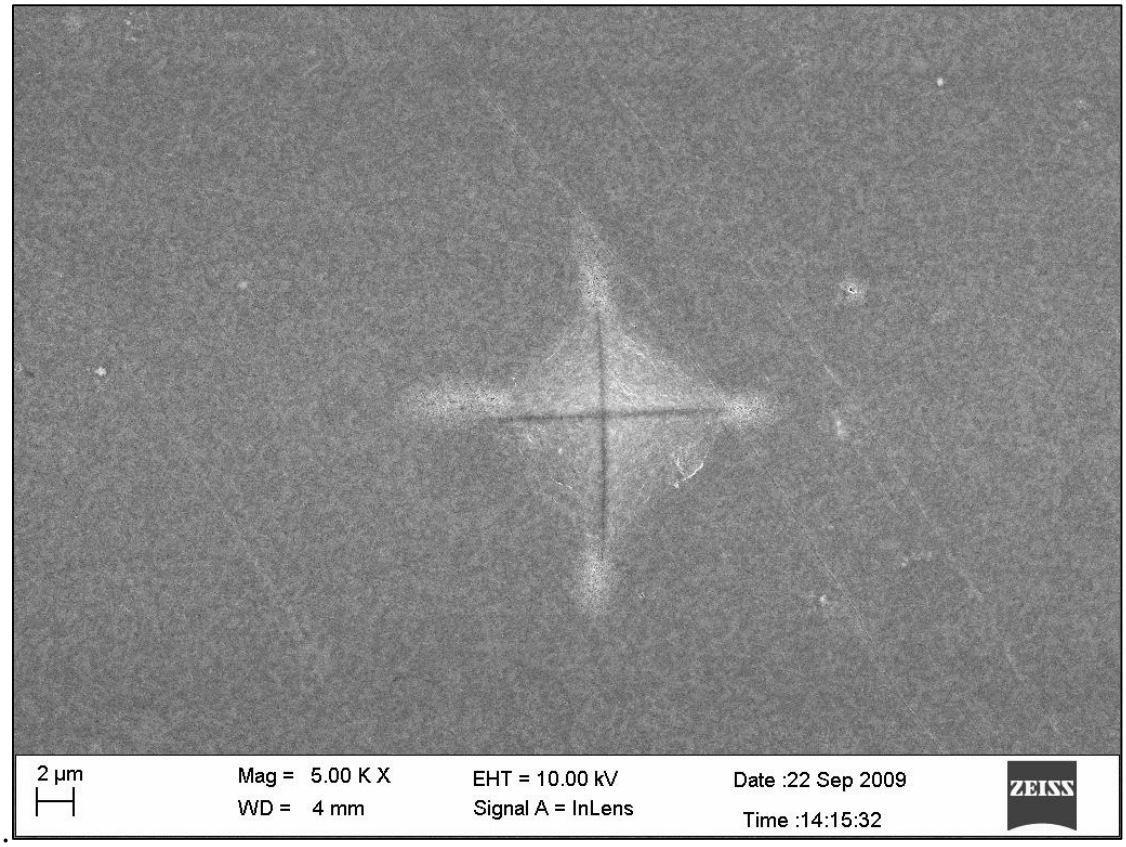

Figure 45:SEM of Vickers indent on LG26 glass ceramics

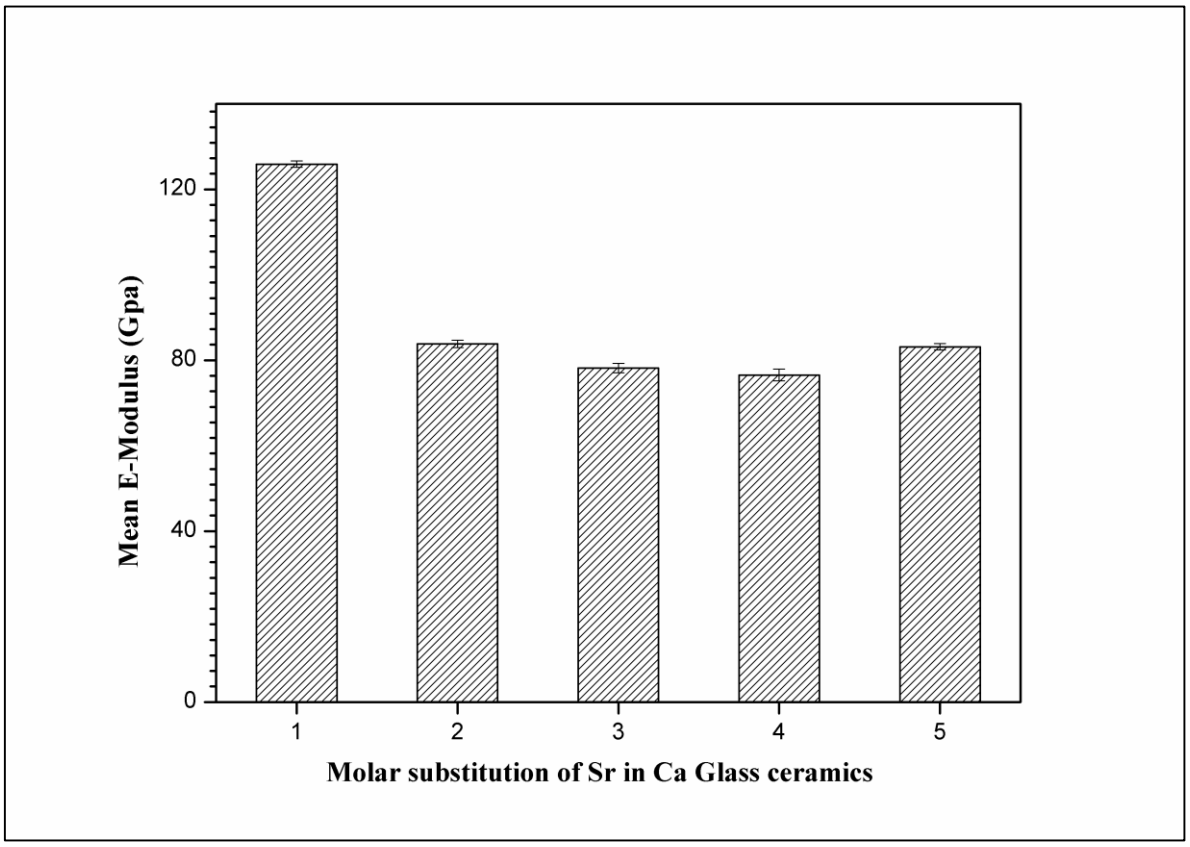

Figure 46: E-modulus of LG26 and Sr substituted glass ceramics

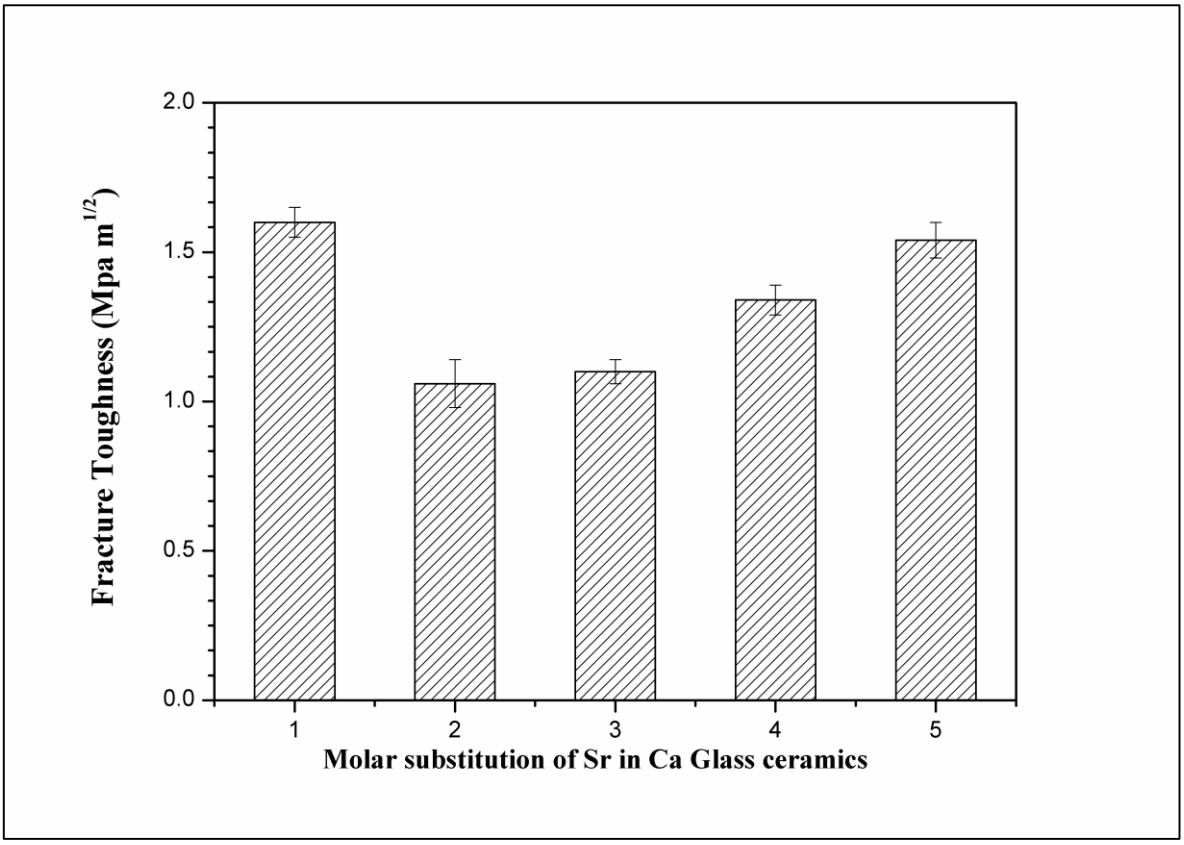

Figure 47: Fracture toughness of LG26 and Sr substituted glass ceramics

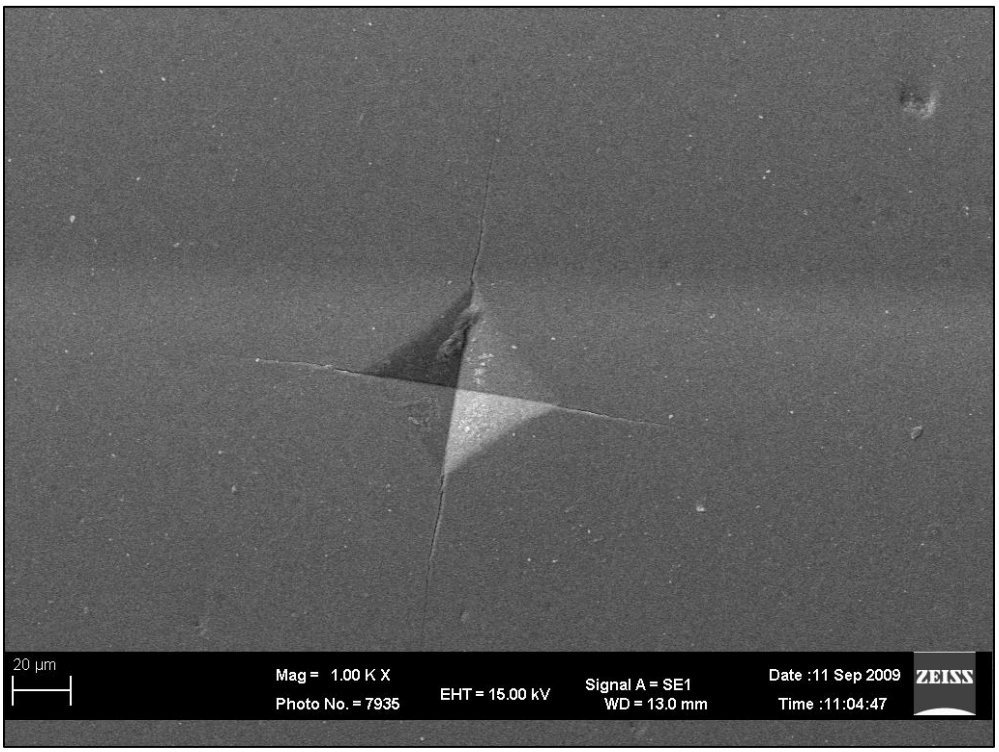

Figure 48: SEM of Vickers indentation of 2Kg of applied load of fracture toughness testing by Anstis method

3.2.4 Microstructural Studies

The microstructural studies on all the crystallized samples were carried out to understand the crystal morphology of glass-ceramics. Figure 49a shows the SEM observation of the LG26 samples. This LG26 crystallized samples were mechanically fractured into two pieces while trying to perform the E-modulus experiment by generating the impulse on the samples. We used that fracture samples to understand the behaviour of the crystal system under the mechanical treatment. SEM image of these fractured samples shows interlocking needle like crystals system which is oriented like blocking the fracture on the crystallized samples. This needle shape crystals are the fluorapatite crystals which interlock with the mullite crystals phases. Initially the interlocking of crystal take place during the crystallization process where the fluorapatite forms first in the glass and mullite phase forms second by this formation interlocking of fluorapatite with mullite phase was formed.

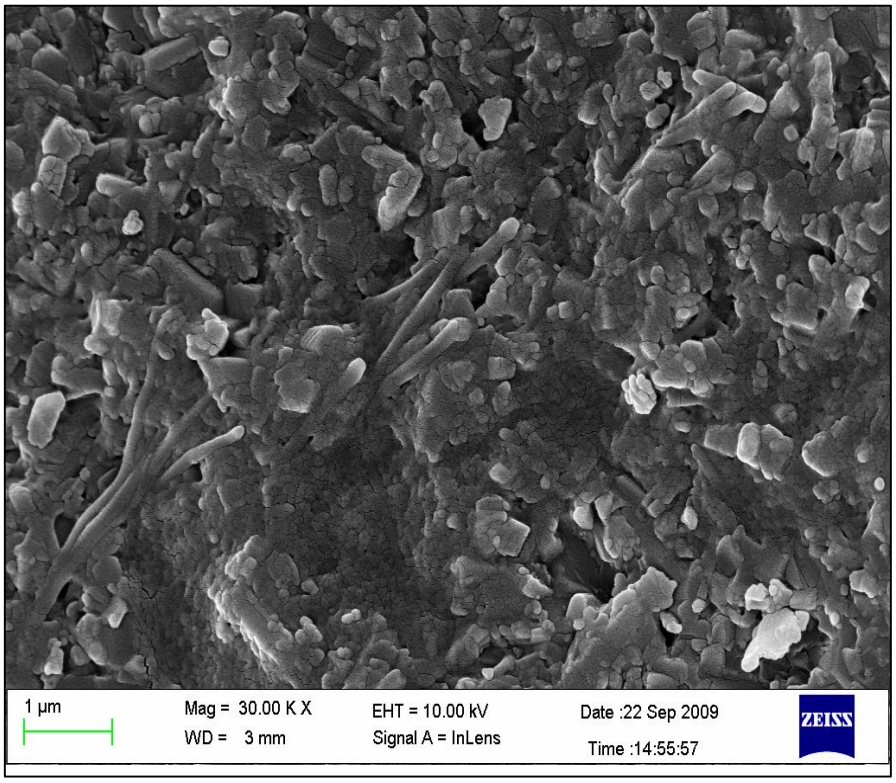

(a)

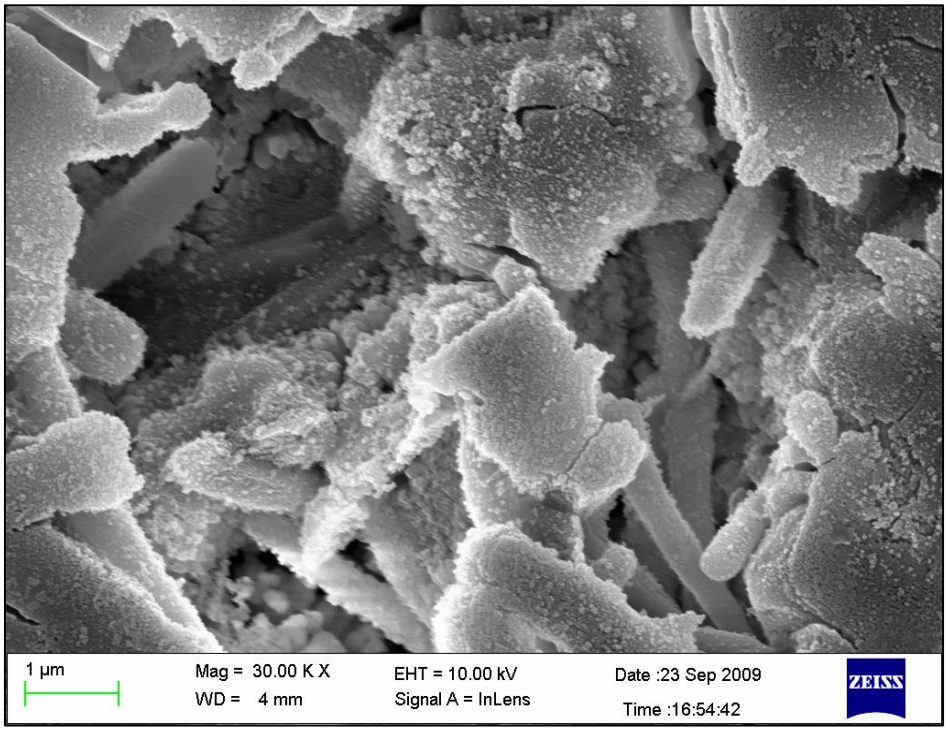
1 µm
Mag = 30.00 K X
WD = 4 mm
EHT = 10.00 kV
Signal A = InLens
Date :23 Sep 2009
Time :16:54:42
ZEISS

(b)

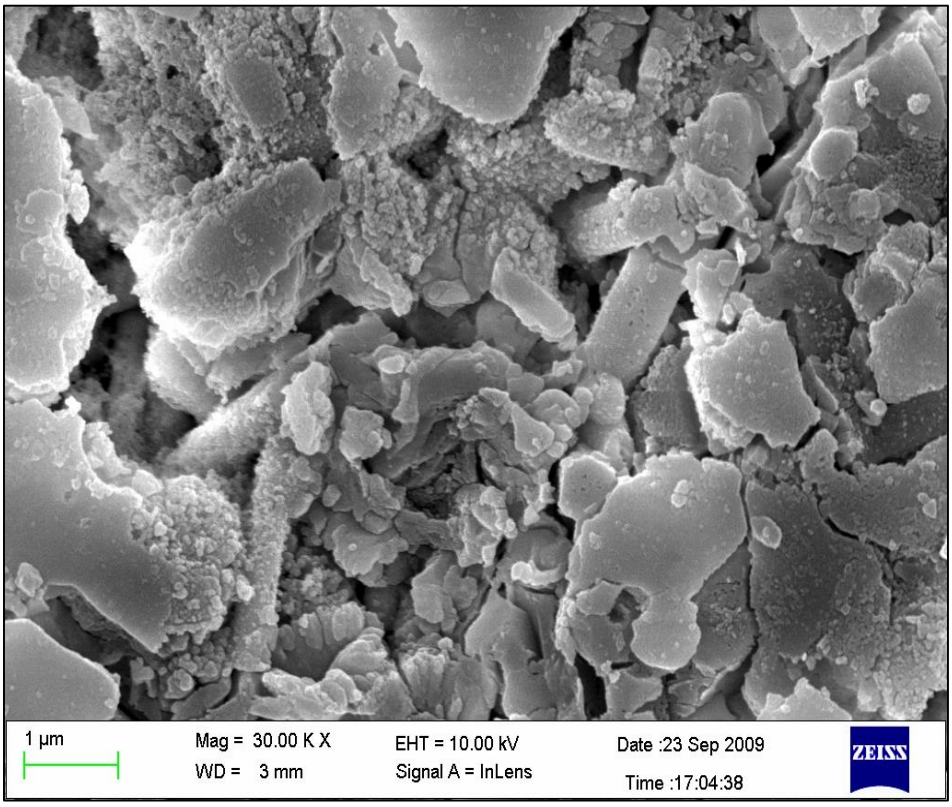
1 µm
Mag = 30.00 K X
WD = 3 mm
EHT = 10.00 kV
Signal A = InLens
Date :23 Sep 2009
Time :17:04:38
ZEISS

(c)

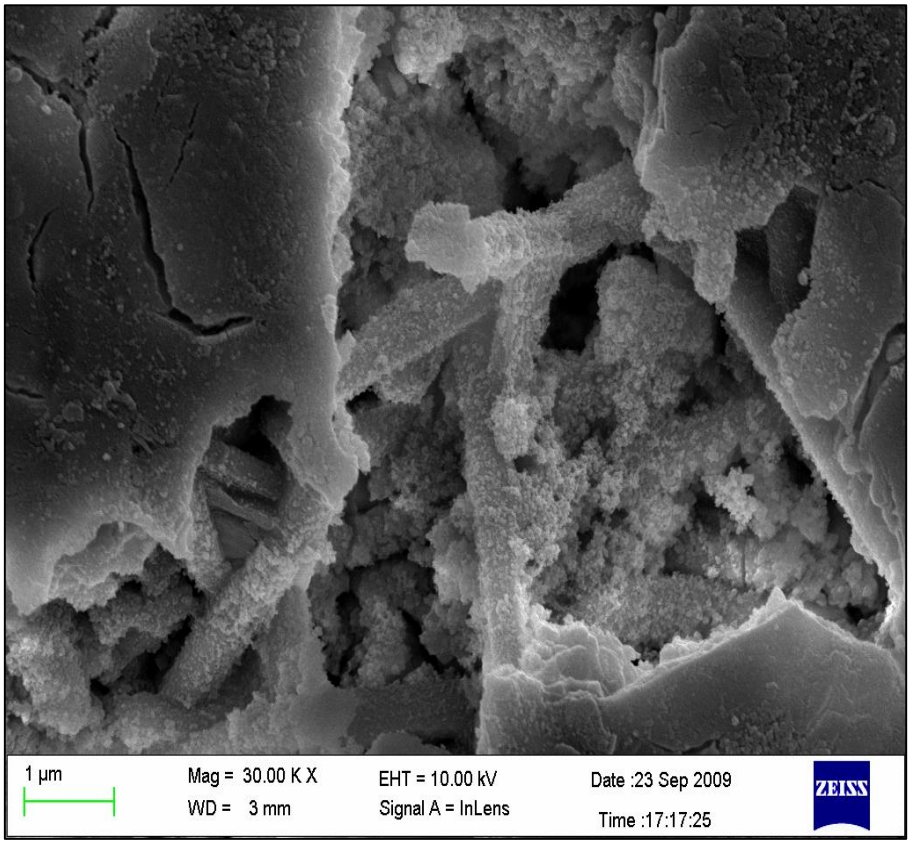

(d)

Figure 49:a) Fractured surface of LG26, b) Chemical Etching of LG26Sr2, c) Chemical etching of LG26Sr3 d) Chemical etching of LG26Sr100

Figure 49b to figure 49d shows the chemically etched SEM observation of the LG26Sr2 LG26Sr3 and LG26Sr4. All these samples were etched with 20% HF for 60 sec. This images shows apatite crystals present in the form needle structure. The celsian crystals phases are not clearly visible due the higher concentration of the HF acid. Further optimizing the chemical etching method can clearly show the morphology of the crystals structure present in the samples. EDX analysis was carried out on the samples to identify the elemental composition. The stoichiometric ratio of the EDX results is closely matched with the starting compositions. Although there were, no quantitative analysis had been performed in order to obtain percentage crystallization.

3.2.5 Summery

Comparing the results with FCT systems the Dr.Sinter samples shows better properties for glass ceramics but considering the physical factors involved during the Dr. Sinter and FCT system obtained results are still much better than the conventional sintering process. The glass ceramics produced using these techniques are of different in sizes when compared with FCT system. The size of the die is much smaller than the size of the used in FCT the volume of the glass powder used is 3 g for sintering using Dr.Sinter. Using Dr.Sinter the study of optimising the processing condition for calcium was carried out and these conditions were applied to strontium glasses molar ratio of 25 %, 50 %, 75 % and 100%. From the obtained results the following conclusion can be made

1. The FAST parameters for sintering Ca Containing glass were optimized. This glass mainly crystallize to apatite and mullite phases and the apatite is present in the form of fluorapatite.
2. The reported mechanical properties showed that FAST is a better method to sinter the materials to their full density acquiring high hardness and fracture toughness values. The microstructural study of the fracture surface of the FAST sintered samples indicated fracture resistance of the crystals formed during sintering.
3. Optimized FAST parameters of the Ca base glass were applied to the Sr substituted glass compositions. It was clearly indicated that the fluorapatite phase was replaced by a mixed Strontium and Fluorine apatite phase and both mullite and celsian phases were present in the 50% and 75% Sr containing glasses. However, in the 100% Sr glass ceramic Sr apatite was fully formed and the mullite was replaced by a Sr celsian phase.
4. The reported mechanical properties and the microstructure of FAST sintered Sr substituted glasses were not as high as the base Ca glass ceramic. This may be the effect of

the mixed cation phases formed and further optimization of FAST parameters is needed to obtain glass ceramics with better properties.

3.3 Results and discussion of honeycomb extrusion process

3.3.1 Benbow/Bridgwater model fit in waste glass paste

Figure 50 and Figure 51 shows the compressive load vs compressive extension curve for the paste 1 and paste 2. Paste 1 shows the instability due the liquid phase being pushed to the surface as the pressure raises which lubricates the walls but as flow relives this pressure and paste leaves the die the remaining liquid is drawn back into the bulk and pressure raises again. This process is repeated over and over again and it is called slick slip behaviour. This may be due the phase migration. The phase migration occurs when the binder system leaks through the powder particles when pressure is applied [154]. Paste 2 shows the stable flow behaviour. All these paste were mixed under the same condition using the Z-blade for 1 hr. Paste 1 is completely unstable due to the binder leaking and paste becomes dry with increasing L/D as pressure rises and makes the extrusion increasingly difficult. During the water absorption test of this waste glass the drying of water content was noticed in the glass powder over a period of time. This might be due to composition of the waste glass. This drying of paste was clearly noticed in the case of paste 1. The extrusion profile would be expected to follow the trend that increasing extrudate velocity increase pressure. In the case of paste 1 at low velocity the pressure remains high when extruded and normal behaviour was exhibited by paste 2.

The presented pressure profile in the Figure 50 and Figure 51 can be divided into 3 regions [155]

1. Compaction
2. Transient flow
3. Steady state of flow

In the compaction region of the extrusion process the air trapped inside the paste is expelled by rapid increase in applied pressure. In the transient region the optimal flow pattern develops. After the transient period steady state occurs were the flow of paste continues at a given

velocity at constant pressure. If there is an inhomogeneity in the paste it can be clearly seen in this region with spikes and pits in the pressure (force) trace.

The determination of average load at each velocity was not possible at different ram speed due to inhomogeneity. Paste 1 is too solid like instead of being plastically deformable by applied pressure. Paste 2 shows steady flow during applied pressure. Due to this reason the organic binder was used in the subsequent paste formulations. The obtained pressure values for paste 1 were not accurate so further paste characterisation was not undertaken.

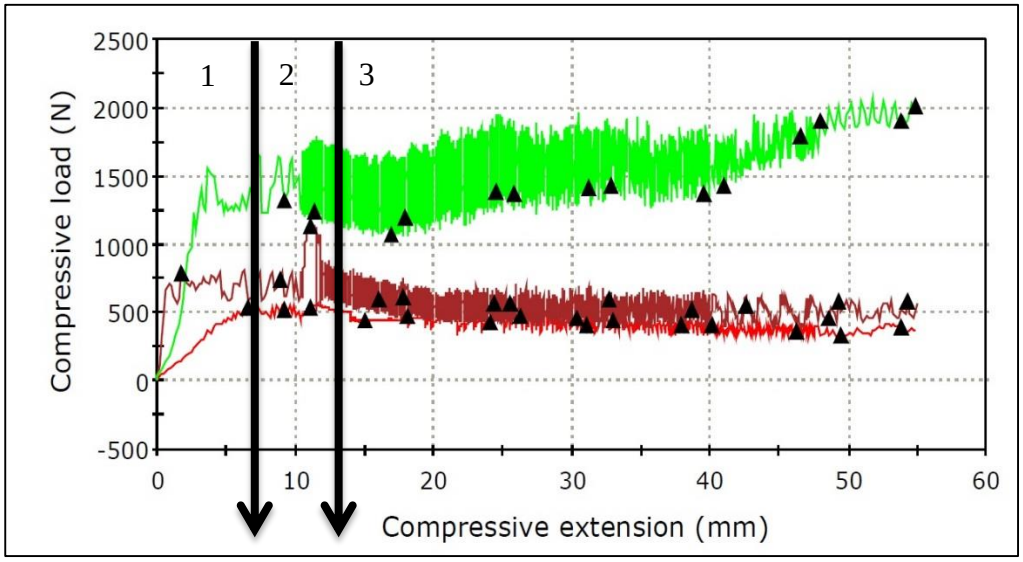

Figure 50: Extrusion load in relation to binder viscosity for Paste 1 with 1 as Compaction, 2 as Transient flow and 3 as steady state of flow**.**

Figure 52 shows the difference in extrusion pressure in relation to length of the die for the Paste 2. Figure 53 shows the comparison of the pressure between calculated Benbow/Bridgwater curve and experimental data at various ram speeds.

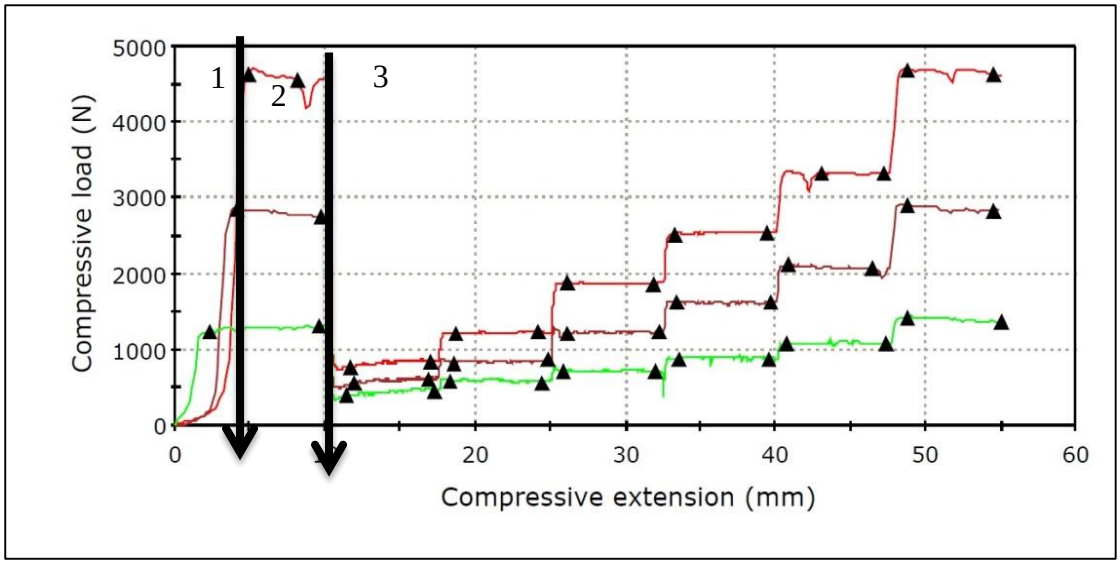

Figure 51: Extrusion load in relation to binder viscosity for Paste 2 with 1 as Compaction, 2 as Transient flow and 3 as steady state of flow.

This experimental extrusion pressure was obtained by calculating the average load applied at each velocity. The obtained values are listed in Table 33 along with the predicted pressure using the equation 15 of Benbow/Bridgwater model and Table 34 shows the calculated parameters of Benbow/Bridgwater for paste 2. In this paste $\sigma_{0,}$ and τ_0 appear to best represented by 0. The Benbow/Bridgwater model assumes the flow of paste to be plug flow with a slip layer at the wall. The value of $\sigma_{0,}$ and τ_0 0 may actually suggest that the model assumption is not maintained but using the other models such as Mooney it would be possible to calculate the properties of slip to no slip at the wall [156]. This was not carried out since the scope of the project is to develop a scaffold.

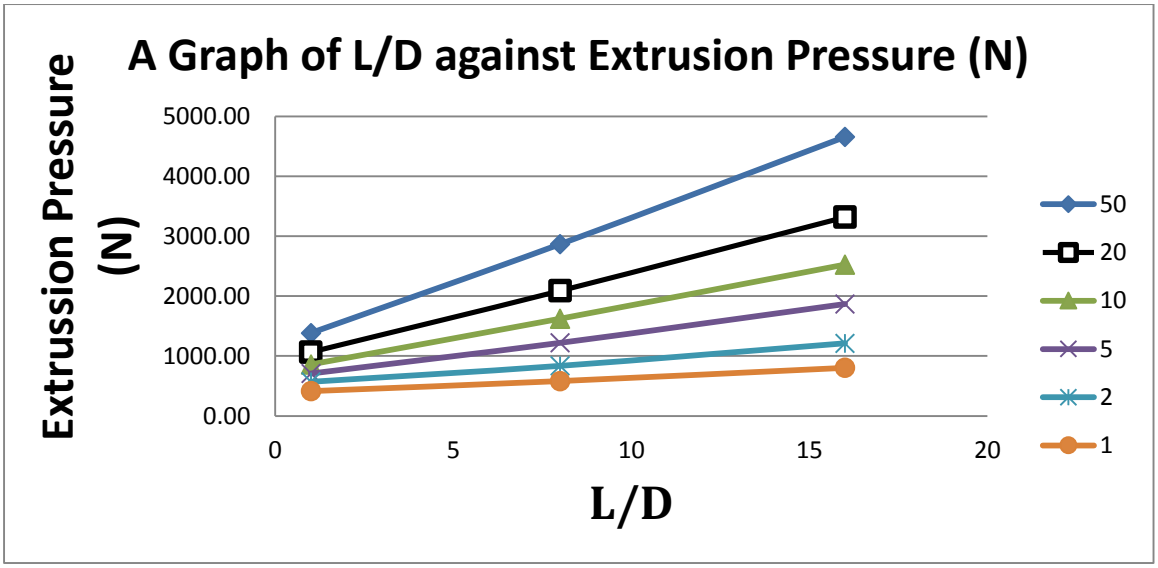

Figure 52: Paste 2 L/D against extrusion Pressure

Table 33: Experimental and predicted pressure of Paste 2 at each velocity

Experimental Pressure (N)				**Predicted Pressure (N)**		
	L/D			**L/D**		
V (mm/min)	**16**	**8**	**1**	**16**	**8**	**1**
50	4656	2867	1384	5057	3108	1403
20	3317	2088	1065	3275	2090	1054
10	2526	1623	860	2377	1564	852
5	1868	1220	708	1739	1181	692
2	1213	836	570	1165	825	528
1	803	582	414	869	636	432

Table 34: Benbow/Bridgewater/Bridgewater paste parameters for Paste 2

Name	**σ_0 (MPa)**	**α_1 (MPa sm)$^{-1}$**	**m**	**τ_0 (MPa)**	**β_1 (MPa sm^{-1})**	**n**
Paste 2	0	1.147	0.27	0	0.555	0.543

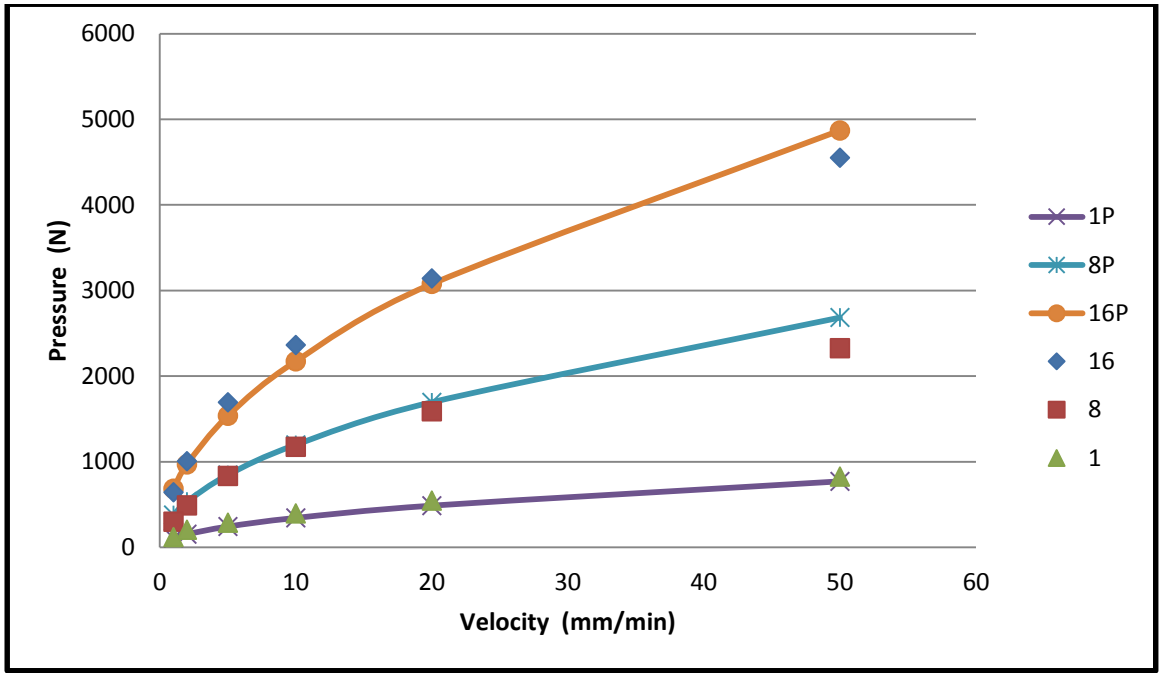

Figure 53: Benbow/Bridgwater model fit with experimental pressure at different velocity of Paste 2

Table 35 shows the experimental and predicted pressure of the Paste 3. In this paste the binder content was reduced by 3% from the actual water absorption test results. Figure 54 shows the comparison of predicated pressure with the actual pressure obtained through extrusion. Table 36 shows the calculated values of paste parameters used in Benbow/Bridgwater equation 15. In paste 3 due to the binder content being reduced to 3%, σ_o raises when compared to paste 2. The rest of the parameters increased other than n which decreased when compared to paste 2 and τ_0 remains 0. This paste shows some yield stress at the die entry region. This due to increase in the powder content of the paste, but the τ_0 remains 0 shows the model assumes the absence of wall shear stress of the Paste 3 at die land. The increased value of the parameter is due to the increasing the solid loading by 3 wt%.

Table 35: Experimental and predicted pressure of Paste 3 at each velocity

Experimental Pressure (N)				**Predicted Pressure (N)**		
	L/D			**L/D**		
V (mm/min)	**16**	**8**	**1**	**16**	**8**	**1**
50	8399	5396	2361	6100	3828	1839
20	6044	3781	1832	4611	2947	1490
10	4784	2958	1518	3504	2285	1218
5	3767	2365	1284	2462	1654	948
2	2641	1551	1048	1904	1312	794
1	1814	1149	831	8887	5458	2457

Table 36: Benbow/ Bridgwater paste parameters for Paste 3

Name	**σ_0 (MPa)**	**α_1 (MPa sm)$^{-1}$**	**m**	**τ_0 (MPa)**	**β_1 (MPa sm^{-1})**	**n**
Paste 3	0.109	2.1246	0.3343	0	0.7499	0.4492

The calculated and predict values of Paste 2 and Paste 3 shows little evidence phase migration when compared with Paste 1. The curve fit obtained for predicted date was in good arrangement with experimental curve, which is normal since this predicted values are calculated using the experimental values. The yield stress at the die entry region of the paste is increased with reduced liquid content which was expected due to the increase in the powder content. The applied pressure for the Paste 2 and Paste 3 is also higher when compared with the Paste 1 which is also expected due to increase in the powder content. The wall shear stress remains 0 even when increasing in the power content in binder which suggest the presence of a low viscosity fluid at the wall giving raise to minimal resistance to plug flow. Other models could be considered to for understanding the wall slip conditions of the paste. The Paste 2 and Paste 3 are plastic allowing shape formation under applied pressure when compared with Paste 1.

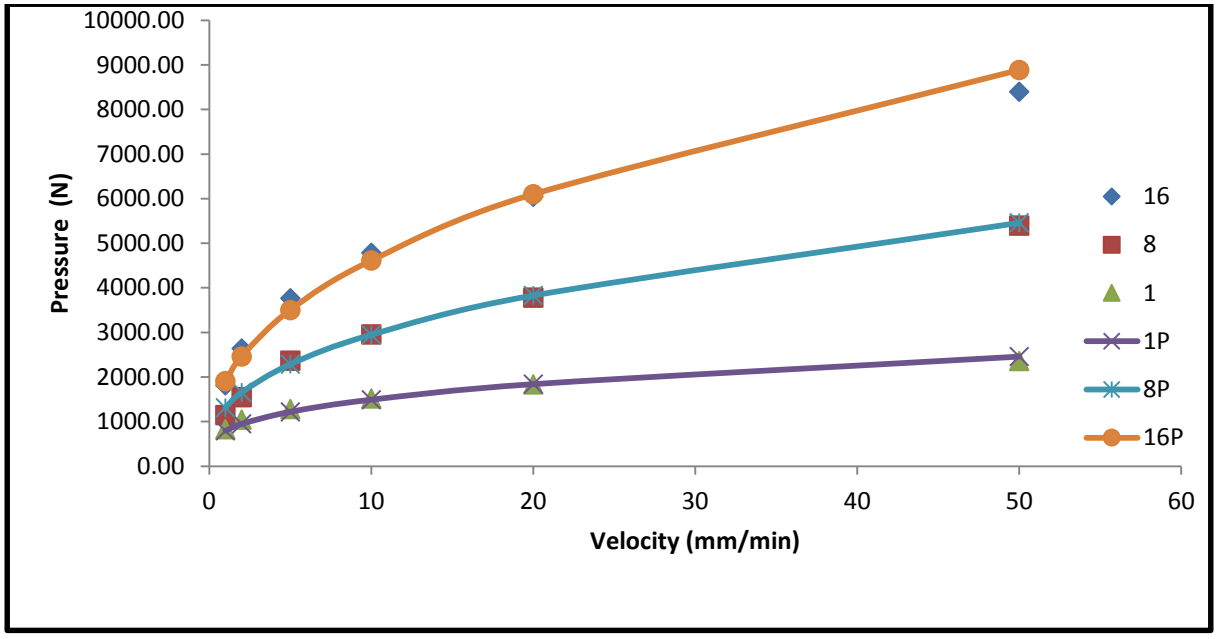

Figure 54: Benbow /Bridgwater model fit with experimental pressure at different velocity of Paste 3

3.3.2 Benbow/Bridgwater Model Fit in LG26 and LG26Mg

Table 37: Benbow/Bridgwater paste parameters for Paste 4

Name	σ_0 (MPa)	α_1 (MPa sm)$^{-1}$	m	τ_0 (MPa)	β_1 (MPa sm^{-1})	n
Paste 4	0	7.643	0.707	0	2.271	0.589

Table 38 shows the experimental and predicted pressure difference of the experimental glass of LG26 Paste 4. In this paste formulation 17 wt% of organic binder was used based on water absorption test. This paste was formed by mixing the experimental glass LG26. The experimental pressure and the predicted pressure were shown in the Figure 55. Table 37 shows the Benbow/Bridgwater parameters used to calculate the predicted pressure of the paste. In this paste σ_o yield stress at the die entry and the wall shear τ_0 remains 0 which is similar to the paste 2. The value n and m which is velocity exponent of die land is also increased when compared with the paste 2 and paste 3.

Table 38: Experimental and predicted pressure of Paste 4 at each velocity

Experimental Results (N)				Predicted Pressure (N)		
	L/D			L/D		
V (mm/min)	16	8	1	16	8	1
50	15192	8248	2892	16264	9260	3132
20	9646	5237	1789	9346	5263	1691
10	6525	3532	1212	6151	3437	1062
5	4306	2333	794	4051	2247	668
2	2401	1273	417	2335	1283	363
1	1469	707	231	1540	841	229

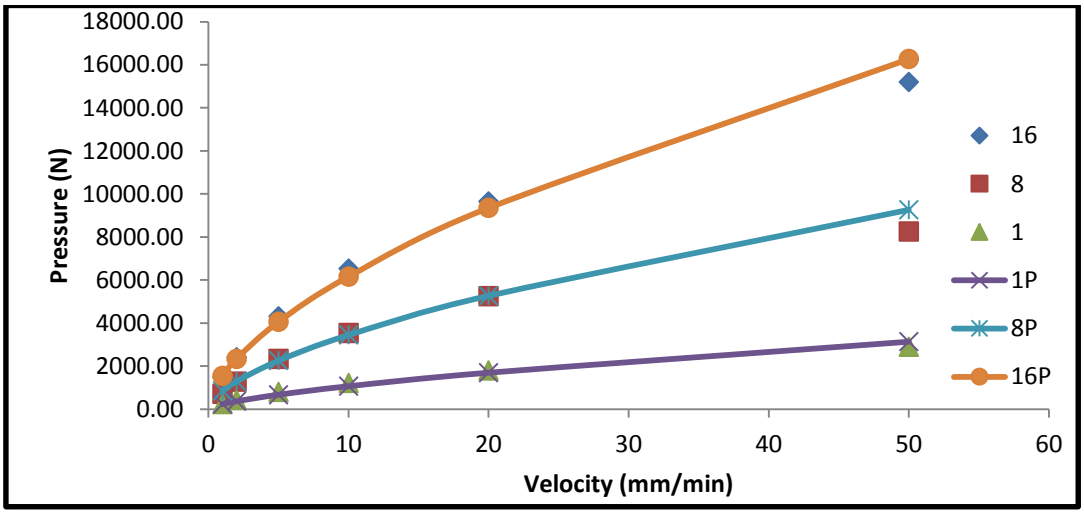

Figure 55: Benbow /Bridgwater model fit with experimental pressure at different velocity of Paste 4

Table 39 shows the paste parameters used to calculate the experimental pressure. Table 40 shows the difference in the pressure between the experimental and calculated values and Figure 56 shows the difference between the experimental pressure vs calculated pressure. In this paste the binder content was reduced by 2 wt% compared with Paste 4. LG26 glass was used in the paste. Even reducing the binder content paste 5 did not show any initial bulk yield stress or initial die wall shear stress at the die entry or die land region of the Benbow/Bridgwater model. In this paste the required pressure for extrusion is increased which is due to increase in the

powder content. This shows that the further reduction in the binder content is needed to form a paste that will retain its shape after extrusion.

Table 39: Benbow/ Bridgwater paste parameters for Paste 5

Name	σ_0 (MPa)	α_1 (MPa sm)$^{-1}$	m	τ_0 (MPa)	β_1 (MPa sm^{-1})	n
Paste 5	0	6.632	0.561	0	2.688	0.584

Table 40: Experimental and predicted pressure of Paste 5 at each velocity

Experimental Pressure (N)				**Theoretical Pressure (N)**		
	L/D			**L/D**		
V (mm/min)	**16**	**8**	**1**	**16**	**8**	**1**
50	18567	10244	3845	19769	11362	4005
20	12003	6718	2496	11614	6690	2382
10	8146	4641	1745	7766	4482	1608
5	5506	3140	1204	5194	3003	1085
2	3083	1741	681	3051	1768	646
1	1933	1079	412	2041	1185	436

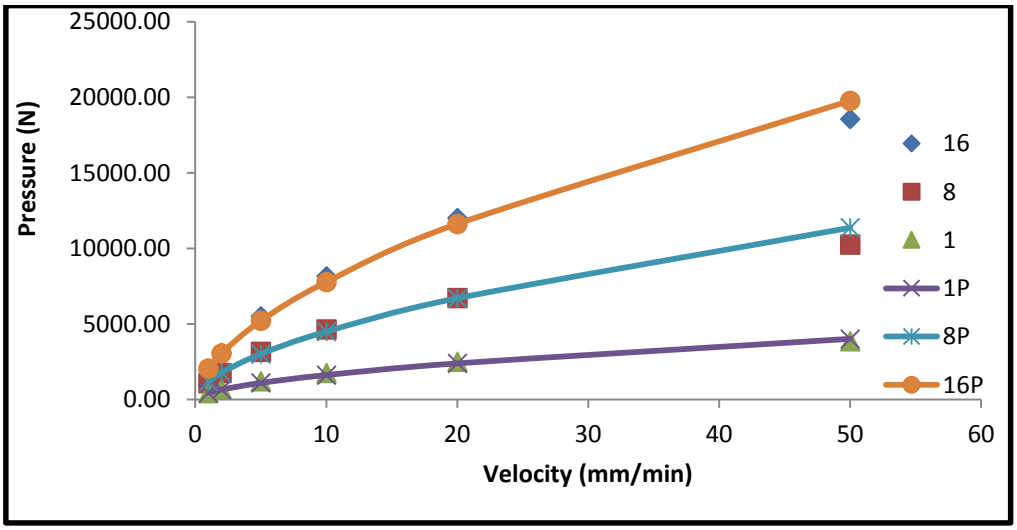

Figure 56: Benbow/Bridgwater model fit with experimental pressure at different velocity of Paste 5

Table 41 shows the calculated value of the Benbow/Bridgwater equation from the raw data for paste 6. In this experiment LG26Mg glass was used. The binder content was reduced by 2wt% from the water absorption test. This paste with the different experimental glass also shows no yield stress at die entry region. Table 42 shows the experimental values along with the calculated pressure using Benbow/Bridgwater model of extrusion at various speeds with difference in L/D values. The Figure 57 shows the difference in the pressure generated between experimental and calculated of different L/D. The calculated values are in good arrangements when compared with the experimental values. In general when comparing the results of all these pastes the yield stress and the wall shear were near zero. This shows the absence of model plug flow assumption of the paste in the die land and dies entry. All the above binder formulation had an organic binder base.

Table 41: Benbow/ Bridgwater paste parameters for Paste 6

Name	**σ_0 (MPa)**	**α_1 (MPa sM)$^{-1}$**	**m**	**τ_0 (MPa)**	**β_1 (MPa sm^{-1})**	**n**
Paste 2	0	4.178	0.478	0	2.228	0.598

Table 42: Experimental and predicted pressure of Paste 6 at each velocity

Experimental Results (N)				**Theoretical Pressure(N)**		
	L/D			**L/D**		
V (mm/min)	**16**	**8**	**1**	**16**	**8**	**1**
50	14508	8442	2930	15750	9051	3189
20	9356	5547	1951	9263	5390	2001
10	6624	3875	1466	6207	3648	1409
5	4406	2677	1057	4163	2472	993
2	2475	1563	632	2459	1482	627
1	1502	963	373	1653	1008	443

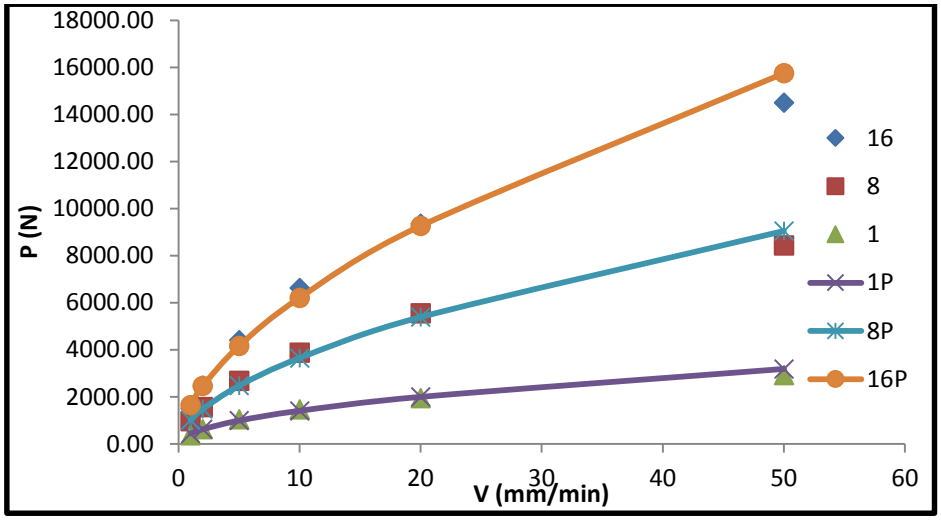

Figure 57: Benbow /Bridgwater model fit with experimental pressure at different velocity of Paste 5

3.3.3 Honeycomb pressure drop Model Fit

The honeycomb pressure drop was calculated using a set of equation developed by S.Blackburn and H.Böhm[147]. The paste used for the honeycomb extrusion was Paste 2 for the waste glass, Paste 5 of LG26 and Paste 6 for LG26Mg. Table 44 show the percentage difference of predicted pressure drop compared to the experimental value. Table 43 shows the experimental pressure of the honeycomb extrusion. The honeycomb extrusion was performed at three different velocities. The paste parameter obtained using the Benbow/Bridgwater equations were inserted into the S.Blackburn and H.Böhm equation to calculate the pressure drop [147]. It can be seen from the table 44 that the calculated pressure drop of the glass paste are not in good agreement with experimental values. The difference between the predicted values are relatively high in all the paste which shows that the models does not fit for this glass paste. The suggested model follows the correct trend but there is significant error in the predicted pressure drop. The failure of the model is in moving from the simple rod extrusion geometry to the honeycomb and also the paste does not show any yield stress during extrusion. The paste in the honeycomb is generally going a lot slower were difference comes due to difficulty of fitting at

very low extrusion speeds and so the pressure drop predicted will possibly be in an area of flow where the model is not fitting the data with much reliability. It brings into question that the model is the right one to be using or the model is in useable when the pastes are poorly understood.

It was found that when σ_o of the paste range from 0.15 to 0.3 MPa a good honeycomb could be extruded but if the value was lower the shape was not retained due to the low yield strength [133]. In the case of all the above glass pastes the value of σ_o was zero and deformation was observed while drying the extrudate. The m values were in range of 0.2 to 0.7 for the above glass paste and they shows a significant difference in the results at the low velocity extrusion. Further higher yield stress value were found in the extrusions where the m values were greater than 0.4 [133]. If the obtained m and n are higher than 0.4 with constant α and β then the decent honeycomb shape can be maintained after extrusion [133].

Table 43: Experimental pressure of honeycomb extrusion

Paste Type	**Glass**	**Velocity (mm/sec)**	**Experimental Pressure MPa**
Paste 3	Waste glass	0.00033	2.05
		0.00016	2.03
		0.00008	1.60
Paste 5	LG26	0.00033	5.35
		0.00016	4.56
		0.00008	3.73
Paste 6	LG26Mg	0.00033	5.37
		0.00016	5.51
		0.00008	4.09

Table 44: Percentage of pressure drop of honeycomb extrusion

Glass	Paste type	Velocity (mm/sec)	Percentage of predicted pressure drop
Waste glass	Paste 3	0.00033	63.49
		0.00016	47.30
		0.00008	45.79
LG26	Paste 5	0.00033	50.28
		0.00016	38.17
		0.00008	31.59
LG26Mg	Paste 6	0.00033	52.64
		0.00016	33.94
		0.00008	31.51

3.3.4 X-Ray Diffraction of Honeycomb extrudate of LG26 and LG26Mg

Figure 58 shows the X-ray diffraction pattern of the honeycomb shaped LG26 and LG26Mg sintered using a conventional furnace. These glasses were sintered at heating rate of 5^{o}C with the nucleation hold at 700^{o}C for 2 hr and final crystallisation temperature of 1100^{o}C for 2 hr. XRD patterns of these glasses show the presence of crystalline peaks. The crystal peaks formed after sintering LG26 are fluorapatite and mullite as the major phases. In the case of LG26Mg the crystals formed were mullite and wagnerite. This glass does not show any amorphous region at lower 2θ angles. This shows the glass is completely crystalline. Only major peaks were identifed and marked in the Figure 58. During the extrusion process these glass were mixed with the organic binder which was burnt out during the sintering process and this organic binder does not show any kind of reaction with the glass composition which can be clearly seen in the XRD pattern

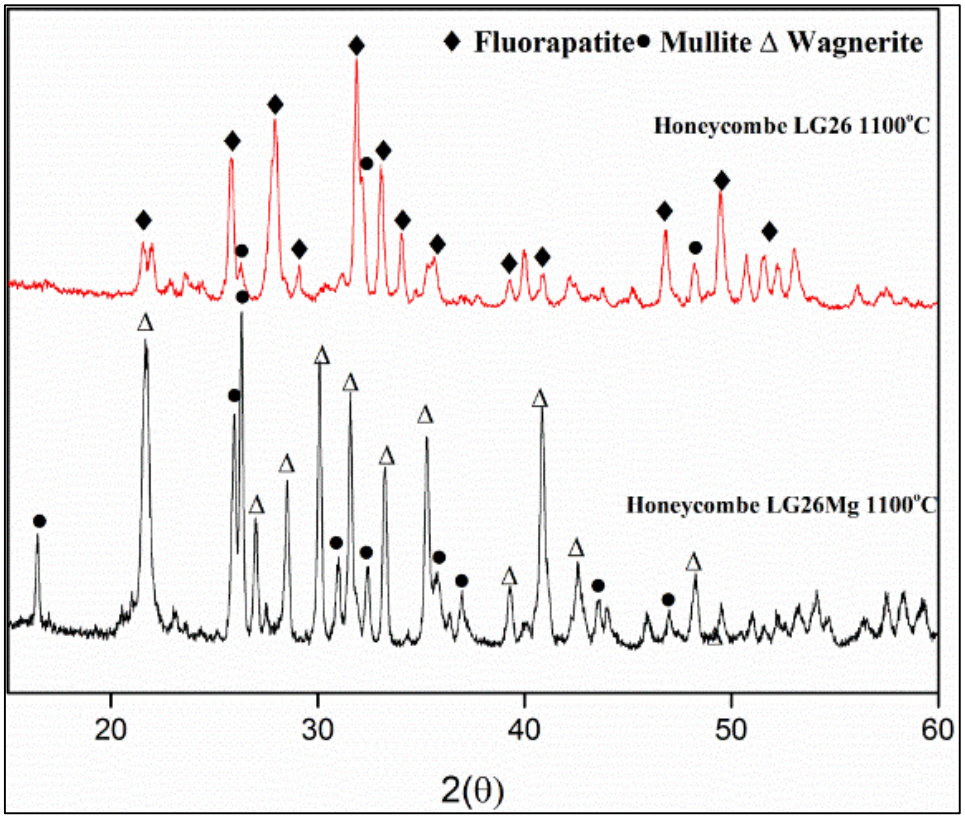

Figure 58: X-ray diffraction of honeycomb extrudate of LG26 and LG26Mg

3.3.5 Microstructure

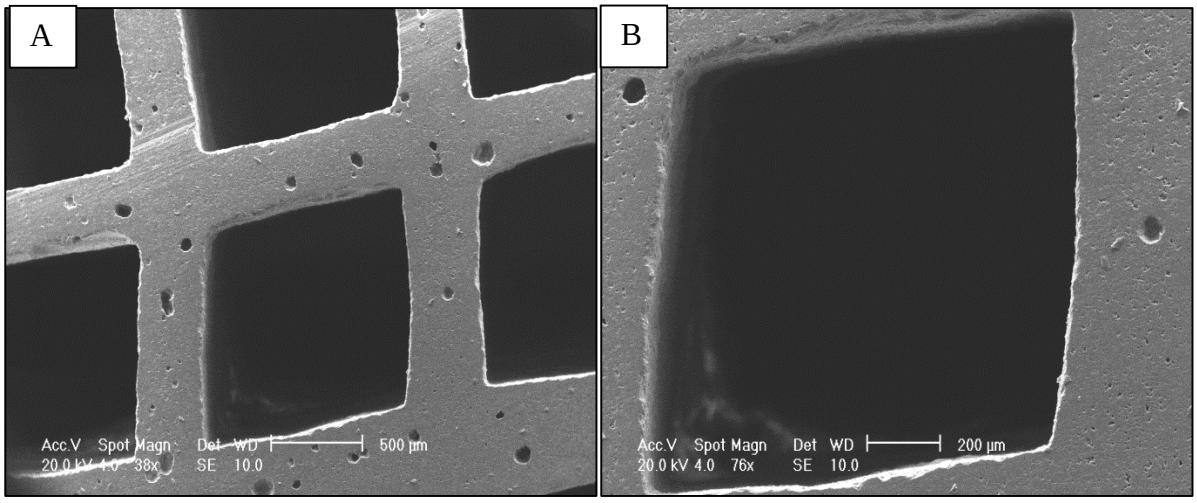

Figure 59: a) Microstructure of honeycomb cell of LG26Mg sintered, b) Deformation of honeycomb cell in LG26Mg

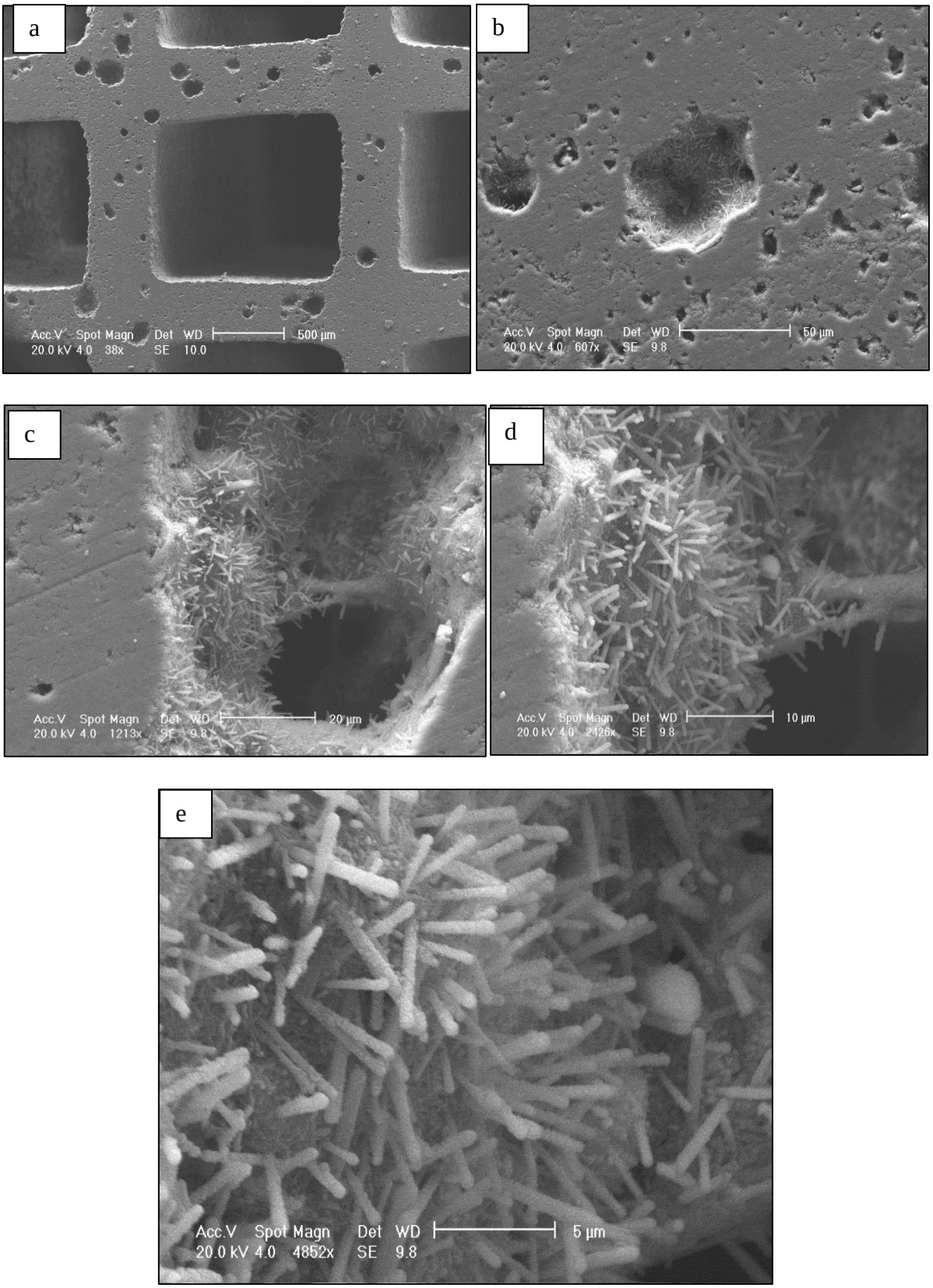

Figure 60: Microstructure of LG26 honeycomb extrudate sintered at 1100ºC

Figure 59 shows the microstructure of honeycomb shape LG26Mg glass sintered at 1100^{o}C. This glass ceramics shows slight deformation on the honeycomb cells. This was due to the sintering and the removal of binder from glass during the sintering process. The presence of binder in this glass was higher when compared with the LG26, which makes this glass not able to retain the extrudate shape. Figure 59 shows the microstructure of the honeycomb extrudate of LG26 glass crystallised at 1100^{o}C. The honeycomb structure did not show any deformation after sintering. Figure 59 shows The surface of honeycomb structure with the presence of pores which was formed due to air entrapment. In these pores the crystal structure of fluorapatite can be seen by the presence of needle like structure which are well known for this glass system [43]. This needle like structure of fluorapatite interlocks with the mullite crystals which intern helps in improving the mechanical properties of this glass ceramic.

3.3.6 Summery

In this work, investigation of the processing of aluminosilicate glass using the extrusion technique were undertaken. The extrusion rheology of the glass powder were optimised using the waste glass and experimental glass powder of LG26 and LG26Mg. Based on the results the following conclusion can be made:

1. The waste glass when mixed with binder of hydroxypropyl methylcellulose did not form an extrudable paste. The required pressure at low velocity was high due to the binder leaking through the pores between the glass powder
2. The paste formed of using the organic binder showed that shaping of honeycomb can be achieved in these glasses.
3. The Benbow/Bridgwater model used for predicting the pressure drop correlates will with the experimental data for these glass for simple extrusion of rods.
4. The honeycomb pressure drop was calculated using the equation developed by S.Blackburn and H.Böhm and shown to obtain results which does not fits of the experimental results. This was attributed to the model not representing the flow behaviour at low velocities and the significant increase in complexity of the die.
5. The honeycomb structure was crystallised successfully without change in any of crystal phases on the experimental glasses
6. The microstructure of the honeycomb shows the formation of needle like fluorapatite crystal in the LG26 on the surface pores and no deformation was observed but the LG26Mg shows the slight deformation due to sintering and removal of binders.
7. Further optimisation on rheology of this LG26Mg paste will help in retain the shape of the honeycomb structure

CHAPTER IV: CONCLUSIONS AND FUTURE WORK

4.1 Conclusions

Fluoro-alumino silicate glasses with the substitution of cations of Ca, Sr and Mg were studied. This work mainly focused on the processing technique of these glass ceramics, since most of the literature is focused on the understanding of the structure and mechanism of crystallisation of these glass ceramics. The literature results suggested that these glass ceramics have the potential to act like bioactive materials. Only some work in the literature has focused on the processing technique of these glass ceramics for medical applications. In this work two different processing techniques for the crystallisation and an alternative way of fabricating tissue engineering scaffolds were explored.

The FAST sintering was used to crystallise all the glasses reported in this work. FAST is a new technique, which has been in practice recently for producing dense ceramics for biomedical applications. The advantages of FAST are short sintering time, high heating rate and uniaxial pressure. This helps in producing dense materials fast with much more control over grain growth. All the glass compositions investigated in this work were crystallised using FAST. The obtained results of FAST sintering process are better when compared to conventional sintering techniques. The mechanical properties of the FAST processed samples were significantly improved. The crystal phases of the FAST sintered glass ceramics were similar to conventional sintering.

The second processing technique used in this work is extrusion which is a traditional process to shape ceramics. In this work the paste parameters and the extrusion rheology as paste passed through a honeycomb die were studied. The honeycomb structure is normally used in the automobile industry to make catalyst templates. In this work the focus was on producing a honeycomb structure that could potentially find application as a tissue engineering scaffold. The obtained honeycomb structure has arrays of channels and micro pores on the side walls.

This kind of pore structure can be used in orthopaedics for regeneration of diseased bone. The honeycomb structure is mechanically much stronger than the sponge replication method of the scaffold processing method.

4.2 Future work

In future, a detailed work should be carried out on the processing of the glasses for various biomedical applications. FAST showed a good combination of properties in these materials but the mechanism of FAST sintering and the crystallisation of these glasses during FAST should be studied in detail. In the extrusion processing technique, only the paste rheology and the crystallisation of the honeycomb structure were studied. Therefore, only basic understanding on the above processing techniques of these glasses was provided in this work and the following future work can be suggested:

1. Crystallography results suggested the presence of crystalline phases but a detailed volume fraction of phases by Rietveld analysis was not presented.
2. Only surface mechanical properties were reported in this work due to the limited number of sintered samples. A complete mechanical testing of the FAST processed glass ceramics will be helpful in understanding the effect of the process on the mechanical properties of the glass ceramics.
3. Further investigation using more sensitive techniques such as solid state MAS-NMR should be carried out in order to develop a detailed understanding of the evolution of the glass ceramics microstructure during crystallisation using FAST.
4. The obtained honeycomb structure of glass ceramics can be used as scaffold but the biological properties and mechanical properties need to be evaluated so that this scaffold can be used for medical applications.

Reference

1. Wise, D.L., *Encyclopedic handbook of biomaterials and bioengineering*. 1995, New York: Marcel Dekker. xv, p855-1795.
2. Jandt, K.D., *Focus on Materials in Biomaterials Science.* Advanced Engineering Materials, 2011. **13**(12): p. B431-B431.
3. Silverthorne, K. and U. Cardiff, *Development of 'smart' biomaterials for tissue repair*. 2004, [Great Britain]: Cardiff University. 1 online resource.
4. Wise, D.L., *Encyclopedic handbook of biomaterials and bioengineering*. 1995, New York: Marcel Dekker. xv,851p.
5. Kokubo, T., *Bioceramics and their clinical applications [electronic resource]*. 2008, Cambridge: Woodhead Publishing Ltd. 784 p.
6. Wong, J.Y. and J.D. Bronzino, *Biomaterials*. 2007, Boca Raton: CRC Press. 1 v. (various pagings).
7. Hoffman, A.S., *Synthetic-Polymer Biomaterials.* Abstracts of Papers of the American Chemical Society, 1983. **185**(Mar): p. 6-Orpl.
8. Hanna, M.A. and N.N. Mohsenin, *Composite Biomaterials as Structural-Materials for Packaging.* Transactions of the Asae, 1976. **19**(2): p. 390-395.
9. Sedel, L. and C. Rey, *Bioceramics*. 1997, Oxford: Pergamon. xxiii,598p.
10. Kokubo, T., T. Nakamura, and F. Miyaji, *Bioceramics*. 1996: Pergamon.
11. Jones, D.W., *Ceramic biomaterials.* Advanced Ceramic Materials, 1996. **122-1**: p. 345-383.
12. Dubok, V.A., *Bioceramics - Yesterday, today, tomorrow.* Powder Metallurgy and Metal Ceramics, 2000. **39**(7-8): p. 381-394.
13. Rusin, R.P., G.S. Fischman, and S. American Ceramic, *Bioceramics : materials and applications*. 1995: ACS.
14. *Bioceramics: Engineering in medicine*. Biomedical materials symposium. 1972, New York: Interscience Publishers. xi, 484 p.
15. Park, J., *Bioceramics [electronic resource] : Properties, Characterizations, and Applications*. 2009, New York, NY: Springer-Verlag New York. digital.
16. Black, J., G.W. Hastings, and Knovel, *Handbook of biomaterial properties [electronic resource]*. 1st ed. 1998, London ; New York: Chapman & Hall. xxvi, 590 p.
17. American Ceramic, S., *Progress in bioceramics*. Progress in ceramic technology series book. 2004, Westerville, Ohio: The American Ceramic Society. ix, 342 p.
18. Narayan, R., et al., *Biomaterials science : processing, properties, and applications*. Ceramic transactions. 2011, Hoboken, N.J.: [Westerville. vii, 196 p.
19. Gittings, J.P. and B. University of, *Fabrication and properties of novel open porous calcium phosphate bioceramics [electronic resource]*. 2005, Bath: University of Bath.
20. International Symposium on Ceramics in, M., G. Daculsi, and P. Layrolle, *Bioceramics : Volume 20 : proceedings of the 20th International Symposium on Ceramics in Medicine, the Annual Meeting of the International Society for Ceramics in Medicine (ISCM), Nantes, France, 24-26 October 2007*. Key engineering materials, v. 361-3631013-9826. 2008, Stafa-Zuerich ; UK: Trans Tech Publications.
21. Fotheringham, A., *Silicate containing calcium phosphate bioceramics*. Aberdeen University: Thesis, M.Sc. 2006. 87 leaves.
22. Hench, L.L., ed. *An Introduction to bioceramics*. Second edition / editor, Larry L. Hench, University of Florida, USA. ed. 2013, World Scientific,Imperial College Press: Hackensack, New Jersey,London. xix, 600 pages.

23. Kokubo, T., M. Institute of Materials, and Mining, *Bioceramics and their clinical applications*. Woodhead Publishing in materials. 2008, Cambridge: Woodhead Publishing Ltd. xxiv, 760 p.
24. Kossler, W., J. Fuchs, and I. ebrary, *Bioceramics : properties, preparation and applications*. 2009, New York: Nova Biomedical Books. xi, 299 p.
25. Šesták, J., J.i.J. Mareš, and P. Hubík, *Glassy, amorphous and nano-crystalline materials : thermal physics, analysis, structure and properties*. Hot topics in thermal analysis and calorimetry. 2010, Dordrecht ; London: Springer. xvii, 380 p.
26. Benbow, J. and J. Bridgwater, *Paste flow and extrusion*. 1993: Clarendon Press Oxford.
27. Shelby, J.E. and C. Royal Society of, *Introduction to glass science and technology [electronic resource]*. 2nd ed. 2005, Cambridge: Royal Society of Chemistry. 1 online resource (291 p.).
28. Society of Glass Technology. Structure of Amorphous Materials Special Interest, G. and T. Society of Glass, *Structure of amorphous materials*. 2004: Society of Glass Technology.
29. Uhlmann, D.R. and N.J. Kreidl, *Glass : science and technology*. 1990, Boston: London : Academic Press.
30. Bell, R.J. and P. Dean, *The structure of vitreous silica: Validity of the random network theory.* Philosophical Magazine, 1972. **25**(6): p. 1381-1398.
31. Lowenstein, W., *The distribution of aluminium in the tetrahedral of silicates and aluminates.* American Mineralogist, 1954. **39**: p. 92-96.
32. Thompson, I.D., L.L. Hench, and E. Institution of Mechanical, *Mechanical properties of bioactive glasses, glass-ceramics and composites*. 1998.
33. Stebbins, J.F. and Z. Xu, *NMR evidence for excess non-bridging oxygen in an aluminosilicate glass.* Nature, 1997. **390**(6655): p. 60-62.
34. Shelby, J.E., *Introduction to glass science and technology*. 2nd ed. 2005, Cambridge: Royal Society of Chemistry. xvi, 291 p.
35. Jones, J.R. and A. Clare, *Bio-glasses : an introduction*. 2012, Chichester, West Sussex: Wiley. p.
36. Garcia, A. and C. Durand, *Bioengineering : principles, methodologies and applications*. Biotechnology in agriculture, industry and medicine. 2010, New York: Nova Science Publisher's. xi, 218 p.
37. Hench, L.L., J.R. Jones, and M.B. Fenn, *New materials and technologies for healthcare*. 2012, LondonHackensack, N.J.: Imperial College Press ;Distributed by World Scientific Pub. Co. vi, 511 p.
38. El-Meliegy, E. and R.v. Noort, *Glasses and glass ceramics for medical applications*. 2012, New York: Springer. xxiv, 244 p.
39. Zhang, S., *Effect of zinc substitution on the structure of calcium Fluoro-Alumino-Silicate glasses and glass-ceramics*. 2010, Birmingham: University of Birmingham. 88 p.
40. Hland, W., G.H. Beall, and S. American Ceramic, *Glass-ceramic technology [electronic resource]*. 2nd ed. 2012, Hoboken, N.J.: Wiley. xx, 414 p., [8] p. of plates.
41. Ylanen, H.O., *Bioactive glasses [electronic resource] : Materials, properties and applications*. 2011, Cambridge: Woodhead Publishing Ltd. 288 p.
42. Höland, W., G.H. Beall, and S. American Ceramic, *Glass-ceramic technology*. 2002, Westerville, OH: American Ceramic Society. xix, 372 p.
43. Clifford, A. and R. Hill, *Apatite-mullite glass-ceramics.* Journal of Non-Crystalline Solids, 1996. **196**: p. 346-351.

44. Fathi, H.M., et al., *The influence of CaF2 on the solubility of apatite-mullite glass-ceramic materials.* J Dent Res, 2003. **82**: p. B336-B336.
45. Walsh, J.M., *Evaluation of apatite-mullite glass-ceramics for use in restorative dentistry*. 2001.
46. Wang, F., *Cation substitution in ionomer glasses : effect on glass structure and crystallisation*. 2009, Birmingham: University of Birmingham. iv, 184 p.
47. Stamboulis, A., et al., *A MAS NMR study of the crystallisation process of apatite-mullite glass-ceramics.* Bioceramics, Vol 16, 2004. **254-2**: p. 99-102.
48. Fathi, H., et al., *The influence of calcium fluoride (CaF2) on biaxial flexural strength of apatite-mullite glass-ceramic materials.* Dental Materials, 2005. **21**(9): p. 846-851.
49. Rafferty, A., et al., *Influence of fluorine content in apatite-mullite glass-ceramics.* Journal of the American Ceramic Society, 2000. **83**(11): p. 2833-2838.
50. Hill, R.G., A. Stamboulis, and R.V. Law, *Characterisation of fluorine containing glasses by F-19, Al-27, Si-29 and P-31 MAS-NMR spectroscopy.* Journal of dentistry, 2006. **34**(8): p. 525-532.
51. Stanton, K.T. and R.G. Hill, *Crystallisation in apatite-mullite glass-ceramics as a function of fluorine content.* Journal of Crystal Growth, 2005. **275**(1-2): p. E2061-E2068.
52. O'Donnell, M.D., et al., *Real time neutron diffraction and solid state NMR of high strength apatite-mullite glass ceramic.* Journal of Non-Crystalline Solids, 2010. **356**(44-49): p. 2693-2698.
53. Hill, R. and D. Wood, *Apatite Mullite Glass-Ceramics.* Journal of Materials Science-Materials in Medicine, 1995. **6**(6): p. 311-318.
54. Kokubo, T., et al., *Mechanical-Properties of a New Type of Apatite-Containing Glass Ceramic for Prosthetic Application.* Journal of Materials Science, 1985. **20**(6): p. 2001-2004.
55. O'Flynn, K.P. and K.T. Stanton, *Controlling the Crystallization of Fluorapatite in Apatite-Mullite Glass-Ceramics.* Crystal Growth & Design, 2012. **12**(3): p. 1218-1226.
56. Stamboulis, A., et al., *MAS NMR study of the crystallisation process of apatite-mullite glass ceramics.* Physics and Chemistry of Glasses, 2004. **45**(2): p. 127-133.
57. Freeman, C.O., et al., *Crystallization modifies osteoconductivity in an apatite-mullite glass-ceramic.* Journal of Materials Science-Materials in Medicine, 2003. **14**(11): p. 985-990.
58. Goodridge, R.D., et al., *Biological evaluation of an apatite–mullite glass-ceramic produced via selective laser sintering.* Acta Biomaterialia, 2007. **3**(2): p. 221-231.
59. Hill, R.G., et al., *The influence of strontium substitution in fluorapatite glasses and glass-ceramics.* Journal of Non-Crystalline Solids, 2004. **336**(3): p. 223-229.
60. Oliveira, J.P., et al., *Strontium Is Incorporated in Different Levels into Bones and Teeth of Rats Treated with Strontium Ranelate.* Calcified Tissue International, 2012. **91**(3): p. 186-195.
61. Fredholm, Y.C., et al., *Influence of strontium for calcium substitution in bioactive glasses on degradation, ion release and apatite formation.* Journal of the Royal Society Interface, 2012. **9**(70): p. 880-889.
62. Fujikura, K., et al., *Influence of strontium substitution on structure and crystallisation of Bioglass (R) 45S5.* J Mater Chem, 2012. **22**(15): p. 7395-7402.
63. Zhang, W.B., et al., *Effects of strontium in modified biomaterials.* Acta Biomater, 2011. **7**(2): p. 800-808.
64. Li, J.X., et al., *In vitro biocompatibility study of calcium phosphate glass ceramic scaffolds with different trace element doping.* Materials Science & Engineering C-Materials for Biological Applications, 2012. **32**(2): p. 356-363.

65. Fredholm, Y.C., et al., *Strontium containing bioactive glasses: Glass structure and physical properties.* Journal of Non-Crystalline Solids, 2010. **356**(44-49): p. 2546-2551.
66. O'Donnell, M.D. and R.G. Hill, *Influence of strontium and the importance of glass chemistry and structure when designing bioactive glasses for bone regeneration.* Acta Biomaterialia, 2010. **6**(7): p. 2382-2385.
67. Wong, C.T., et al., *Ultrastructural study of mineralization of a strontium-containing hydroxyapatite (Sr-HA) cement in vivo.* Journal of Biomedical Materials Research Part A, 2004. **70A**(3): p. 428-435.
68. Wong, K.L., et al., *Mechanical properties and in vitro response of strontium-containing hydroxyapatite/polyetheretherketone composites.* Biomaterials, 2009. **30**(23-24): p. 3810-3817.
69. Sabareeswaran, A., et al., *Early osseointegration of a strontium containing glass ceramic in a rabbit model.* Biomaterials, 2013. **34**(37): p. 9278-9286.
70. Bertoni, E., et al., *Nanocrystals of magnesium and fluoride substituted hydroxyapatite.* J Inorg Biochem, 1998. **72**(1-2): p. 29-35.
71. Chaudhry, A.A., et al., *Synthesis and characterisation of magnesium substituted calcium phosphate bioceramic nanoparticles made via continuous hydrothermal flow synthesis.* Journal of Materials Chemistry, 2008. **18**(48): p. 5900-5908.
72. Tamimi, F., et al., *Biocompatibility of magnesium phosphate minerals and their stability under physiological conditions.* Acta Biomaterialia, 2011. **7**(6): p. 2678-2685.
73. Qi, G.C., et al., *Osteoblastic cell response on magnesium-incorporated apatite coatings.* Applied Surface Science, 2008. **255**(2): p. 304-307.
74. Watts, S.J., et al., *Influence of magnesia on the structure and properties of bioactive glasses.* Journal of Non-Crystalline Solids, 2010. **356**(9-10): p. 517-524.
75. Gu, X.N., et al., *Microstructure, mechanical property, bio-corrosion and cytotoxicity evaluations of Mg/HA composites.* Materials Science & Engineering C-Materials for Biological Applications, 2010. **30**(6): p. 827-832.
76. Kartelia, E.M., *Thermal characterization of magnesium containing ionomer glasses*. 2010, Birmingham: University of Birmingham. 70 p., 3 p. of plates.
77. Kang, S.-J.L., *Sintering: densification, grain growth and microstructure*. 2004: Butterworth-Heinemann.
78. Committee, A.I.H., *Powder Metal Technologies and Applications*. 1998: ASM International.
79. Munir, Z.A., U. Anselmi-Tamburini, and M. Ohyanagi, *The effect of electric field and pressure on the synthesis and consolidation of materials: A review of the spark plasma sintering method.* Journal of Materials Science, 2006. **41**(3): p. 763-777.
80. Gorman, C.M. and R.G. Hill, *Heat-pressed ionomer glass-ceramics. Part I: an investigation of flow and microstructure.* Dent Mater, 2003. **19**(4): p. 320-6.
81. Donald, I.W. and E. Atomic Weapons Research, *Inorganic glasses and glass-ceramics : A review*. 1984, Aldermaston: Atomic Weapons Research Establishment.
82. Lewis, M.H., *Glasses and glass-ceramics*. 1989, London ; New York: Chapman and Hall. xii, 378 p.
83. McMillan, P.W., *Glass-ceramics*. 2d ed. Non-metallic solids. 1979, London ; New York: Academic Press. viii, 285 p.
84. O'Flynn, K.P. and K.T. Stanton, *Nucleation and Early Stage Crystallization of Fluorapatite in Apatite-Mullite Glass-Ceramics.* Crystal Growth & Design, 2010. **10**(3): p. 1111-1117.
85. Dhanaraj, G., et al., *Springer Handbook of Crystal Growth [electronic resource]*. 2010, Berlin, Heidelberg: Springer-Verlag Berlin Heidelberg. v.: digital.

86. Bach, H. and D. Krause, *Analysis of the composition and structure of glass and glass ceramics*. Schott series on glass and glass ceramics,. 1999, Berlin ; New York: Springer. xviii, 528 p.
87. Rudolph, P., G. M?ller, and J.-J. M?tois, *Crystal Growth - From Fundamentals to Technology [electronic resource]*. 2004, Burlington: Elsevier. 1 online resource (434 p.).
88. Shelby, J.E., *Introduction to glass science and technology*. 2005, Cambridge: Royal Society of Chemistry.
89. Shelby, J.E., *Introduction to Glass Science and Technology*. RSC paperbacks, The Royal Society of Chemistry 1997. 69-72.
90. Davis, M.J. and I. Mitra, *Crystallization measurements using DTA methods: Applications to Zerodur.* Journal Of The American Ceramic Society, 2003. **86**(9): p. 1540-1546.
91. Diouf, S. and A. Molinari, *Densification mechanisms in spark plasma sintering: Effect of particle size and pressure.* Powder Technology, 2012. **221**: p. 220-227.
92. Stanciu, L.A., V.Y. Kodash, and J.R. Groza, *Effects of heating rate on densification and grain growth during field-assisted sintering of alpha-Al2O3 and MoSi2 powders.* Metallurgical and Materials Transactions a-Physical Metallurgy and Materials Science, 2001. **32**(10): p. 2633-2638.
93. Zhou, Y., et al., *Effects of heating rate and particle size on pulse electric current sintering of alumina.* Scripta Materialia, 2003. **48**(12): p. 1631-1636.
94. Kim, B.N., et al., *Effects of heating rate on microstructure and transparency of spark-plasma-sintered alumina*. Journal of the European Ceramic Society, 2009. **29**(2): p. 323-327.
95. Shen, Z.J., et al., *Spark plasma sintering of alumina.* Journal of the American Ceramic Society, 2002. **85**(8): p. 1921-1927.
96. Chaim, R. and M. Margulis, *Densification maps for spark plasma sintering of nanocrystalline MgO ceramics.* Materials Science and Engineering a-Structural Materials Properties Microstructure and Processing, 2005. **407**(1-2): p. 180-187.
97. Anselmi-Tamburini, U., et al., *Spark plasma sintering and characterization of bulk nanostructured fully stabilized zirconia: Part I. Densification studies.* Journal of Materials Research, 2004. **19**(11): p. 3255-3262.
98. Orru, R., et al., *Consolidation/synthesis of materials by electric current activated/assisted sintering.* Materials Science & Engineering R-Reports, 2009. **63**(4-6): p. 127-287.
99. Quach, D.V., et al., *Pressure effects and grain growth kinetics in the consolidation of nanostructured fully stabilized zirconia by pulsed electric current sintering.* Acta Mater, 2010. **58**(15): p. 5022-5030.
100. Choi, K., et al., *Densification of nano-CeO2 ceramics as nuclear oxide surrogate by spark plasma sintering.* Journal of Nuclear Materials, 2010. **404**(3): p. 210-216.
101. Guo, W.M., et al., *Effect of pressure loading cycle on spark plasma sintered ZrB2-SiC-Yb2O3 ceramics.* Ceramics International, 2012. **38**(6): p. 5293-5297.
102. Carney, C.M. and T.I. Mah, *Current Isolation in Spark Plasma Sintering of Conductive and Nonconductive Ceramics.* Journal of the American Ceramic Society, 2008. **91**(10): p. 3448-3450.
103. Anselmi-Tamburini, U., et al., *Fundamental investigations on the spark plasma sintering/synthesis process - II. Modeling of current and temperature distributions.* Materials Science and Engineering a-Structural Materials Properties Microstructure and Processing, 2005. **394**(1-2): p. 139-148.

104. Wang, Y.C. and Z.Y. Fu, *Study of temperature field in spark plasma sintering.* Materials Science and Engineering B-Solid State Materials for Advanced Technology, 2002. **90**(1-2): p. 34-37.
105. Zavaliangos, A., et al., *Temperature evolution during field activated sintering.* Materials Science and Engineering a-Structural Materials Properties Microstructure and Processing, 2004. **379**(1-2): p. 218-228.
106. Vanmeensel, K., et al., *Field assisted sintering of electro-conductive ZrO2-based composites.* Journal of the European Ceramic Society, 2007. **27**(2-3): p. 979-985.
107. Vanmeensel, K., et al., *Modeling of Field Assisted Sintering Technology (Fast) and Its Application to Electro-Conductive Systems.* Advanced Processing and Manufacturing Technologies for Structural and Multifunctional Materials Ii, 2009. **29**(9): p. 109-122.
108. Tiwari, D., B. Basu, and K. Biswas, *Simulation of thermal and electric field evolution during spark plasma sintering.* Ceramics International, 2009. **35**(2): p. 699-708.
109. Bernard-Granger, G. and C. Guizard, *Densification mechanism involved during spark plasma sintering of a codoped alpha-alumina material: Part I. Formal sintering analysis.* Journal of Materials Research, 2009. **24**(1): p. 179-186.
110. Bernard-Granger, G., C. Guizard, and A. Addad, *Sintering of an ultra pure alpha-alumina powder: I. Densification, grain growth and sintering path.* Journal of Materials Science, 2007. **42**(15): p. 6316-6324.
111. Gu, Y.W., et al., *Spark plasma sintering of hydroxyapatite powders.* Biomaterials, 2002. **23**(1): p. 37-43.
112. Yu, L.G., et al., *Effect of spark plasma sintering on the microstructure and in vitro behavior of plasma sprayed HA coatings.* Biomaterials, 2003. **24**(16): p. 2695-2705.
113. Kawagoe, D., et al., *Transparent beta-tricalcium phosphate ceramics prepared by spark plasma sintering.* Journal of the Ceramic Society of Japan, 2004. **112**(1308): p. 462-463.
114. Zou, L.M., et al., *Fabrication of biomedical Ti-35Nb-7Zr-5Ta alloys by mechanical alloying and spark plasma sintering.* Powder Metallurgy, 2012. **55**(1): p. 65-70.
115. Shi, S.L., et al., *Reinforcement of hydroxyapatite bioceramic by addition of Ti3SiC2.* Journal of the American Ceramic Society, 2006. **89**(2): p. 743-745.
116. Lee, B.-T., et al., *Microstructures and fracture characteristics of spark plasma-sintered HAp–5vol.% Ag composites.* Materials Science and Engineering: A, 2006. **429**(1): p. 348-352.
117. Delaizir, G., et al., *Spark plasma sintering: an easy way to make infrared transparent glass–ceramics.* Journal of the American Ceramic Society, 2010. **93**(9): p. 2495-2498.
118. Riello, P., et al., *Erbium-doped LAS glass ceramics prepared by spark plasma sintering (SPS).* Journal of the European Ceramic Society, 2006. **26**(15): p. 3301-3306.
119. Tarafder, A., et al., *Structure, dielectric and optical properties of Nd< sup> 3+</sup>-doped LiTaO< sub> 3</sub> transparent ferroelectric glass–ceramic nanocomposites.* Journal of Alloys and Compounds, 2010. **489**(1): p. 281-288.
120. Alberti, C., *Tissue engineering: technological advances to improve its applications in reconstructive surgery.* G Chir, 2012. **33**(11-12): p. 435-43.
121. Mallick, K.K. and S.C. Cox, *Biomaterial scaffolds for tissue engineering.* Front Biosci (Elite Ed), 2013. **5**: p. 341-60.
122. Lee, K., D. Kaplan, and C. Chan, *Tissue engineering : scaffold systems for tissue engineering*. 2006, Berlin ; [Great Britain]: Springer.
123. Chu, P.K. and X. Liu, *Biomaterials fabrication and processing handbook*. 2008, Boca Raton, Fla.: CRC ; London : Taylor & Francis [distributor].
124. Sukmana, I., *Bioactive polymer scaffold for fabrication of vascularized engineering tissue.* Journal of Artificial Organs, 2012. **15**(3): p. 215-224.

125. Laurencin, C.T. and L.S. Nair, *Nanotechnology and tissue engineering : the scaffold*. 2008, Boca Raton, Fla. ; London: CRC Press.
126. Thibault, R.A., A.G. Mikos, and F.K. Kasper, *Scaffold/Extracellular Matrix Hybrid Constructs for Bone-Tissue Engineering.* Advanced Healthcare Materials, 2013. **2**(1): p. 13-24.
127. Gibson, L.J., M.F. Ashby, and B.A. Harley, *Cellular materials in nature and medicine*. 2010, Cambridge: Cambridge University Press.
128. Zhi, W., et al., *A novel porous bioceramics scaffold by accumulating hydroxyapatite spherulites for large bone tissue engineering in vivo. II: Construct Large volume of bone grafts.* J Biomed Mater Res A, 2013.
129. Mobini, S., et al., *Bioactivity and Biocompatibility Studies on Silk-Based Scaffold for Bone Tissue Engineering.* Journal of Medical and Biological Engineering, 2013. **33**(2): p. 207-213.
130. Qiao, X., *Scaffold fabrication for bone tissue engineering*. 2011: Leeds. xiv, 278 leaves.
131. Khang, G., M.S. Kim, and H.B. Lee, *A manual for biomaterials : scaffold fabrication technology*. Manuals in biomedical research. 2007, Singapore ; London: World Scientific. xxix, 258 p.
132. Yoon, D.H. and D.W. Shin, *Extrusion forming of cordierite honeycomb with hexagonal open cells.* High-Performance Ceramics IV, Pts 1-3, 2007. **336-338**: p. 1035-1037.
133. Das, R.N., C.D. Madhusoodana, and K. Okada, *Rheological studies on cordierite honeycomb extrusion.* Journal of the European Ceramic Society, 2002. **22**(16): p. 2893-2900.
134. *Extrusion : process and product development*. 1971, [S.l.]: American Association of Cereal Chemists Central States Section.
135. Rees, H., et al., *Influenza vaccination during cancer therapy.* Archives of Disease in Childhood, 2010. **95**(7).
136. Scheffler, M. and P. Colombo, *Cellular ceramics : structure, manufacturing, properties and applications*. 2005, Weinheim: Chichester : Wiley-VCH ; John Wiley [distributor]. xxv, 645 p.
137. Aranzabal, A., et al., *Optimization of process parameters on the extrusion of honeycomb shaped monolith of H-ZSM-5 zeolite.* Chemical Engineering Journal, 2010. **162**(1): p. 415-423.
138. Jazayeri, S.H., *The influence of the geometry on the extrusion and properties of ceramic pastes*. 1989, Birmingham: University of Birmingham.
139. Lord, W., *CATALYST SUPPORT*. 1974, Google Patents.
140. Blackburn, S. and D.I. Wilson, *Shaping ceramics by plastic processing.* Journal of the European Ceramic Society, 2008. **28**(7): p. 1341-1351.
141. Karhu, H. and y. Turun, *XPS studies of alumina and silica supported Pt, Pd and CuO catalysts with Ba, La and Ce modifiers*. Turun yliopiston julkaisuja. Sarja A1, Astronomica - Chemica - Physica - Mathematica. 2002, Turku: Turun yliopisto. 1 v. (various pagings).
142. Benbow, J. and J. Bridgwater, *Paste flow and extrusion*. Oxford series on advanced manufacturing. 1993, Oxford ; New York: Clarendon Press. xv, 153 p.
143. Marsh, S.P., *Multiparticle effects in the sintering of supported metal catalysts*. 1984, Troy, NY: Rensselaer Polytechnic Institute.
144. Hartmann, D., *Implementing Cisco Unified Communications Manager. : authorized self-study guide*. 2008, Indianapolis, Ind.: Cisco Press. 524 p.
145. Mark, H.F. and J.I. Kroschwitz, *Encyclopedia of polymer science and engineering*. 2nd / editorial board, Herman F. Mark ... et al. ; editor-in-chief, Jacqueline I. Kroschwitz. ed. 1985, New York ; Chichester: Wiley.

146. Althaus, T.O. and E.J. Windhab, *Extrusion of highly unsaturated wet powders: Stress fields in extruder barrels.* Powder Technology, 2011. **211**(1): p. 10-18.
147. Blackburn, S. and H. Bohm, *A method for calculating the pressure drop in honeycomb dies.* Journal of the European Ceramic Society, 1997. **17**(2-3): p. 183-189.
148. Clifford, A., et al., *The influence of calcium to phosphate ratio on the nucleation and crystallisation of apatite glass ceramics.* Journal of Materials Science: Materials in Medicine, 2001. **12**: p. 461-469.
149. Quinn, G.D. and R.C. Bradt, *On the Vickers indentation fracture toughness test.* Journal of the American Ceramic Society, 2007. **90**(3): p. 673-680.
150. Roy, S. and B. Basu, *Hardness properties and microscopic investigation of crack-crystal interaction in SiO2-MgO-Al2O3-K2O-B2O3-F glass ceramic system.* Journal of Materials Science-Materials in Medicine, 2010. **21**(1): p. 109-122.
151. Vullo, P. and M.J. Davis, *Comparative study of micro-indentation and Chevron notch fracture toughness measurements of silicate and phosphate glasses.* Journal of Non-Crystalline Solids, 2004. **349**: p. 180-184.
152. Hill, R., et al., *Real-time nucleation and crystallization studies of a fluorapatite glass-ceramics using small-angle neutron scattering and neutron diffraction.* Journal of the American Ceramic Society, 2007. **90**(3): p. 763-768.
153. Munir, Z., U. Anselmi-Tamburini, and M. Ohyanagi, *The effect of electric field and pressure on the synthesis and consolidation of materials: a review of the spark plasma sintering method.* Journal of Materials Science, 2006. **41**(3): p. 763-777.
154. Draper, O., et al., *A comparison of paste rheology and extrudate strength with respect to binder formulation and forming technique.* Journal of Materials Processing Technology, 1999. **93**: p. 141-146.
155. Martin, P.J., D.I. Wilson, and P.E. Bonnett, *Rheological study of a talc-based paste for extrusion-granulation.* Journal of the European Ceramic Society, 2004. **24**(10-11): p. 3155-3168.
156. Mooney, M. and S. Black, *A generalized fluidity power law and laws of extrusion.* Journal of colloid science, 1952. **7**(3): p. 204-217.